

Improvement of scanning ion-conductance microscopy for bio-analytical application

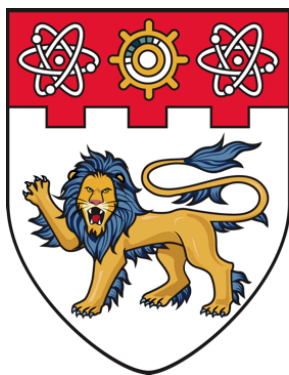
Kim, Joonhui

2018

Kim, J. (2018). Improvement of scanning ion-conductance microscopy for bio-analytical application. Doctoral thesis, Nanyang Technological University, Singapore.

<http://hdl.handle.net/10356/73734>

<https://doi.org/10.32657/10356/73734>



**NANYANG
TECHNOLOGICAL
UNIVERSITY**

SINGAPORE

**IMPROVEMENT OF
SCANNING ION-CONDUCTANCE MICROSCOPY
FOR BIO-ANALYTICAL APPLICATION**

JOONHUI KIM

SCHOOL OF MATERIALS SCIENCE AND ENGINEERING

2018

**IMPROVEMENT OF
SCANNING ION-CONDUCTANCE MICROSCOPY
FOR BIO-ANALYTICAL APPLICATION**

JOONHUI KIM

SCHOOL OF MATERIALS SCIENCE AND ENGINEERING

A thesis submitted to the Nanyang Technological University
in partial fulfilment of the requirement for the degree of
Doctor of Philosophy

2018

Statement of Originality

I hereby certify that the work embodied in this thesis is the result of original research and has not been submitted for a higher degree to any other University or Institution.

August 2, 2017

.....

Date

Joonhui Kim

.....

Joonhui Kim

Abstract

Scanning ion-conductance microscopy (SICM) is an emerging microscope technique among the family of scanning probe microscopy (SPM). Since the invention of scanning tunneling microscopy (STM) in 1981, SPM has widened their capabilities and opened the understanding of small things. The most promising one of SPM family is atomic force microscopy (AFM). AFM has the virtue of operating in any environment, vacuum, air and even in liquid. AFM can profile almost all physical and chemical properties in small scale by functionalization of its probes. By virtue of versatile utility, AFM has been stabilized for many years since its invention in 1986 and becomes a standard tool for nanoscale research. Increasing demands of biological studies in sub-micrometer level, AFM reaches its limitation because of employing forces to the target materials. Also, even though AFM can be utilized in a liquid environment, a serious interaction between the probe and the medium hinders to find the optimal operating condition. SICM natively loosens the problem, and provides the solution for bio-analytical studies, currently. However, the history of SICM is quite young; there are still many unrevealed principles waiting. Even if the measuring ion-conductance began from the Faraday's age, the ion-transport in a sub-micrometer channel has been actively studied by modern researchers. The pipette with an opening in sub-micrometer scale is a well-defined model system of the submicrometer channels. Hence, this dissertation explores the advantages of SPM techniques, and discusses the current limitations both of AFM and SICM, first. This thesis shows what aspect of AFM is superior to the high-resolution scanning electron microscope (SEM), then explains the needs of a special utility to study soft materials. Although this thesis mainly targets SICM, the most promising feature of AFM, i.e. gauging of mechanical properties is presented with the extended functionality of SICM. The second part dedicates to improving and understanding the microscopy. Assuming Nitz's model based on Ohm's law, the alternative circuit configuration is suggested to reduce the system impedance. Reduced impedance leads lower noise and increasing the response speed of the probe. Then, this dissertation is organized to provide a platform to analyze the ion-transport phenomena over the Ohm's law based model as a future perspective. The Poisson-Nernst-Planck model is an extended

model to elucidate the kinetics of charged particles in a continuous medium. The brief discussion of the Poisson-Nernst-Planck equation is included. The progress presented in this dissertation would contribute to unravel questions about small things.

Acknowledgments

At the moment of getting to understand the topic, I have to finish my Ph.D. course. There were many moments of regrets, joys, and gratitude. One day I became very ambitious, and the other day I was depressed. Whenever I was in wrong way, there have been so many persons to help me. It is unable to raise one Ph.D. without attentions and helps from the community.

I would like to thank Professor Nam-Joon Cho for giving me the opportunity to pursue my Ph.D. degree here in Nanyang Technological University. It cannot be imagined without him to continue my Ph.D. He has given me lots of inspiration for my topic and continued to help me in more ways than one. He selflessly takes the time out of his schedule to talk with me whenever I am in need. When discussing trivial ideas, he would never disregard them, and after our conversations, I felt the ideas become more solid and feasible. I feel that I have still lots of things to learn from him, but it may be the time to start being an independent researcher.

I want to thank Dr. Sang-il Park. I learned the way of thinking from him when I was young. I thank Dr. Sang-Joon Cho and Prof. Jungchul Lee. Dr. Park, Dr. Cho, and Prof. Lee were willing to give a chance of collaboration, and hospitable environment.

I want to thank Seong-Oh Kim, a good friend of mine who has contributed greatly to the main idea and efforts of my project. I have immensely enjoyed walking back to our dormitory together and discussing our experiments. I give thanks to Ahram Kim and Donghyuk Lee. We were not only discussing our projects but have shared much of time personally. I really thank our lab members, Dr. Josh Jackman, Dr. Ferhan Rahim, Dr. Jurriaan Gillissen, Dr. Jeung Eun Seo, Dr. Jae Ho Lee, Dr. Jae Hyeok Choi, Hitomi, Saziye, Minchul, Bo-Kyeong, Soohyun, Elba, Gaia, Jin, MikeC, MikeP, and all of them. I appreciate Weibeng, who is a very kind person and helped me to have a good life in Singapore. I thank Supriya and Marc, who are the best friends in Singapore, and good tennis partners. I especially thank Mr. Jooho Son and Ms. Yongjoo Han's family. Without

their warm care, I could not get used to living abroad. I very thank Myunghee, Kyunghee, and Jaehyun. When I was in a hard time, they stood by me.

I really appreciate my family for allowing me to continue my studies. To my brothers, Joongeol and Joonsoo, and their families, I give thank for supporting me always. Thank you, my father and mother. I am a very blessed man as your son. Even in my absence, my daughters, Jena and Yuna have been growing up well, and for that I am proud. If it were not for my wife's parents' help, I would have many worries, so I really thank my parents-in-law. I would like to give great thanks to my wife. I love you.

Table of Contents

Abstract.....	i
Acknowledgments	iii
Table of Contents	v
Table Captions.....	xi
Figure Captions.....	xiii
Abbreviations	xvii
Chapter 1 Introduction.....	1
1.1 Background and Significance	2
1.2 Hypothesis and Objective	8
1.3 Dissertation Overview	9
1.4 Findings and Outcomes	10
References.....	11
Chapter 2 Literature Review	13
2.1 Overview.....	14
2.2 Advances in SICM Instrumentation	15
2.2.1 AC mode: SICM with Vibrating Probes	15
2.2.2 AC-bias Mode	17
2.2.3 Mapping Surface Charges by SICM	18

2.2.4	Hopping (or ARS) Mode and its Variations.....	19
2.2.5	Works on Improving Approaching Speed.....	21
2.2.6	Works on Optimizing Retract Distance.....	21
2.2.7	Works on Minimizing Number of Pixels	22
2.2.8	Other Works	23
2.2.9	Summary	23
2.3	Properties of Nanopipettes.....	24
2.3.1	Ohmic Model: Analytical Solution.....	24
2.3.2	Ohmic Model: Numerical Solution	26
2.3.3	Estimating Tip Geometry	28
2.3.4	Electrical Properties	28
2.3.5	Ion Rectification and Poisson-Nernst-Planck Model.....	29
2.4	Ph.D. in Context of Literature	30
	References.....	31
Chapter 3	Methodology	39
3.1	Atomic Force Microscopy (AFM).....	40
3.1.1	Operating Principle of AFM	40
3.1.2	Force Spectroscopy	41
3.1.3	Modulation Technique	43
3.2	Scanning Ion-Conductance Microscopy (SICM)	46
3.2.1	Operational Principle of SICM	46
3.2.2	Vertical Resolution of SICM.....	48
3.2.3	Lock-in Amplifier and Note on AC-mode SICM	49
3.3	Finite Element Method (FEM)	52

3.3.1	Variational Form	52
3.3.2	Numerical Solution of FEM.....	53
3.3.3	Linearized Poisson-Boltzmann Equation.....	56
	References.....	57
Chapter 4	Structural Analysis by AFM and SEM.....	59
4.1	Introduction.....	60
4.2	Materials and Methods	61
4.2.1	Atomic Force Microscopy (AFM)	61
4.2.2	Scanning Electron Microscopy (SEM)	61
4.2.3	Preparation of Epididymis Spermatozoa.....	62
4.3	Results.....	62
4.4	Discussion.....	68
	References.....	70
Chapter 5	Dimensional Comparison between AFM and SICM.....	73
5.1	Introduction.....	74
5.2	Materials and Methods	74
5.2.1	Atomic Force Microscopy (AFM)	74
5.2.2	Scanning Ion-Conductance Microscopy (SICM).....	75
5.2.3	Edge-enhanced coloring.....	76
5.2.4	Buffer Solution.....	76
5.2.5	Collagen Fibrils.....	76
5.2.6	Fibroblast Cells	77
5.3	Results and Discussion	77
5.3.1	Imaging Collagen Fibrils	77

5.3.2 Imaging a Cell	80
5.4 Conclusions.....	80
References.....	83
Chapter 6 Mechanical Property Measurement by AFM and SICM.....	87
6.1 Introduction.....	88
6.2 Materials and Methods	89
6.2.1 L929 Cells and Viability Assay.....	89
6.2.2 SPM Apparatus	90
6.2.3 Cell Fluctuation Analysis by SICM	90
6.2.4 AFM Measurements of Young's Modulus of Cells	91
6.3 Results and Discussion	92
6.3.1 Topographic Images of Live and Fixed L929 Cell using SICM.....	92
6.3.2 Surface Fluctuations of Untreated and PFA-treated Cells	92
6.3.3 Young's Modulus of Untreated and PFA-treated Cells	93
6.3.4 Cell Changes in Various PFA Concentrations.....	95
6.4 Conclusions.....	98
References.....	98
Chapter 7 Improvement on SICM Instrumentation	103
7.1 Introduction.....	104
7.2 Theoretical Background.....	105
7.2.1 Limitation of Voltage Source Configuration.....	105
7.2.2 Current Source Configuration and its Characteristics.....	107
7.3 Materials and Methods	109
7.3.1 SICM and Nanopipettes	109

7.3.2	Measurement of Noise and Frequency Response	109
7.3.3	L929 Fibroblast Cell	109
7.3.4	Implementation of Current Source Configuration	110
7.4	Results and Discussion	111
7.4.1	Comparison of Bandwidth and Noise	111
7.4.2	Comparison of Image Quality	112
7.5	Conclusions.....	115
	References.....	116
Chapter 8	Conclusions and Future Outlook	119
8.1	Conclusions.....	120
8.2	Current-Distance Relation: Critical Review of Chapter 7.....	121
8.2.1	Source of Current-Distance Relation in SICM	121
8.2.2	Access Resistance as a Voltage Source	121
8.2.3	Discussion on Improving the Signal-to-Noise Ratio	124
8.3	Ultramicroelectrode	125
8.3.1	Electrolyte Filled Pipette.....	125
8.3.2	Ultramicroelectrode (UME).....	126
8.3.3	UME Fabrication by Electroplating	128
8.4	Beyond the Ohmic Model.....	132
8.5	Solving Poisson-Boltzmann Equation	133
8.5.1	Poisson-Nernst-Planck Equation.....	134
8.6	Future Work	136
	References.....	137
List of Publications	143

Table Captions

Table 2.1	Categorized summary of SICM imaging modes	24
Table 2.2	Summary of some representative works on PNP equation	30
Table 3.1	Hessian Matrixes	55
Table 6.1	Mean values and standard deviation (SD) of Young's modulus and fluctuation amplitude investigated at various PFA concentrations from live cell to 10 %	96

Figure Captions

Figure 1.1	Diagram of sensing mechanism of the scanning ion conductance microscope.....	3
Figure 1.2	Hopping Mode SICM.....	4
Figure 1.3	Typical configuration of SICM	6
Figure 1.4	Rectification effect of nanopipette	7
Figure 2.1	Scopus statistics from the query of <i>TITLE-ABS-KEY</i> ("scanning ion-conductance microscopy" OR "scanning ion-conductance microscope" OR <i>sicm</i>).....	14
Figure 2.2	Imaging modes in SICM	15
Figure 2.3	Current-distance curves with different DC bias voltages.....	17
Figure 2.4	Concept of simultaneous mapping of topography and surface charge distribution.....	19
Figure 2.5	Experimental approach curves depicting normalized DC ion current (a and b); and phase shift (c and d) behavior as a function of the probe-to-substrate distance, d	20
Figure 2.6	Schematic representation of the high-speed SICM algorithm.....	22
Figure 2.7	Approximate model of access resistance.....	25
Figure 2.8	Finite element method (EFM) simulated current-distance curves	26
Figure 2.9	FEM simulated images of two cylindrical particles.....	27
Figure 2.10	Nyquist plots of glass nanopipette.....	28
Figure 2.11	Impedance model of SICM	29
Figure 3.1	Schematics of AFM and force distance curve on a solid sample	40
Figure 3.2	Schematic of reconstruction of height of AFM.....	41

Figure 3.3	Indentation determination from AFM force curve data	42
Figure 3.4	The qualitative sketch of the force curve (a) and the resonance frequency shift (b) of the cantilever under force fields.....	44
Figure 3.5	Schematic of a basic SICM setup	46
Figure 3.6	Schematic of reconstruction of the height of SICM.....	47
Figure 3.7	Experimental data of the current distance curve and the noise spectrum of the SICM pipette	48
Figure 3.8	Mixing process and noise of the lock-in amplifier (LIA).....	50
Figure 3.9	Experimental current-distance results in AC-mode SICM with various lock-in amplifier (LIA) settings.....	51
Figure 4.1	Optical view and AFM images of a mouse spermatozoon.....	63
Figure 4.2	The stitched high-resolution AFM image in deflection mode of a mouse spermatozoon.....	64
Figure 4.3	The topographical image of AFM gives profiles of detailed sperm structures	66
Figure 4.4	Spermatozoa from caput and cauda were examined by AFM and SEM....	67
Figure 4.5	End knob structure statistics among 45 mouse spermatozoa	67
Figure 5.1	Comparison of AFM and SICM imaging capabilities of collagen fibrils ..	78
Figure 5.2	Line profile comparison of AFM and SICM imaging of the collagen intersection	79
Figure 5.3	AFM and SICM images of fixed fibroblast.....	81
Figure 6.1	Single L929 fibroblast cell surface image using SICM before and after 4 % PFA treatment	93
Figure 6.2	(a) Schematic view of the cell surface fluctuation setting by SICM, (b) Typical Ion current	94

Figure 6.3	Force spectroscopy	94
Figure 6.4	Surface fluctuation and Young's modulus.....	95
Figure 6.5	Evaluation of cytotoxicity property of PFA on the L929 cell	97
Figure 7.1	Principle of SICM signal amplification.....	106
Figure 7.2	Implementation of the current source circuit.....	110
Figure 7.3	Comparison of bandwidth and noise of voltage and current source configurations.....	111
Figure 7.4	Comparison of SICM imaging in voltage and current source configurations	113
Figure 7.5	Comparison of cell images for the conventional voltage source and the modified current source configurations.....	114
Figure 8.1	Circuit model of the pipette	122
Figure 8.2	Frequency response of modulating (a) the voltage bias and (b) the access resistance.....	122
Figure 8.3	Noise spectrums from PBS (blue) and 3M KCl (red) bath solutions	125
Figure 8.4	SEM images and schematics of SECM/SICM probes	126
Figure 8.5	Some represented modes in SECM	126
Figure 8.6	Current-distance curves for (a) negative feedback mode and (b) positive feedback mode in SECM.....	127
Figure 8.7	UME fabrication process by pulling the capillary and the electrode together	127
Figure 8.8	Electroplating of commercial silver-cyanide solution in a capillary.....	128
Figure 8.9	Reduction at the tip end with 10 mM AgNO ₃ solution	129
Figure 8.10	Dendritic growth of silver due to depletion of ions for DC plating in the pipette	130
Figure 8.11	Custom made plating station	130

Figure 8.12	Snapshots of electroplating of silver inside of the pipette.....	131
Figure 8.13	Numerical result of Gouy-Chapman model	133
Figure 8.14	Convergence of Poisson-Boltzmann equation.....	133
Figure 8.15	The pipette geometry and the mesh of PNP problem.....	134
Figure 8.16	FEM Simulation result of the pipette problem	135
Figure 8.17	Line profiles of the pipette simulation.....	136

Abbreviations

AAO	Anodic Aluminum Oxide
AC	Alternate Current
AFM	Atomic Force Microscope
AM-AFM	Amplitude Modulation Atomic Force Microscopy
APTES	3-aminopropyl triethoxysilane
ARS	Approach Retract Scanning
BM	Bias Modulation
BNC	Bayonet Neill–Concelman (connector)
DC	Direct Current
DIC	Differential Interference Contrast
DMEM	Dulbecco’s Modified Eagle Medium
DSP	Digital Signal Processor
EFM	Electrostatic Force Microscopy
EIS	Electro-Impedance Spectroscopy
FBS	Fetal Bovine Serum
FEM	Finite Element Method
FET	Field Effect Transistor
FM-AFM	Frequency Modulation Atomic Force Microscopy
GBP	Gain Bandwidth Product
HPICM	Hopping Probe Ion-Conductance Microscope
ICR	Institute of Cancer Research
IEEE	Institute of Electrical and Electronics Engineers
LIA	Lock-in Amplifier
MFM	Magnetic Force Microscopy
NCM	Non-Contact Mode (AFM)
NP	Nernst-Planck (equation)
opamp	Operational Amplifier
PB	Poisson-Boltzmann (equation)
PBS	Phosphate Buffered Saline

PCB	Printed Circuit Board
PDE	Partial Differential Equation
PDMS	polydimethylsiloxane
PFA	paraformaldehyde
PM	Phase Modulation
PNP	Poisson-Nernst-Planck (equation) and known as NPP
PSPD	Position Sensitive Photodiode
RC	Resistors and Capacitors
RMS	Root Mean Square
SCM	Scanning Capacitance Microscopy
SEM	Scanning Electron Microscope
SECM	Scanning Electrochemical Microscope
SICM	Scanning Ion-Conductance Microscope
SKPM	Scanning Kelvin Probe Microscopy
SMA	Subminiature version A (connector)
SNR	Signal-to-Noise Ratio
SNOM	Scanning Near-field Optical Microscopy and known as NSOM
SPICE	Simulation Program with Integrated Circuit Emphasis
SPM	Scanning Probe Microscope
SSE	Sum of Squared Residuals
STA	Standing Approach
TC	Time Constant
TSV	Through-Silicon Via
UME	Ultramicroelectrode
vSICM	vibrating SICM

Chapter 1

Introduction

Scanning ion-conductance microscopy (SICM) is a promising tool to investigate biological samples in aqueous solution. SICM reconstructs a morphological map from the distance-modulated ion-current signal. There have been many efforts on stabilizing the operation of SICM; especially adopting hopping mode, SICM became capable of taking a high-resolution image of whole cell morphologies. However, there is still an obstacle for SICM to be a daily practical microscope because of its low throughput. In this chapter, bottlenecks of SICM are profiled, and strategies to improve these bottlenecks are discussed. In addition, since the most important part is the probe or the nanopipette, this chapter also overviews the encountered problems for understanding the electrolyte system surrounding the nanopipette.

1.1 Background and Significance

Since the invention of scanning tunneling microscopy (STM) in 1981,¹ scanning probe microscopy (SPM) family has been utilized for revealing the nanoscale phenomena. The principle of SPM is quite different from that of optical microscopy and electron microscopy families. SPM uses a very sharp stylus, which scans over the target surface while maintaining a certain distance, with an analogy of a turntable where a stylus follows a long groove to make a sound. One interesting point is that SPM is called as a kind of microscopes, but it has extended their functionality from the nature of using a stylus. The inventors, Binnig and Rohrer also commented on the birth of the STM in their Nobel Lecture in 1986² as follows: “The original idea then was not to build a microscope but rather to perform spectroscopy locally on an area less than 100 Å in diameter.” It is not only advance in science to take surface images in 1000 times higher magnitude than the optical diffraction limit, but also SPM is capable of recording spectroscopy on a tiny area and to manipulate particles in atomic level.

Atomic force microscopy was introduced by Binnig, Quate, and Gerber in 1986 to overcome that STM could not operate well with non-conducting samples and in air.³ They introduced a new stylus probe (or so called a tip) attached to a cantilever, which can deflect with soft spring constant in the order of 1 N m^{-1} . By the capability of operating on various samples and in air, AFM became the most popular microscope in SPM family. Then AFM extended their applications by functionalized probes, e.g. scanning magnetic force microscopy (MFM),⁴ scanning electrostatic force microscopy (EFM),^{5,6} scanning Kelvin probe microscopy (SKPM),⁷ scanning capacitance microscopy (SCM),⁸ scanning near-field optical microscopy (SNOM)⁹ and so forth. The discussion on comparison between AFM and scanning electron microscopy (SEM) is presented in Chapter 4.

A specialized SPM technique was developed for operating in the electrolyte solution. It is named scanning ion-conductance microscopy (SICM) by Hansma et al. in 1989.¹¹ Almost ten years later, Korchev et al. demonstrated the capability of SICM for imaging living cells successfully in 1997,^{10,12} then SICM became the most promising tool for bio-analytical

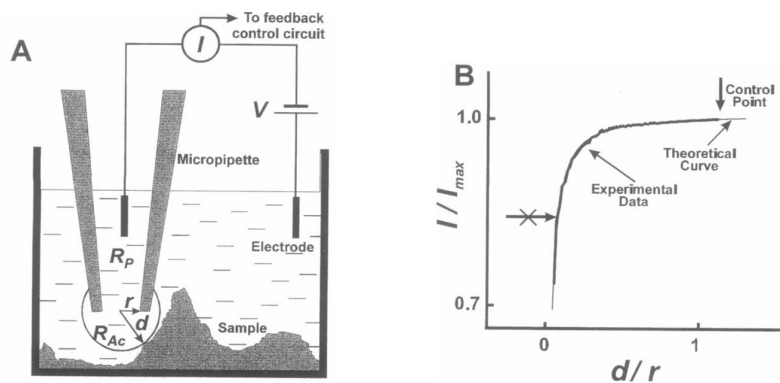


Figure 1.1 Diagram of sensing mechanism of the scanning ion conductance microscope. (a) Ion-current flows from a bath electrode to a pipette electrode and is impeded by the gap between the pipette and the sample. (b) Typical current-distance curve; as the pipette approaches the sample, the ion-current is reduced. Adapted from Korchev et al. 1997.¹⁰

application among SPM families. Chapter 5 discusses why SICM is more suitable than AFM for studying soft samples in the electrolyte solution. SICM uses a pulled pipette as a stylus to detect ion-current between two electrodes; the reference electrode is located in bulk solution, and the working electrode is inserted inside of the pipette. If the pipette is close to the sample surface, the cross-sectional area of current flow between the pipette apex and the surface decreases, so that the ion-current becomes impeded. Figure 1.1b shows the typical current-distance curve of SICM. When the pipette approaches the sample, the ion-current decreases.

Intrinsically the ion current flows just beneath of the pipette apex, so SICM has no any hints for encountering obstacles forgoing direction. Moreover, the dimension of a biological cell is in the order of $1\text{ }\mu\text{m}$ to $10\text{ }\mu\text{m}$, which is much greater than the sensing distance of SICM, approximately 100 nm . To avoid the collision in lateral motion between the pipette and the side of the large biological cell, the hopping mode is typically used for SICM measurement instead of the raster scanning (or the continuous mode in Figure 1.2), which is conventionally used in AFM.^{13,14} The pipette approaches the sample, then is retracted higher than the cell height for securing no collision occurred. This hopping mode provided a stable operation to SCIM and became a standard scanning method in SICM. Figure 1.2 illustrates the concept of the hopping mode and the results. A cleaner image can be found

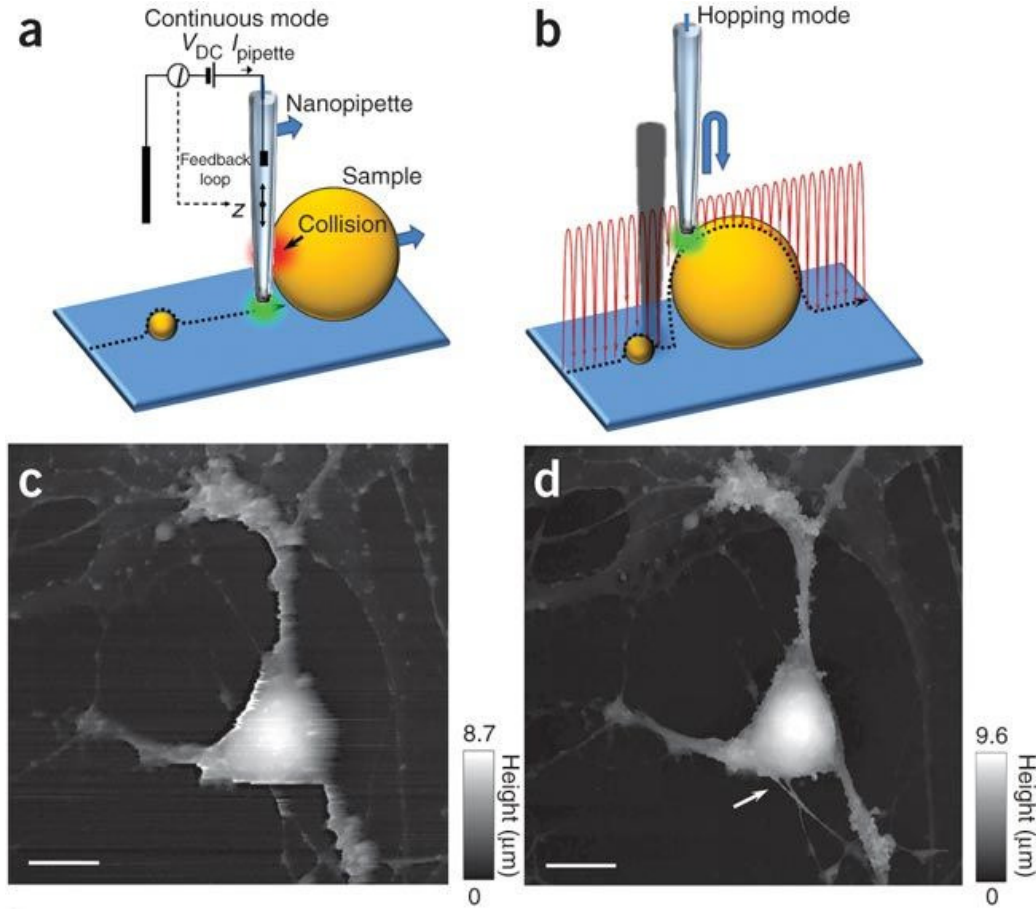


Figure 1.2 Hopping Mode SICM. (a) raster scanning is dragging a pipette just above the surface. (b) Hopping mode repeats approaching and retracting the pipette to prevent the collision. Adapted from Novak et al. 2009.¹³

without any strike lines in the hopping mode.

However, hopping mode has a disadvantage regarding the throughput, or the imaging time because the traveling distance of the pipette to acquire an image is dramatically increased. The imaging time, T is the sum of approaching, retracting and reposition time,

$$T = \sum_i^n \left(\frac{d_i}{v_a} + \frac{d_i}{v_r} + \tau_i \right) \quad (1.1)$$

where i is the pixel index, n is the total number of pixels, v_a is the approaching speed, v_r is the retracting speed, d_i is the approaching or retracting distance of i -th position and τ_i is the moving time to the next pixel. Because the approaching speed v_a is much slower than the

retracting speed v_r , and the reposition time τ_i is negligible, the imaging time with average approaching distance \bar{d} is simply

$$T \simeq n \cdot \frac{\bar{d}}{v_a}. \quad (1.2)$$

It takes 40 minutes to make one 128 by 128 pixels image with the approaching speed of $2 \mu\text{m s}^{-1}$ and the average distance of $0.3 \mu\text{m}$ for instance. This long imaging time seems to be impractical for biological research. It is not easy to say how fast scanning is enough for biological application because of various biological kinetics. But comparing with the raster scanning of AFM, which is expected to take 5 minutes for a 256 by 256 pixels moderate-resolution image and 10 minutes for a 512 by 512 pixels high-resolution image, 40 minutes does not seem to be realistic. From the equation (1.2), three strategies can be applied to improve the throughput of SICM:

1. Optimizing the retract distance, \bar{d} or d_i ,
2. Minimizing the number of pixels, n and
3. Improving approaching speed, v_a .

The various efforts on improving those parameters from SICM fields are discussed in Section 2.2. The first two strategies are algorithmic approaches to achieve performance with the questions; how to predict the height which is not measured yet, and how to decide the area where meaningful structure exists. The last strategy is a more straightforward approach to improve SICM. The overall works of this dissertation are focused to solve the problem related to the final strategy. At first, the bottleneck of speed should be identified.

A complete set of SICM consists of a nanopipette connected to a current-voltage converter as an ion-current sensor, a set of XY and Z scanner for nanopositioning, a data acquisition and feedback system for controlling the entire system as shown in Figure 1.3. The commercially available data acquisition system can do feedback faster than 50 kHz, so the feedback control bandwidth is more than 5 kHz. It is also easy to achieve a long-distance piezo-scanner with the resonance frequency of higher than 6 kHz. The electric current is

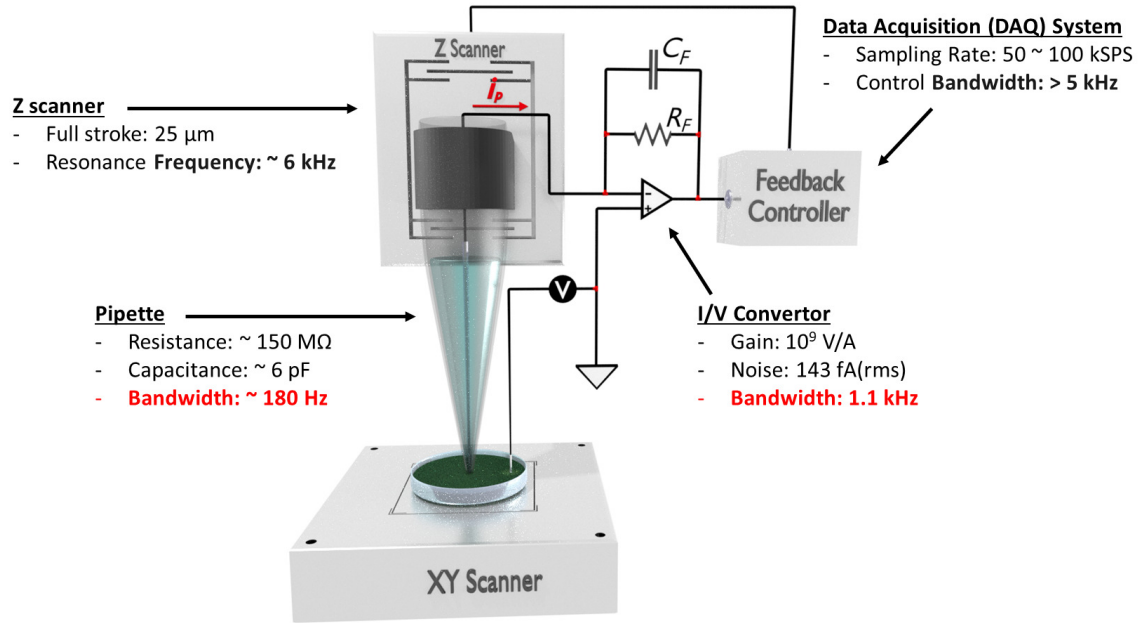


Figure 1.3 Typical configuration of SICM.

converted into a voltage signal for control with 10^9 transimpedance gain in the current-to-voltage converter with the reasonable noise level. Due to the physical dimension of a resistor, the capacitance of the transimpedance gain resistor is in the order of 0.1 pF, then the bandwidth of the current-to-voltage amplifier with the transimpedance gain of $1 \text{ G}\Omega$ could not be achieved greater than 1 kHz easily. Even though above values of bandwidth were chosen conservatively, the slowest part in SICM is the pipette whose bandwidth is expected as 180 Hz because of its resistance and capacitance in a general physiological condition, for example, phosphate buffered saline (PBS), are around $150 \text{ M}\Omega$ and 6 pF. Hence, it can be concluded that the performance of SICM is seized by the pipette firstly and the ion-current signal converter secondly.

It is natural to take ion-current flows in an electroneutral solution by migration, firstly. The model can be formulated by Laplace equation and Ohm's law,

$$\nabla^2 \phi = 0 \quad (1.3)$$

$$\mathbf{j} + \sigma \nabla \phi = 0 \quad (1.4)$$

where ϕ is electrostatic potential, \mathbf{j} is the current flux, and σ is the conductivity of the elec-

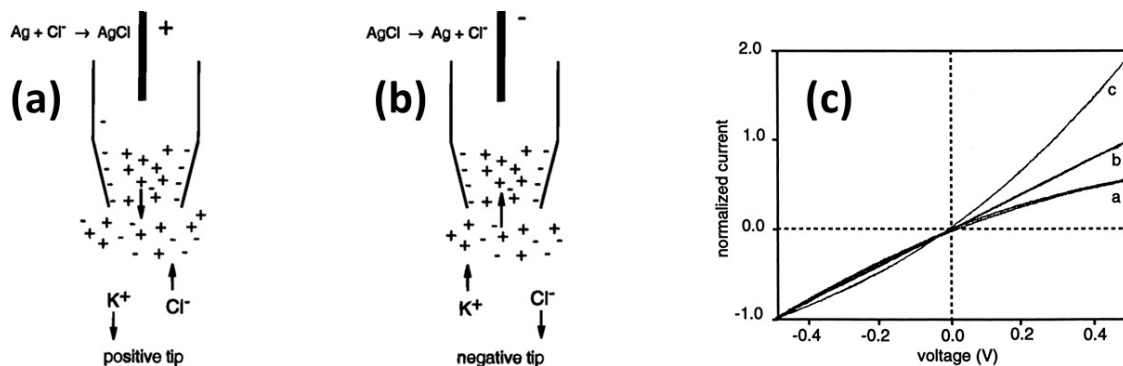


Figure 1.4 Rectification effect of nanopipette. (a) and (b) Schematic for an electrical double layer formed at the inner surface. (c) pH dependence of rectification effect: a-0.1 mM, b-0.4 mM and c-1 mM HCl added. Adapted from Wei and Bard 1997.¹⁵

trolyte. This point of view treats the electrolyte as a conductive matter with the property of resistivity. This model simplifies problems into the circuit theory, and it can be simulated by famous SPICE software. From this circuit model, the solution for improving the electrical properties of the pipette topic is discussed in Chapter 7.

Although the circuit model is simple, it is well known that ion-current in asymmetric geometry, like conically shaped pipette used in SICM, does not obey Ohm's law. Since older than 50 years ago, researchers have known a rectification effect occurred in the conically shaped pipette,¹⁶ and cell membranes.^{17,18} Wei and Bard suggested the first plausible explanation in 1997.¹⁵ They monitored current-voltage curves with various pH for changing the surface zeta potential of the glass, which is the material of the pipette. If the glass is negatively charged, for an anodic process, K^+ moves out of the tip and is constrained by the tip diameter (Figure 1.4a). For a cathodic process, K^+ moves in from the bulk solution, and K^+ is less hindered resulting in a larger current (Figure 1.4b). Figure 1.4c shows the trend in changes of the nonlinear current-voltage relationship by adding HCl. Solution pH alters the trend of ion-current rectification by changing the surface charge density of the pipette as shown in Figure 1.4c. When HCl is added to the solution, the glass surface becomes positively charged, then the rectification trend becomes reversed.

Cervera, Schiedt, and Ramírez reported the first numerical result with a sophisticated

model to describe a rectification effect of the pipette in 2005.^{19,20} They solved this rectification problem using 1D Poisson-Nernst-Planck (PNP) equation. The PNP equation with continuity equation is expressed by

$$\epsilon \nabla^2 \phi + F \sum_i z_i c_i = 0 \quad (1.5)$$

$$\mathbf{j}_i + D_i \left(\nabla c_i + \frac{F}{RT} z_i c_i \nabla \phi \right) = 0 \quad (1.6)$$

$$\frac{\partial c_i}{\partial t} + \nabla \cdot \mathbf{j}_i = 0 \quad (1.7)$$

where ϵ is the dielectric constant of the medium, t is time. And c_i is the concentration, z_i is the valency and \mathbf{j}_i is the flux density with the subscription i for each ion or particle.

At least from the 1960s, researchers in the semiconductor field have tried solving PNP equation because this model is the same for electrons and holes in semiconductor devices.^{21,22} Moreover, this model is also used in describing ion-selectivity of a cell membrane.²³ So, there are tons of papers from the semiconductor, physical chemistry, physiology and mathematical fields to solve this problem. Recently reported SICM papers include the numerical simulation results to correct the ion-current behavior over the Ohm's law by COMSOL multiphysics modeling software (COMSOL, US), which is commercial finite element method (FEM) solver. A brief feasibility of the PNP solver can be found in Section 3.3 and Section 8.4 with the FEniCS project,²⁴ which is a mature open source FEM solver.

1.2 Hypothesis and Objective

Many new findings and insights have been pulled from the introduction of new instrumentations. Since the invention of STM, the SPM family has been utilized to understand nanoscale phenomena. Because scientific instrumentation is attained by an interdisciplinary approach, instrumentation needs not only one discipline topic, but it is necessary to understand physical, chemical and engineering issues. The topics which should be proven are various, but this dissertation starts with a small step. The first thing to be clarified is what aspect of SICM is unique compared to other microscopes. Therefore, the first hypothesis is:

SICM would reconstruct the morphological variation of soft samples because of its contact-free scanning nature, whereas AFM would deform soft materials during mapping images because of its force-sensing nature.

However, there is still an obstacle to extend SICM as a daily use microscope. Current SICM is not practical to investigate the kinetics of biological phenomena because of its slow imaging time. In order to overcome this, the second hypothesis is:

If the total impedance of sensing circuitry is reduced, the overall throughput of SICM would be improved.

Because the environment in which SICM operates is electrolyte solution, and the main physics which SICM stems from is ion-migration, it is important to understand electro-chemical aspects. Taken together, specific objectives of this dissertation are:

1. to show the advantage of SPM by comparing SEM,
2. to find a suitable microscopy technique for the soft material research between AFM and SICM,
3. to demonstrate investigating mechanical properties of cells with AFM and SICM,
4. to suggest an alternative scheme for operating SICM to reduce the noise of the system.

1.3 Dissertation Overview

This dissertation starts with an outline of the background of the research fields and the significance of topics in Chapter 1. This chapter presents the objective and specific aims of this Ph.D. research. Chapter 2 provides the critical reviews on the recently developed methods in the SICM research field. Chapter 2 is organized into two sections: one section dedicates to the evolution of instrumentation, and another section is for models, which are physical basis of SICM. Then the theoretical foundations of techniques used in the

dissertation are presented in Chapter 3. The basic operating principles of AFM and SICM can be found in this chapter. The modern microscopes are compared in Chapter 4 and Chapter 5. First, the convenience and nondestructive feature of AFM compared with SEM is emphasized. Second, thanks to *contact-free* feature, it is demonstrated that SICM is more suitable to image soft biological samples than AFM. Chapter 6 shows an application of AFM and SICM. This chapter correlates the mechanical stiffness to the cell vitality. Alternative operating scheme to improve signal-to-noise is suggested from the assumption of Ohm's law in Chapter 7. Finally, Chapter 8 sketches the further consideration after Ph.D. work based on a critical review of the preceding contents.

1.4 Findings and Outcomes

This Ph.D. work is categorized into two parts. The one part is to emphasize the utility of SICM in biological or soft material research. The most prominent feature of SICM is its *contact-free* principle. Unlike AFM, which relies on the interaction between its probe and the surface, in case of the SICM probe, the nanopipette needs a gap from the target materials to let ions flow. Comparing to the other comprehensive studies of AFM and SICM, the work presented in Chapter 5 gives a fair competition to AFM because of employing all possible techniques to reduce mechanical forces come from AFM measurement itself. Despite those efforts, AFM still applies a mechanical stress onto the soft materials.

The other part is to understand and to improve the performance of SICM. The most focused performance is speed or throughput, which is related to the sensitivity of the SICM probe. The direction of improving the performance is also provided. For whatever reason, Chapter 7 yields an advance to increase the signal-to-noise ratio and the bandwidth from simply transposing two complementary concepts, voltage and current, or positions of the in-circuit resistor and the resistor of the sensory system. A correct logic is developed after getting the result of Chapter 7, and appears in Chapter 8.

References

- (1) Binnig, G.; Rohrer, H.; Gerber, C.; Weibel, E. Surface studies by scanning tunneling microscopy. *Phys. Rev. Lett.* **1982**, *49*, 57.
- (2) Binnig, G.; Rohrer, H. Scanning tunneling microscopy—from birth to adolescence. *Rev. Mod. Phys.* **1987**, *59*, 615.
- (3) Binnig, G.; Quate, C. F.; Gerber, C. Atomic force microscope. *Phys. Rev. Lett.* **1986**, *56*, 930–933.
- (4) Martin, Y.; Wickramasinghe, H. K. Magnetic imaging by “force microscopy” with 1000 Å resolution. *Appl. Phys. Lett.* **1987**, *50*, 1455–1457.
- (5) Terris, B.; Stern, J.; Rugar, D.; Mamin, H. Contact electrification using force microscopy. *Phys. Rev. Lett.* **1989**, *63*, 2669.
- (6) Khim, Z. G.; Hong, J. In *Nanoscale Phenomena in Ferroelectric Thin Films*; Springer: 2004, pp 157–182.
- (7) Henning, A. K.; Hochwitz, T.; Slinkman, J.; Never, J.; Hoffmann, S.; Kaszuba, P.; Daghlia, C. Two-dimensional surface dopant profiling in silicon using scanning Kelvin probe microscopy. *J. Appl. Phys.* **1995**, *77*, 1888–1896.
- (8) Williams, C.; Slinkman, J.; Hough, W.; Wickramasinghe, H. Lateral dopant profiling with 200 nm resolution by scanning capacitance microscopy. *Appl. Phys. Lett.* **1989**, *55*, 1662–1664.
- (9) Dürig, U.; Pohl, D. W.; Rohner, F. Near-field optical-scanning microscopy. *J. Appl. Phys.* **1986**, *59*, 3318–3327.
- (10) Korchev, Y. E.; Bashford, C. L.; Milovanovic, M.; Vodyanoy, I.; Lab, M. J. Scanning ion conductance microscopy of living cells. *Biophys. J.* **1997**, *73*, 653–658.
- (11) Hansma, P. K.; Drake, B.; Marti, O.; Gould, S. A.; Prater, C. B. The scanning ion-conductance microscope. *Science* **1989**, *243*, 641–3.
- (12) Korchev, Y. E.; Milovanovic, M.; Bashford, C. L.; Bennett, D. C.; Sviderskaya, E. V.; Vodyanoy, I.; Lab, M. J. Specialized scanning ion-conductance microscope for imaging of living cells. *J. Microsc.* **1997**, *188*, 17–23.
- (13) Novak, P.; Li, C.; Shevchuk, A. I.; Stepanyan, R.; Caldwell, M.; Hughes, S.; Smart, T. G.; Gorelik, J.; Ostanin, V. P.; Moss, G. W. J.; Frolenkov, G. I.; Klenerman, D.;

- Korchev, Y. E. Nanoscale live-cell imaging using hopping probe ion conductance microscopy. *Nat. Methods* **2009**, *6*, 279–282.
- (14) Mann, S.; Hoffmann, G.; Hengstenberg, A.; Schuhmann, W.; Dietzel, I. Pulse-mode scanning ion conductance microscopy – a method to investigate cultured hippocampal cells. *J. Neurosci. Methods* **2002**, *116*, 113–117.
- (15) Wei, C.; Bard, A. J.; Feldberg, S. W. Current rectification at quartz nanopipet electrodes. *Anal. Chem.* **1997**, *69*, 4627–4633.
- (16) Emck, J. Some Anomalous Electrical Effects in Microelectrodes. *Phys. Med. Biol.* **1959**, *3*, 339.
- (17) Teorell, T. Studies on the “diffusion effect” upon ionic distribution. some theoretical considerations. *Proc. Natl. Acad. Sci.* **1935**, *21*, 152–161.
- (18) Teorell, T. Transport phenomena in membranes eighth Spiers Memorial Lecture. *Discuss. Faraday Soc.* **1956**, *21*, 9–26.
- (19) Cervera, J.; Schiedt, B.; Ramírez, P. A Poisson/Nernst-Planck model for ionic transport through synthetic conical nanopores. *Europhys. Lett.* **2005**, *71*, 35.
- (20) Cervera, J.; Schiedt, B.; Neumann, R.; Mafé, S.; Ramírez, P. Ionic conduction, rectification, and selectivity in single conical nanopores. *J. Chem. Phys.* **2006**, *124*, 104706.
- (21) Gummel, H. K. A self-consistent iterative scheme for one-dimensional steady state transistor calculations. *IEEE Trans. Electron Devices* **1964**, *11*, 455–465.
- (22) Jerome, J. W., Analysis of charge transport: a mathematical study of semiconductor devices. Springer Science & Business Media: 2012.
- (23) MacGillivray, A. Nernst-Planck Equations and the Electroneutrality and Donnan Equilibrium Assumptions. *J. Chem. Phys.* **1968**, *48*, 2903–2907.
- (24) Logg, A.; Mardal, K.-A.; Wells, G., Automated solution of differential equations by the finite element method: The FEniCS book. Springer Science & Business Media: 2012; Vol. 84.

Chapter 2

Literature Review

Since the introduction of scanning ion-conductance microscopy (SICM) in 1989, there have been advances in instrumentation to stabilize the operation and to extend functionalities of SICM. The recent progress of SICM instrumentation is critically reviewed in this chapter. Adopted the idea from the modulation technique in atomic force microscopy (AFM), SICM developed AC mode to stabilize the ion-current signal. Although AC mode in SICM has no explicit relationship to distance sensitivity except low-pass filtering, this modulation technique may be used in detecting zeta potential of charged surfaces. To avoid the collision between the pipette and the sample, hopping mode or approach retract scanning (ARS) mode was introduced at the expense of throughput. Works on improving throughput are discussed. In addition, it is important to understand its model to improve a scientific device. The development of models for SICM is presented. The SICM model with the assumption of Ohm's law are discussed.

2.1 Overview

Just after the introduction of scanning ion-conductance microscopy (SICM), it had less attention from the research society till 1997. There were few papers for eight years. After successful demonstration of imaging living cells by Korchev in 1997,¹ SICM was beginning to gather wider interests from various groups. Two currently active groups, Prof. Patrick Unwin in the University of Warwick, UK, and Prof. Lane Baker in Indiana University, US have been researching SICM since around 2009. Figure 2.1 shows the time-frame plot of published documents with the query of *TITLE-ABS-KEY("scanning ion-conductance microscopy" OR "scanning ion-conductance microscope" OR sicm)* from Scopus database. Even though the query was not elaborated, the trend of research activities on SICM can be estimated roughly.

In this chapter, the recent progress of SICM instrumentation is critically reviewed. Most of researchers have adopted the modulation technique to SICM. Herein, pros and cons of the modulation technique are discussed. Then efforts on improving throughput are summarized. For the fundamental study, various models of SICM are also discussed. The model based on Ohm's law is not suitable to elucidate nanofluidic behavior so that the extended model is presented at the last of this chapter.

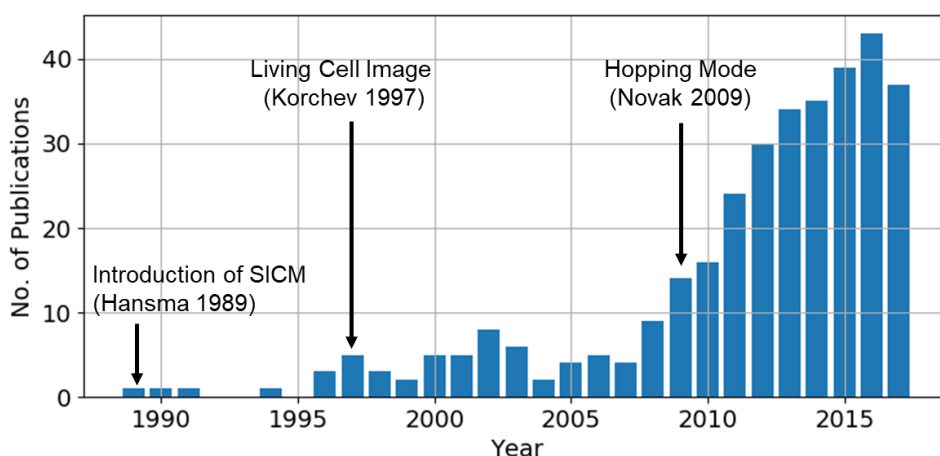


Figure 2.1 Scopus statistics from the query of *TITLE-ABS-KEY("scanning ion-conductance microscopy" OR "scanning ion-conductance microscope" OR sicm)*.

2.2 Advances in SICM Instrumentation

Since the invention of SICM, various imaging modes have been developed. Figure 2.2 shows most mentioned imaging modes. Figure 2.2a shows constant height mode, which is rarely used. However, recently Zhukov et al.³ adapted this concept to develop a high-speed SICM (described in Subsection 2.2.8). Figure 2.2b shows DC mode operation, which maintains the ion-current constant while adjusting the pipette position with feedback. DC mode is the natural scanning method in the AFM community, so it was first applied to SICM.⁴ In 2001, two research groups from the United Kingdom and the United States independently reported studies using AC mode SICM (Figure 2.2c): the nanopipette oscillates along the Z axis, and the modulated ion-current is monitored using the lock-in amplifier to increase sensitivity and stability of DC mode.^{5,6} Hopping mode (Figure 2.2d) was firstly introduced by Mann et al. in Ruhr-University Bochum, German and termed as a backstep mode to improve DC stability and to circumvent the situation where the nanopipette crashes overhanging cell structures.^{7,8} The hopping mode has become a popular scanning method in SICM after the successful demonstration of live cell imaging by Novak et al.⁹ This section discusses advances in instrumentation specifically.

2.2.1 AC mode: SICM with Vibrating Probes

The concept of modulated probes is trendy in AFM and is subcategorized into tapping mode,¹⁰ non-contact mode¹¹ and in a stricter term, dynamic force mode.¹² A cantilever, as a force sensing probe in AFM, oscillates near the resonance frequency of the cantilever, because the highest sensitivity of force is at this resonance. Proksch et al. introduced tapping

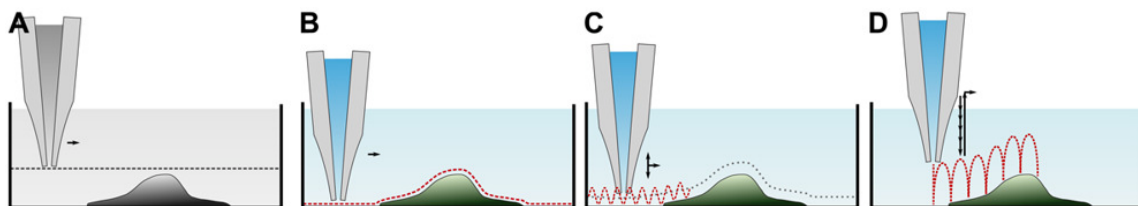


Figure 2.2 Imaging modes in SICM. The dotted line represents the trajectory of the tip apex. (A) Constant height mode, (B) DC mode, (C) AC mode, and (D) hopping mode. Adapted from Happel et al. 2012.²

mode SICM in 1996, which comprised of a bent nanopipette for sensing forces.¹³ The bent pipette oscillated at a resonance frequency between 50 kHz to 100 kHz to detect the force between the pipette and the sample, and the DC component of ion-current was monitored.

Five years after the introduction of tapping mode SICM, AC mode SICM or SICM with vibrating probes (vSICM), which did not vibrate the nanopipette near the resonance frequency, was introduced.⁵ Pastré et al. emphasized that this modulation technique would improve the sensitivity of the ion-current signal,⁵ and Shevchuk et al. mentioned: “it makes the measurement insensitive to changes in ion strength or DC drift.”⁶ So far, these statements have been considered as advantages of the AC mode. Moreover, the result of the simulation using finite element method (FEM) also argued that “AC feedback control yields a better tip response to surface features.”¹⁴ However, these advantages should be verified properly, because:

1. AFM vibrates the probe at the resonance with high Q -value that allows the highest sensitivity of force changes. But AC mode SICM does not vibrate the probe at its resonance in contrast to AFM. Subsection 3.1.3 describes the relationship between the resonance frequency and the force in AFM. AC mode SICM does not have a relationship between the oscillation frequency and the ion-current.
2. The lock-in amplifier (LIA) can amplify the signal with arbitrary gain. Thus, the slope of an ion-current to distance curve, which is related to sensitivity, can be adjusted arbitrarily. Also, the lock-in amplifier itself is not a noiseless source, and is just a good *bandpass filter*. Hence, the lock-in amplifier also amplifies noise. Even the manual of a commercial lock-in amplifier (SR830, Stanford Research System, CA) also says that “In fact, when there is noise at the input, there is noise on the output.” Subsection 3.2.3 discusses the lock-in detection technique in detail.
3. If the ion strength changes, the overall conductance is changed, and the amplitude of ion-conductance is also changed. Therefore, there is no strong reason explaining no correlations exist between the ion strength and AC mode amplitude.

2.2.2 AC-bias Mode

Voltage bias can be modulated instead of vibrating probes. One expected advantage is that AC-bias can minimize polarization of electrodes. Bias modulated (BM) SICM uses the amplitude signal for topography feedback,¹⁶ and phase modulation (PM) mode uses the in-phase signal for topography feedback because the quadrature signal of AC modulation is insensitive to distance changes between the pipette and the sample.¹⁵ Li et al. commented “the PM mode is immune to DC drift,”¹⁵ and displayed current-distance curves shown in Figure 2.3 as the evidence: the in-phase current signal in PM mode does not have a dependency on DC offset voltage (Figure 2.3b) whereas the current-distance curve of DC mode has a dependency on DC bias voltage (Figure 2.3a).

However, the first impression from studying Figure 2.3 is that the noise of in-phase current is much greater than DC even though the slope in the range of less than $0.1\ \mu\text{m}$ seems almost similar. So, the signal-to-noise ratio for in-phase current seems like to be worse than that of DC current. Second, the cause of DC drift was ambiguous. Li et al. imitated DC drift to change the bias voltage, but the modern electronics provides highly stable DC voltage drift in long-term. It is easy to find that a voltage reference integrated circuit has a stability of less than 0.01% (100 ppm) for over 1000 h. Moreover, there are many source meters which have a specification of less than 0.1% stability (typically 0.02%).

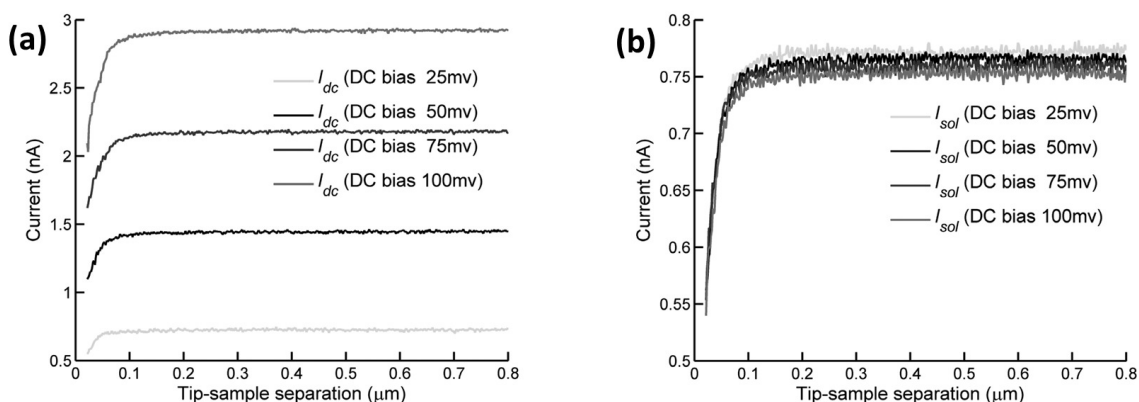


Figure 2.3 Current-distance curves with different DC bias voltages. (a) Current-distance curves in DC mode with various DC bias voltages, (b) In-phase current-distance curves in PM mode with different DC offset voltages. Adapted from Li et al. 2014.¹⁵

The most uncontrollable DC drift in SICM stems from ionic strength changes, but there is no correlation between ion strength changes and DC voltage changes.

Considering the measured current i has some relation f with applied voltage v , and this relation is given by

$$i = f(v) \quad (2.1)$$

while voltage consists of DC and AC terms, $v = v_{DC} + v_{AC}$, the measured current is approximated by

$$i \simeq f(v_{DC}) + v_{AC} \cdot \left. \frac{\partial f}{\partial v} \right|_{v_{DC}}. \quad (2.2)$$

The first term of the right-hand side is DC current, and the second term is AC current. If the current response function f is typically almost linear to the variable of v_{DC} , then $\partial f / \partial v$ is almost constant over various v_{DC} value. Therefore, AC current is independent from DC offset voltage. Hence, the result of Figure 2.3 could not be the evidence of stabilizing ion current from ion-strength drift.

The modulation technique limits the bandwidth of the measured current signal. The superficial result, which shows a less noisy signal than non-modulated DC signal, stems from the cost of the signal speed. Additionally, the pipette modulation can cause convection of the solution and might disturb ion-current measurement.¹⁷ Even though the current modulation technique seems to have drawbacks, one important application of the modulation technique remains; it is the capability of mapping surface charges.

2.2.3 Mapping Surface Charges by SICM

After introducing bias modulated (BM) SICM in 2014,¹⁶ Unwin's group in the University of Warwick, UK reported of mapping surface charges sequentially. They paid attention to the surface-induced rectification.¹⁹ McKelvey et al. demonstrated the capability of mapping surface charge using distance-modulated SCIM in 2014.²⁰ Perry et al. studied BM SICM for various charged surfaces in 2015,¹⁸ then Perry et al. successively visualized surface charges of living cells in 2016.²¹ Figure 2.4 shows the concept of simultaneous mapping of topography and surface charge distribution. For getting topographical images,

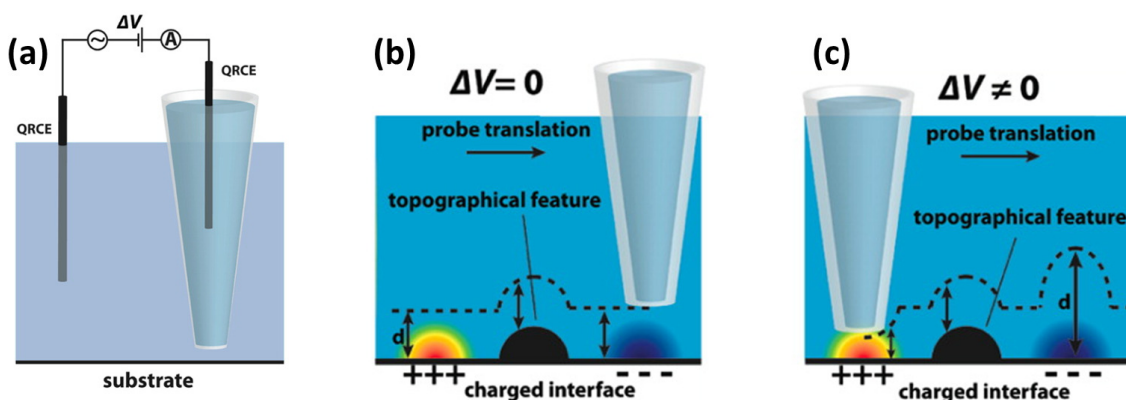


Figure 2.4 Concept of simultaneous mapping of topography and surface charge distribution. Adapted from Perry et al. 2015.¹⁸

BM mode is used while $v_{DC} = 0$. For mapping charge distribution, DC offset is applied, $v_{DC} \neq 0$, because the charged channel rectifies ion currents.

Figure 2.5 shows experimental approach curves on the negatively charged surface (glass, left column), and the positively charged surface (3-aminopropyl triethoxysilane or APTES, right column). DC current responses and AC phase responses are opposite to each surface with the same DC bias voltage.

2.2.4 Hopping (or ARS) Mode and its Variations

The morphological variation of the cell membrane is considered smooth, so it can be assumed that it is easier to scan over the cell surface in comparison to semiconductors. However, to get whole cell images, it is necessary to image the substrate in addition to the cell surface. Unfortunately, in that case, the pipette will meet a very steep and tall wall, and often result in colliding to the side of a cell and dragging the cell instead of not-touching the cell. In order to overcome this problem, backstep mode,⁷ hopping probe ion conductance microscope (HPICM),⁹ standing approach (STA) mode²² and approach retract scanning (ARS) mode^{23,24} were introduced (henceforth referred to as hopping mode or ARS mode in this dissertation). Like force-distance mapping²⁵ and step-in mode²⁶ in AFM, the pipette tries approaching the surface at every single pixel. The force-distance mapping also has many synonyms; the first appeared name was hopping mode in Japanese

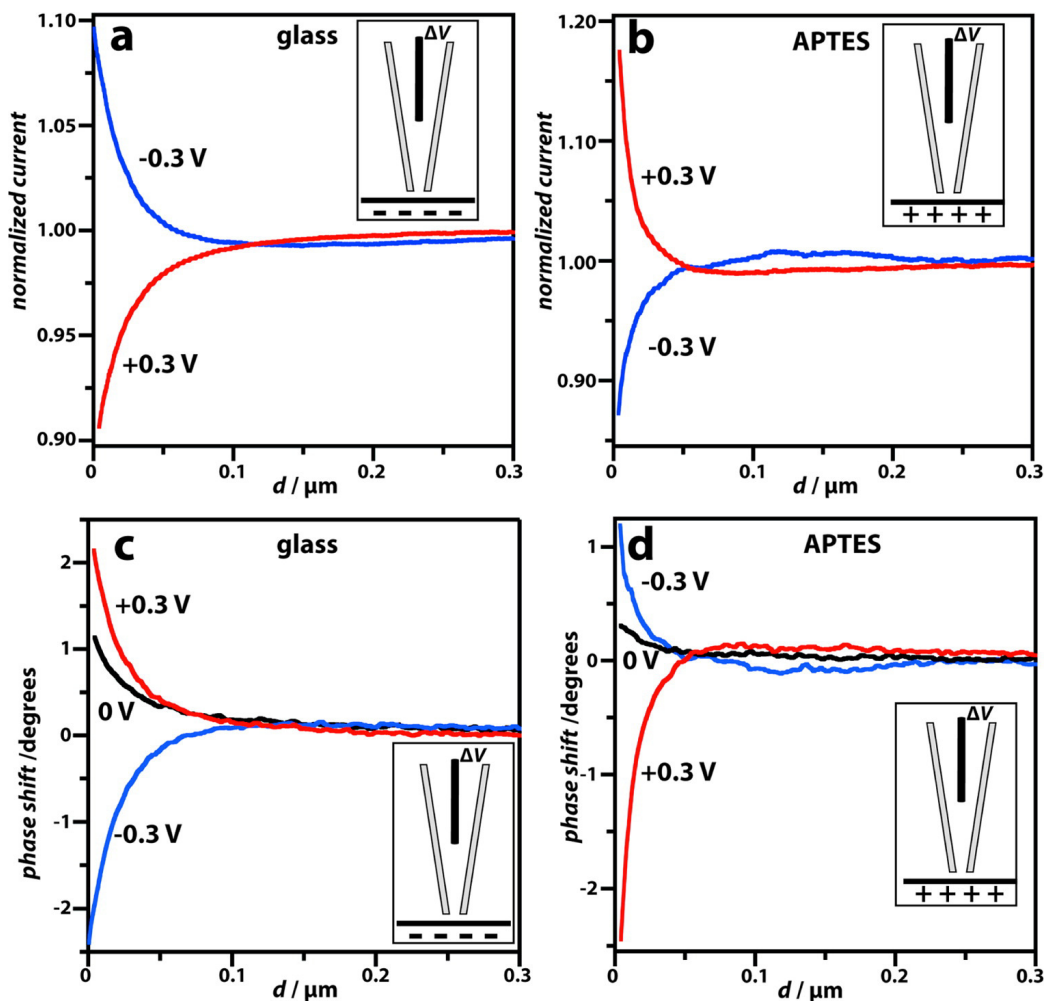


Figure 2.5 Experimental approach curves depicting normalized DC ion current (a and b); and phase shift (c and d) behavior as a function of the probe-to-substrate distance, d . Adapted from Perry et al. 2014.¹⁸

patent in 1988²⁷ and a journal paper in 1993,²⁸ then adhesive force mode (1994),²⁹ pulsed force mode (1997),³⁰ step-in scan (early of 2000), recently peak-force and pin-point mode were developed. Hopping mode also has the capability to stabilize slowly varying DC drift from concentration changes because the setpoint can be readjusted just before the approach. This stable operation is obtained at the expense of imaging time. Comparing with traditional raster scanning, which drags the pipette along the surface, hopping mode increases the travel distance of the pipette. That means it takes a significantly longer time to make an image than raster scanning.

As discussed in Chapter 1, the parameters which affect the imaging time are 1) the speed of approach, 2) the distance of approaching or retracting for moving to the next pixel, and 3) the number of pixels. The works on those topics are described in the following subsections.

2.2.5 Works on Improving Approaching Speed

There are two types of works to improve the approaching speed; one is to speed up the physical movement of the pipette, and the other is improving the sensor response. When the pipette approaches the surface quickly, an overshoot of the pipette motion occurs. Novak et al. attached an additional fast actuator to act as a brake booster and to stop the pipette motion faster.³¹ Closed loop ARS uses a closed-loop approaching algorithm instead of a discrete step movement of the pipette to increase approaching speed and to prevent negative overshooting.³²

After studying the phase modulation SICM, Li et al. introduced a capacitive compensation method to enhance the signal-to-noise ratio.³³ Zhuang et al. used two pipettes to eliminate the unnecessary pipette resistance R_P . One pipette is used for the scanning similar to regular SICM, and the other is used for the reference pipette resistance.³⁴ Using the bridge configuration, one can cancel out the intrinsic pipette resistance.

As one of this Ph.D. works, the improving approaching speed by enhancing the signal-to-noise ratio is suggested in Chapter 7.

2.2.6 Works on Optimizing Retract Distance

Floating backstep mode pre-scans the cell surface with low resolution first, determines the edges of the cell, then uses different retract distances in the second high-resolution image.⁸ Takahashi et al. introduced an algorithm to decide how far is good to move, known as standing approach (STA) mode; after approaching on the sample, STA mode retracts the pipette a certain distance (e.g. 2 μm), then if the ion current is not large enough, then STA mode tries to retract the pipette again until the ion-current is high enough.²²

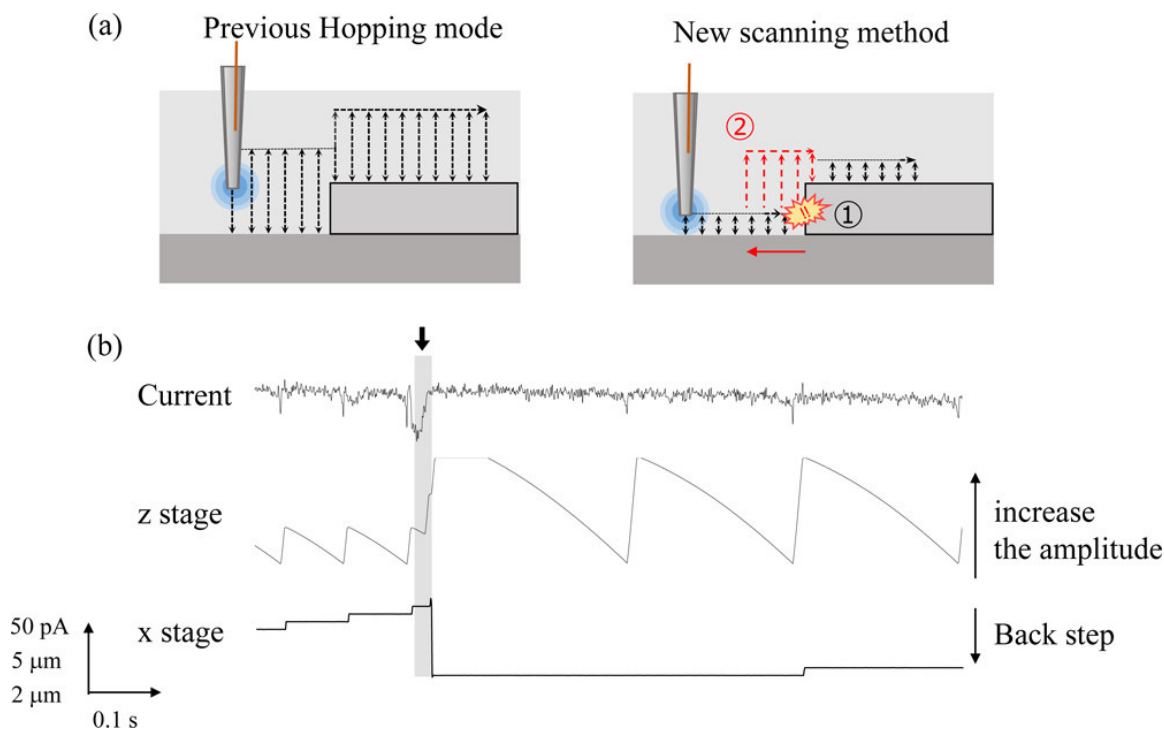


Figure 2.6 Schematic representation of the high-speed SICM algorithm. Adapted from Ida et al. 2017.³⁵

Ida et al. found one interesting behavior of ion current.³⁵ When the pipette contacts to the side of samples, the ion current abnormally decreases. So, the pipette can be hopping on the sample with small retract height in most of all areas. If there is abnormally low ion-current, the scanning method will go some distance back from the abnormal point, then do forward again by hopping mode with higher and safe retract distance (Figure 2.6.)

2.2.7 Works on Minimizing Number of Pixels

HPICM also uses an adaptive method, which scans the sample more than two times. HPICM pre-scans the sample in low-resolution, evaluates the roughness of each area, and then scans the sample again in high roughness regions.⁹ Floating backstep mode, which uses an adaptive method as well, tries to optimize the retract distance whereas HPICM attempts to minimize the number of pixels in the image. Another prior knowledge based method, which decides the region of interest by using edge detection instead of roughness, was reported.³⁶

Interestingly, Andersson et al. made an interesting observation: “non-raster scan measurements were quite common in a variety of fields,” but there was only raster scanning in AFM.³⁷ Then, they developed compressed sensing algorithm as a non-adaptive method, which samples less number of height data in random position than the original resolution, and reconstructs the original resolution image.³⁸ Li et al. adapted this method to SICM and demonstrated around 50 % improvement in imaging time.³⁹

2.2.8 Other Works

Hybrid scanning mode was also reported for improving the speed of SICM.³ As mentioned earlier, the hybrid scanning mode drags the pipette at almost constant height in order to save the feedback time. The pipette roughly follows the sample surface fast and records ion-current values simultaneously for post reconstruction of real topography. This hybrid scanning mode predicts next line features from previous line topography adaptively.

If the Z movement of the pipette is fast enough, the line-by-line scanning method could limit the performance. After getting one line, the sample should turn back, but the acceleration of the sample motion is discontinuous, so impulse applies on the sample and the XY scanner. This impulse appears as ringing marks on the border of images. Therefore, the spiral movement can be used for eliminating discontinuous acceleration. Kang et al. used this spiral scanning movement for fast electrochemical reaction mapping with SICM.⁴⁰

2.2.9 Summary

Table 2.1 categorized the SICM imaging modes. The two electrodes in SICM are excited from biasing sources, voltage or current. Moreover, the response of two electrodes can be detected by DC or modulation/demodulation technique (Measurement Technique). The pipette is dragged (Raster scan) or approached and repeatedly retracted (Hopping mode). The region of interest (ROI) can be decided adaptively or non-adaptively. In general, ‘DC mode’ refers to the composition of voltage bias with DC measurement during raster scanning, ‘AC mode’ implies the composition of voltage bias with Z modulation and raster scanning, and ‘hopping mode’ involves voltage bias with DC measurement in roughness

Table 2.1 Categorized summary of SICM imaging modes

Category	Method	First reported in SICM
Biasing	Voltage	Hansma 1989 ⁴
	Current Pulse	Mann 2002 ⁷
	Current	Kim 2015 ⁴¹
Measurement Technique	DC	Hansma 1989 ⁴
	Z modulation	Pastré 2001, ⁵ Shevchuk 2001 ⁶
	Bias modulation	McKelvey 2014, ¹⁶ Li 2014 ¹⁵
Scanning method	Raster scan	Hansma 1989 ⁴
	Hopping mode	Mann 2002 ⁷
	Spiral scanning	Kang 2016 ⁴⁰
Region of Interest	Adaptive (roughness)	Novak 2009 ⁹
	Adaptive (edge detection)	Li 2013 ³⁶
	Compressed sensing	Li 2014 ³⁹

based adaptive hopping scanning.

Even though there have been many efforts to improve imaging time especially algorithmic approach (i.e. scanning method and deciding the region of interest), it is needed to study the fundamental behavior of nanopipette dynamics to push the imaging time to the limit in which nature allows.

2.3 Properties of Nanopipettes

An electrolyte-filled nanopipette, which is pulled from a glass capillary, is used as the probe.⁴ This nanopipette is the fundamental component which is utilized to investigate nanoscale phenomena in a physiological environment. So, there have been many efforts to understand the phenomena occurring in the gap between the nanopipette apex and the surface. This section discusses models of nanopipettes and reviews the electrical characteristics of the nanopipette.

2.3.1 Ohmic Model: Analytical Solution

Nitz et al. firstly introduced the Ohmic model of the pipette in 1998.⁴² The access resistance R_{AC} was derived analytically in this paper, and given by

$$R_{AC} = \frac{3}{2\pi\kappa} \cdot \frac{\ln(r_o/r_i)}{z} \quad (2.3)$$

where κ is the conductance of the electrolyte, r_o and r_i are the outer and inner radii of the pipette tip end, respectively, and z is the distance from the pipette end to the sample surface. This equation can be induced by assuming a disk-shaped conductance channel. Assuming the ion-current is impeded under the end area of pipette glass (Figure 2.7), the access resistance can be calculated by

$$R_{AC} = \frac{1}{\kappa} \int_{r_i}^{r_o} \frac{dr}{2\pi r z} = \frac{1}{2\pi\kappa} \cdot \frac{\ln(r_o/r_i)}{z}. \quad (2.4)$$

The equation 2.3 and equation 2.4 have an only difference of the factor 3. Similarly, the pipette resistance R_P can be integrated to

$$R_P = \frac{1}{\pi\kappa} \cdot \frac{L}{r_b r_i} \simeq \frac{1}{\pi\kappa} \cdot \frac{1}{\tan(\theta/2)} \quad (2.5)$$

where r_b is the base radius, and L and θ are stem length and cone angle, respectively.^{14,42} Assuming the conductivity of electrolyte solution is $500 \text{ M}\Omega \mu\text{m}$ (the conductance of phosphate buffered saline (PBS) 1X solution is $14 \text{ M}\Omega^{-1} \text{ cm}$ to $17.8 \text{ M}\Omega^{-1} \text{ cm}$), and r_t is 50 nm , θ is 3° , then R_P is $122 \text{ M}\Omega$. This value well agrees with experimental resistance, around $150 \text{ M}\Omega$ with PBS 1X solution. Then, Nitz equation is obtained by

$$I(z) = I_0 \left(1 + \frac{z_0}{z}\right)^{-1} \quad (2.6)$$

$$z_0 = \frac{3r_b r_i}{2L} \ln\left(\frac{r_o}{r_i}\right) \quad (2.7)$$

where I_0 is the current when the pipette is far from the sample, or $I_0 = V/R_P$ with the applied voltage V .

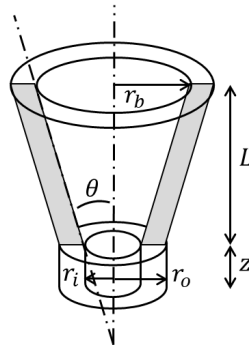


Figure 2.7 Approximate model of access resistance. The ion-current is impeded under the glass area approximately. The cross section of pipette is displayed in gray.

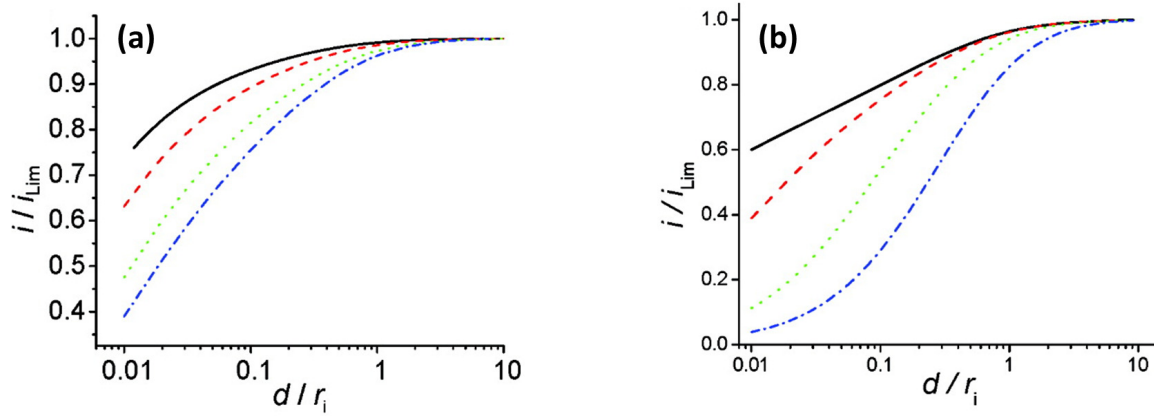


Figure 2.8 Finite element method (EFM) simulated current-distance curves. (a) various cone angles θ , solid black θ is 3° , dashed red 5° , dotted green 10° , dash-dotted 15° (b) various $RG = r_o/r_i$, solid black $RG = 1.1$, dashed red 1.1 , dotted green 2 , dash-dotted 10 . Adapted from Edwards et al. 2009.¹⁴

The pipette capacitance can be calculated by assuming that the electrolyte is highly conductive material and the capacitance stems from the glass capillary. The capacitance can be expressed by

$$C_P = C_{P0} + \frac{2\pi\epsilon L}{\ln(r_o/r_i)}. \quad (2.8)$$

The first term of the right-hand side C_{P0} denotes the contribution of tapered tip portion, and the second term is for submerged coaxial capillary portion. L is the immersed length of coaxial portion, ϵ is dielectric constant and r_o , r_i are the outer and inner radii of the coaxial capillary. Using the dielectric constant of glass as 4.6, the capacitance per length of the coaxial capillary is 0.47 pF/mm. If the pipette is submerged 5 mm in the solution, the capacitance of the coaxial capillary portion is 2.3 pF. The order of this approximation value seems to agree with experimental value, around 6 pF.¹⁶ The through-silicon via (TSV) has similar tapered geometry of the pipette tip end, which contributes C_{P0} . Even though the analytical equation of TSV was reported,⁴³ the capacitance from the TSV equation does not correspond to the experimental value requiring the improvement of the equation of C_{P0} .

2.3.2 Ohmic Model: Numerical Solution

Results from the finite element method (FEM) were reported to investigate geometric effects¹⁴ and to define resolution.^{44,45} Figure 2.8 shows FEM simulated curves with various

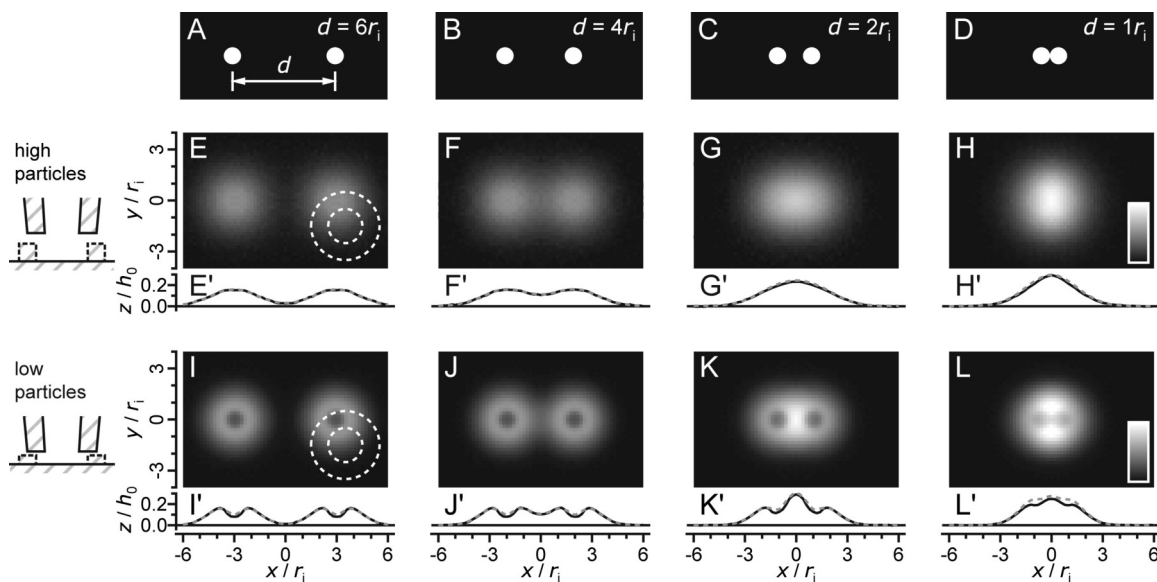


Figure 2.9 FEM simulated images of two cylindrical particles. (a-d) Actual topography. (e-h) calculated topography images for two high particles, $h_0 = r_i$, and a large pipette-sample distance $z_0 = 1.6 \cot r_i$. (i-l) images for low particle, $h_0 = r_i/2$, and a small pipette-sample distance, $z_0 = 0.6r_i$. Adapted from Rheinlaender et al. 2009.⁴⁴

geometries. When the ratio of geometry $RG = r_o/r_i$ is increased, the area of glass is increased. Consequentially the slope of current-distance becomes steeper (Figure 2.8b). The dependence on RG is also expected from approximate equations (2.6) and (2.7). The current-distance curve also has a dependency on the cone angle θ of the pipette. If the pipette is steeper, which means a smaller cone angle θ , the detection range is narrower.¹⁴

Rheinlaender et al. investigated the resolution of SICM using FEM simulation (Figure 2.9), and concluded that “the lateral resolution is three times the inner opening radius of the pipette, $d_0 = 3r_i$.”⁴⁴ Additionally, the ring shape of the particle image can be observed from their simulation (Figure 2.9I). This might be related to the pipette-sample distance because it cannot be observed in Figure 2.9E. It can be assumed that this ring shape is an artifact of SICM. However, by thinking reversely, this unique shape can be a clue to determine the pipette shape. From known various-sized small particles, the inner and outer radii of the pipette can be determined with the deconvolution algorithm, which was developed in AFM earlier.⁴⁶

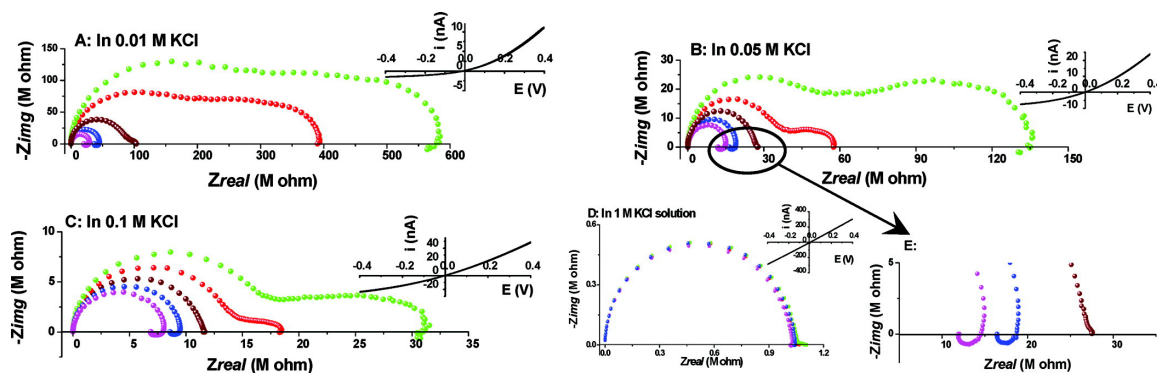


Figure 2.10 Nyquist plots of glass nanopipette. (A-D) different concentration of KCl solution in various offset voltage, green (-0.4 V), red (-0.2 V), wine (0 V), blue (0.2 V) and magenta (0.4 V). Adapted from Feng et al. 2010.⁴⁹

2.3.3 Estimating Tip Geometry

Like AFM, it is important to figure out the geometry of each pipette because the shape of the pipette is related to the resolution of SICM. The direct measurement of the pipette shape from scanning electron microscopy (SEM) or AFM is accurate, but it is hard to perform routinely. Caldwell et al. introduced one method to estimate the pipette geometry.⁴⁷ This method monitors the ion-current resistance while breaking the pipette end, then fits the resistance data to the analytical Nitz equation. One can find more information about the characterization of SICM pipettes on the recent review paper.⁴⁸

2.3.4 Electrical Properties

The measurement setup of SICM can be modeled as electrical circuit components, resistors and capacitors (RC). The basic idea of SICM is detecting the changes of the access resistance. It is important to find the proper circuit model between two electrodes to determine the signal bandwidth. Electro-impedance spectroscopy (EIS) was used to find the circuit model in electrochemistry, and Geddes summarized circuit models of the electrode-electrolyte interface.⁵⁰ Feng et al. reported multi-time constant features of a glass nanopore and suggested an RC model.⁴⁹ Figure 2.10 shows the multi-time constant appears when there is a low concentration with a negative offset voltage, in which ion-current is more hindered.

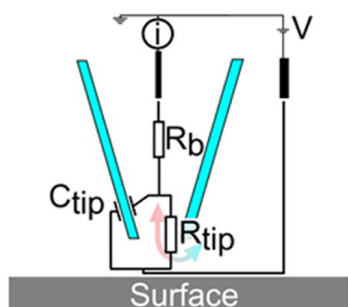


Table 1. Parameters Used to Fit the Impedance Data in Figure 4A–C, Using the Model in Figure 4D

distance	R_b/Ω	R_{tip}/Ω	C_{tip}/F
bulk	3.5×10^4	4.8×10^7	5.7×10^{-12}
200 nm	4.0×10^4	5.4×10^7	6.0×10^{-12}
100 nm	4.2×10^4	6.7×10^7	6.0×10^{-12}
50 nm	3.6×10^4	8.9×10^7	5.9×10^{-12}

Figure 2.11 Impedance model of SICM. Adapted from McKelvey et al. 2014.¹⁶

The impedance model of SICM can be more simplified because typically it is biased to a positive offset voltage (less hindered ion-current), and McKelvey et al. successfully found the bulk resistance, the tip resistance and the tip capacitance (Figure 2.11).¹⁶ Note the tip resistance (greater than 50 M Ω) is 1000 times higher than the bulk resistance (around 40 k Ω), and the tip capacitance is around 6 pF.

Another important electrical property is noise. The discussion of noise is still under debate. There are many papers focused on noise from the electrode-electrolyte interface.^{51–55} Many of them focused on the $1/f$ noise phenomena and tried to derive an equation without supporting experimental data,⁵⁶ or mismatched data.⁵⁷ One researcher argued that the noise obeys shot-noise, which is proportional to current,⁵⁴ while others argued the noise is proportional to the square of current.^{52,57} Even though Plamondon et al. found good agreement between their model and experimental data, they concluded carefully that “However, it should be remembered that biological solutions are more complex than simple monovalent electrolytes,... For example, it has been observed that the use of NaCl solution, instead of KCl, as external electrolyte, might double the voltage noise of the microtip.”⁵⁵

2.3.5 Ion Rectification and Poisson-Nernst-Planck Model

The rectification effect of micropipettes was reported over 50 years ago.⁵⁸ Thirty years ago, Plamondon and Gagné tried to explain this rectification effect using a diffusion model which includes an electroosmotic effect.⁵⁹ In 1997, Wei and Bard suggested that this rectification effect resulted from the surface charge of the glass pipette and the geometry of the

Table 2.2 Summary of some representative works on PNP equation

Problem	References
PNP, semiconductor	Gummel 1964 ⁶⁸
PNP	Brumleve 1978 ⁷⁴
NP, ion migration in pipette geometry	Fåhræus 1997, ⁷⁵ Fåhræus 1997 ⁷⁶
PNP, ion migration in pipette geometry	Cervera 2005, ⁶⁴ Cervera 2006 ⁶⁵
PNP, nano-fluidic channel, analytic solution	Vlassiouk 2008 ⁷⁷
PNP, charged membrane	Zheng 2011, ⁷⁸ Zheng 2011 ⁷⁹
PNP, mathematical analysis with steric effect	Ji 2012, ⁸⁰ Liu 2012 ⁸¹

pipette orifice.⁶⁰ Siwy et al. also emphasized the role of surface charges in the rectification effect.⁶¹ Many investigations have followed numerically^{62–65} and experimentally.⁶⁶

Sa et al. considered the rectification effect including the sample surface.¹⁹ This is a more realistic model to elucidate the pipette behavior on charged substrates. Clarke et al. also reported different current-distance behaviors on various kinds of samples.⁶⁷ Those findings reveal that the access resistance R_{AC} cannot be interpreted by simply depending on inversely proportional to the pipette-sample distance $1/z$.

The governing equation for interpreting this rectification is comprised of Poisson, Nernst-Planck (NP), and continuity equations. Moreover, those set is known as Poisson-Nernst-Planck (PNP) or Nernst-Planck-Poisson (NPP) equation. In the semiconductor field, the dynamics of electrons and holes is also illustrated by PNP equation. The most prominent advance to solve this problem was made by Gummel in 1964.⁶⁸ Even though the solution of PNP equation was beginning since mid of the 1960s, many types of researches are still developing to solve analytically^{69–72} and numerically.⁷³ Some representative works on PNP equation is summarized in Table 2.2.

2.4 Ph.D. in Context of Literature

Although SICM is considered as a powerful tool to investigate molecular-level biological study, slow imaging time is still a huge barrier. As discussed in Chapter 1, to obtain whole cell images, hopping mode is necessary, but the increased traveling length of the pipette is inevitable despite of many efforts to reduce imaging time in SICM. Those efforts

were focused on algorithmic approaches, including reducing the number of ROI pixels, optimizing pipette movement, and other tactics. Those efforts have been successful and well improved the optimization of SICM. Despite of those efforts, the physics related to nanopipettes is complex as reviewed in this chapter. Many phenomena were still remained and require clear explanations. Therefore, there is a room for improvement in the performance of SICM, given a deeper understanding of the nanopipette which can only be attained by the focused study.

This Ph.D. work starts with the capability of AFM for demonstrating structural inspection of mouse sperm samples in Chapter 4 to emphasize the convenience of sample preparation than the preparation steps of the high-resolution SEM. In Chapter 5, the advantage of SICM over AFM is displayed with soft biological samples. Although there were also many reports about these topics,^{23,82–84} it is not reported the direct comparison between SICM and AFM with the same scanning method. Chapter 6 demonstrates how SICM and AFM can be utilized for biological study in addition to their imaging features. However, this dissertation has focused not only on the capability of SICM but also the investigating models and the improvement of the instrument. In consequence, this review focused on instrumentation, and the more in-depth study for instrumentation is presented in Chapter 7.

References

- (1) Korchev, Y. E.; Bashford, C. L.; Milovanovic, M.; Vodyanoy, I.; Lab, M. J. Scanning ion conductance microscopy of living cells. *Biophys. J.* **1997**, *73*, 653–658.
- (2) Happel, P.; Thatenhorst, D.; Dietzel, I. D. Scanning ion conductance microscopy for studying biological samples. *Sensors* **2012**, *12*, 14983–15008.
- (3) Zhukov, A.; Richards, O.; Ostanin, V.; Korchev, Y.; Klenerman, D. A hybrid scanning mode for fast scanning ion conductance microscopy (SICM) imaging. *Ultra-microscopy* **2012**, *121*, 1–7.
- (4) Hansma, P. K.; Drake, B.; Marti, O.; Gould, S. A.; Prater, C. B. The scanning ion-conductance microscope. *Science* **1989**, *243*, 641–3.

- (5) Pastré, D.; Iwamoto, H.; Liu, J.; Szabo, G.; Shao, Z. Characterization of AC mode scanning ion-conductance microscopy. *Ultramicroscopy* **2001**, *90*, 13–19.
- (6) Shevchuk, A. I.; Gorelik, J.; Harding, S. E.; Lab, M. J.; Klenerman, D.; Korchev, Y. E. Simultaneous Measurement of Ca^{2+} and Cellular Dynamics: Combined Scanning Ion Conductance and Optical Microscopy to Study Contracting Cardiac Myocytes. *Biophys. J.* **2001**, *81*, 1759–1764.
- (7) Mann, S.; Hoffmann, G.; Hengstenberg, A.; Schuhmann, W.; Dietzel, I. Pulse-mode scanning ion conductance microscopy – a method to investigate cultured hippocampal cells. *J. Neurosci. Methods* **2002**, *116*, 113–117.
- (8) Happel, P.; Hoffmann, G.; Mann, S. A.; Dietzel, I. D. Monitoring cell movements and volume changes with pulse-mode scanning ion conductance microscopy. *J. Microsc.* **2003**, *212*, 144–151.
- (9) Novak, P.; Li, C.; Shevchuk, A. I.; Stepanyan, R.; Caldwell, M.; Hughes, S.; Smart, T. G.; Gorelik, J.; Ostanin, V. P.; Moss, G. W. J.; Frolenkov, G. I.; Klenerman, D.; Korchev, Y. E. Nanoscale live-cell imaging using hopping probe ion conductance microscopy. *Nat. Methods* **2009**, *6*, 279–282.
- (10) Martin, Y.; Williams, C.; Wickramasinghe, H. K. Atomic force microscope–force mapping and profiling on a sub 100-Å scale. *J. Appl. Phys.* **1987**, *61*, 4723–4729.
- (11) Albrecht, T.; Grütter, P.; Horne, D.; Rugar, D. Frequency modulation detection using high-Q cantilevers for enhanced force microscope sensitivity. *J. Appl. Phys.* **1991**, *69*, 668–673.
- (12) García, R.; Perez, R. Dynamic atomic force microscopy methods. *Surf. Sci. Rep.* **2002**, *47*, 197–301.
- (13) Proksch, R.; Lal, R.; Hansma, P. K.; Morse, D.; Stucky, G. Imaging the internal and external pore structure of membranes in fluid: TappingMode scanning ion conductance microscopy. *Biophys. J.* **1996**, *71*, 2155–7.
- (14) Edwards, M. A.; Williams, C. G.; Whitworth, A. L.; Unwin, P. R. Scanning ion conductance microscopy: a model for experimentally realistic conditions and image interpretation. *Anal. Chem.* **2009**, *81*, 4482–92.
- (15) Li, P.; Liu, L.; Wang, Y.; Yang, Y.; Zhang, C.; Li, G. Phase modulation mode of scanning ion conductance microscopy. *Appl. Phys. Lett.* **2014**, *105*, 053113.

- (16) McKelvey, K.; Perry, D.; Byers, J. C.; Colburn, A. W.; Unwin, P. R. Bias modulated scanning ion conductance microscopy. *Anal. Chem.* **2014**, *86*, 3639–46.
- (17) Chen, C. C.; Baker, L. A. Effects of pipette modulation and imaging distances on ion currents measured with scanning ion conductance microscopy (SICM). *Analyst* **2011**, *136*, 90–7.
- (18) Perry, D.; Al Botros, R.; Momotenko, D.; Kinnear, S. L.; Unwin, P. R. Simultaneous nanoscale surface charge and topographical mapping. *ACS Nano* **2015**, *9*, 7266–7276.
- (19) Sa, N.; Lan, W.-J.; Shi, W.; Baker, L. A. Rectification of Ion Current in Nanopipettes by External Substrates. *ACS Nano* **2013**, *7*, 11272–11282.
- (20) McKelvey, K.; Kinnear, S. L.; Perry, D.; Momotenko, D.; Unwin, P. R. Surface charge mapping with a nanopipette. *J. Am. Chem. Soc.* **2014**, *136*, 13735–44.
- (21) Perry, D.; Nadappuram, B. P.; Momotenko, D.; Voyias, P. D.; Page, A.; Tripathi, G.; Frenguelli, B. G.; Unwin, P. R. Surface charge visualization at viable living cells. *J. Am. Chem. Soc.* **2016**, *138*, 3152–3160.
- (22) Takahashi, Y.; Murakami, Y.; Nagamine, K.; Shiku, H.; Aoyagi, S.; Yasukawa, T.; Kanzaki, M.; Matsue, T. Topographic imaging of convoluted surface of live cells by scanning ion conductance microscopy in a standing approach mode. *Phys. Chem. Chem. Phys.* **2010**, *12*, 10012–10017.
- (23) Ushiki, T.; Nakajima, M.; Choi, M.; Cho, S.-J.; Iwata, F. Scanning ion conductance microscopy for imaging biological samples in liquid: A comparative study with atomic force microscopy and scanning electron microscopy. *Micron* **2012**, *43*, 1390–1398.
- (24) Liu, B. C.; Lu, X. Y.; Song, X.; Lei, K. Y.; Alli, A. A.; Bao, H. F.; Eaton, D. C.; Ma, H. P. Scanning ion conductance microscopy: A nanotechnology for biological studies in live cells. *Front. Physiol.* **2013**, *3*, 483.
- (25) Cappella, B.; Baschieri, P.; Frediani, C.; Miccoli, P.; Ascoli, C. Improvements in AFM imaging of the spatial variation of force - distance curves: on-line images. *Nanotechnology* **1997**, *8*, 82.

- (26) Hosaka, S.; Morimoto, T.; Kuroda, H.; Minomoto, Y.; Kembo, Y.; Koyabu, H. New AFM imaging for observing a high aspect structure. *Appl. Surf. Sci.* **2002**, *188*, 467–473.
- (27) Hosaka, S.; Hosoki, S.; Takada, K. Japanese patent no. *P2936545 (submitted date 1988.6. 24)* **1988**.
- (28) Kado, H.; Yamamoto, S.-i.; Yokoyama, K.; Tohda, T.; Umetani, Y. Observation of contact holes by atomic force microscopy with a ZnO whisker tip. *J. Appl. Phys.* **1993**, *74*, 4354–4356.
- (29) Van Der Werf, K. O.; Putman, C. A.; de Grooth, B. G.; Greve, J. Adhesion force imaging in air and liquid by adhesion mode atomic force microscopy. *Appl. Phys. Lett.* **1994**, *65*, 1195–1197.
- (30) Rosa-Zeiser, A.; Weilandt, E.; Hild, S.; Marti, O. The simultaneous measurement of elastic, electrostatic and adhesive properties by scanning force microscopy: pulsed-force mode operation. *Meas. Sci. Technol.* **1997**, *8*, 1333.
- (31) Novak, P.; Shevchuk, A.; Ruenraroengsak, P.; Miragoli, M.; Thorley, A. J.; Klennerman, D.; Lab, M. J.; Tetley, T. D.; Gorelik, J.; Korchev, Y. E. Imaging single nanoparticle interactions with human lung cells using fast ion conductance microscopy. *Nano Lett.* **2014**, *14*, 1202–7.
- (32) Jung, G.-E.; Noh, H.; Shin, Y. K.; Kahng, S.-J.; Baik, K. Y.; Kim, H.-B.; Cho, N.-J.; Cho, S.-J. Closed-loop ARS mode for scanning ion conductance microscopy with improved speed and stability for live cell imaging applications. *Nanoscale* **2015**, *7*, 10989–10997.
- (33) Li, P.; Liu, L.; Yang, Y.; Wang, Y.; Li, G. In-Phase Bias Modulation Mode of Scanning Ion Conductance Microscopy With Capacitance Compensation. *IEEE Trans. Ind. Electron.* **2015**, *62*, 6508–6518.
- (34) Zhuang, J.; Li, Z.; Jiao, Y. Double micropipettes configuration method of scanning ion conductance microscopy. *Rev. Sci. Instrum.* **2016**, *87*, 073703.
- (35) Ida, H.; Takahashi, Y.; Kumatani, A.; Shiku, H.; Matsue, T. High Speed Scanning Ion Conductance Microscopy for Quantitative Analysis of Nanoscale Dynamics of Microvilli. *Anal. Chem.* **2017**, *89*, 6015–6020.

- (36) Li, P.; Zhang, C.; Liu, L.; Wang, Y.; Xi, N.; Wejinya, U. C.; Li, G. In *IEEE/ASME Int. Conf. Adv. Intell. Mechatron.* 2013, pp 89–93.
- (37) Andersson, S. B.; Abramovitch, D. Y. In *Amer. Contr. Conf.* 2007, pp 3516–3521.
- (38) Andersson, S. B.; Pao, L. Y. In *Amer. Contr. Conf.* 2012, pp 2485–2490.
- (39) Li, G.; Li, P.; Wang, Y.; Wang, W.; Xi, N.; Liu, L. Efficient Imaging and Real-Time Display of Scanning Ion Conductance Microscopy Based on Block Compressive Sensing. *Int. J. Optomechatronics* **2014**, *8*, 218–227.
- (40) Kang, M.; Momotenko, D.; Page, A.; Perry, D.; Unwin, P. R. Frontiers in Nano-scale Electrochemical Imaging: Faster, Multifunctional, and Ultrasensitive. *Langmuir* **2016**, *32*, 7993–8008.
- (41) Kim, J.; Kim, S.-O.; Cho, N.-J. Alternative configuration scheme for signal amplification with scanning ion conductance microscopy. *Rev. Sci. Instrum.* **2015**, *86*, 023706.
- (42) Nitz, H.; Kamp, J.; Fuchs, H. A combined scanning ion-conductance and shear-force microscope. *Probe Microscopy* **1998**, *1*, 187–200.
- (43) Wang, F. J.; Zhu, Z. M.; Yang, Y. T.; Liu, X. X.; Ding, R. X. Capacitance characterization of tapered through-silicon-via considering MOS effect. *Microelectron. J.* **2014**, *45*, 205–210.
- (44) Rheinlaender, J.; Schäffer, T. E. Image formation, resolution, and height measurement in scanning ion conductance microscopy. *J. Appl. Phys.* **2009**, *105*, 094905.
- (45) Rheinlaender, J.; Schaffer, T. E. Lateral Resolution and Image Formation in Scanning Ion Conductance Microscopy. *Anal. Chem.* **2015**, *87*, 7117–24.
- (46) Villarrubia, J. Algorithm for scanned probe microscope image simulation, surface reconstruction, and tip estimation. *J. Res. Natl. Inst. Stand. Technol.* **1997**, *102*, 425–454.
- (47) Caldwell, M.; Del Linz, S. J. L.; Smart, T. G.; Moss, G. W. J. Method for estimating the tip geometry of scanning ion conductance microscope pipets. *Anal. Chem.* **2012**, *84*, 8980–8984.
- (48) Tognoni, E.; Baschieri, P.; Ascoli, C.; Pellegrini, M.; Pellegrino, M. Characterization of tip size and geometry of the pipettes used in scanning ion conductance microscopy. *Micron* **2016**, *83*, 11–18.

- (49) Feng, J.; Liu, J.; Wu, B.; Wang, G. Impedance Characteristics of Amine Modified Single Glass Nanopores. *Anal. Chem.* **2010**, *82*, 4520–4528.
- (50) Geddes, L. Historical evolution of circuit models for the electrode-electrolyte interface. *Ann. Biomed. Eng.* **1997**, *25*, 1–14.
- (51) Flasterstein, A. Voltage fluctuations of metal-electrolyte interfaces in electrophysiology. *Med. Biol. Eng.* **1966**, *4*, 583–588.
- (52) Hooge, F. N. $1/f$ noise is no surface effect. *Phys. Lett. A* **1969**, *29*, 139–140.
- (53) Stevens, C. F. Inferences about membrane properties from electrical noise measurements. *Biophys. J.* **1972**, *12*, 1028–1047.
- (54) Läuger, P. Shot noise in ion channels. *Biochim. Biophys. Acta* **1975**, *413*, 1–10.
- (55) Plamondon, R.; Gagne, S.; Poussart, D. J.-M. Power spectrum density analysis of electrical noise in glass microelectrodes. *IEEE Trans. Biomed. Eng.* **1984**, 428–434.
- (56) Hassibi, A.; Navid, R.; Dutton, R. W.; Lee, T. H. Comprehensive study of noise processes in electrode electrolyte interfaces. *J. Appl. Phys.* **2004**, *96*, 1074–1082.
- (57) Powell, M.; Sa, N.; Davenport, M.; Healy, K.; Vlassiouk, I.; Letant, S.; Baker, L.; Siwy, Z. Noise properties of rectifying nanopores. *J. Phys. Chem. C* **2011**, *115*, 8775–8783.
- (58) Emck, J. Some Anomalous Electrical Effects in Microelectrodes. *Phys. Med. Biol.* **1959**, *3*, 339.
- (59) Plamondon, R.; Gagne, S. Studies on electroosmotic effects in glass microelectrodes-improvement of microelectrode selection. *IEEE Trans. Biomed. Eng.* **1984**, 512–519.
- (60) Wei, C.; Bard, A. J.; Feldberg, S. W. Current rectification at quartz nanopipet electrodes. *Anal. Chem.* **1997**, *69*, 4627–4633.
- (61) Siwy, Z.; Heins, E.; Harrell, C. C.; Kohli, P.; Martin, C. R. Conical-nanotube ion-current rectifiers: the role of surface charge. *J. Am. Chem. Soc.* **2004**, *126*, 10850–10851.
- (62) Wang, X.; Xue, J.; Wang, L.; Guo, W.; Zhang, W.; Wang, Y.; Liu, Q.; Ji, H.; Ouyang, Q. How the geometric configuration and the surface charge distribution influence the ionic current rectification in nanopores. *J. Phys. D: Appl. Phys.* **2007**, *40*, 7077.

- (63) Ramírez, P.; Apel, P. Y.; Cervera, J.; Mafé, S. Pore structure and function of synthetic nanopores with fixed charges: tip shape and rectification properties. *Nanotechnology* **2008**, *19*, 315707.
- (64) Cervera, J.; Schiedt, B.; Ramírez, P. A Poisson/Nernst-Planck model for ionic transport through synthetic conical nanopores. *Europhys. Lett.* **2005**, *71*, 35.
- (65) Cervera, J.; Schiedt, B.; Neumann, R.; Mafé, S.; Ramírez, P. Ionic conduction, rectification, and selectivity in single conical nanopores. *J. Chem. Phys.* **2006**, *124*, 104706.
- (66) Sa, N.; Baker, L. A. Experiment and Simulation of Ion Transport through Nanopipettes of Well-Defined Conical Geometry. *J. Electrochem. Soc.* **2013**, *160*, H376–H381.
- (67) Clarke, R. W.; Zhukov, A.; Richards, O.; Johnson, N.; Ostanin, V.; Klenerman, D. Pipette-surface interaction: Current enhancement and intrinsic force. *J. Am. Chem. Soc.* **2013**, *135*, 322–329.
- (68) Gummel, H. K. A self-consistent iterative scheme for one-dimensional steady state transistor calculations. *IEEE Trans. Electron Devices* **1964**, *11*, 455–465.
- (69) Golovnev, A.; Trimper, S. Exact solution of the Poisson–Nernst–Planck equations in the linear regime. *J. Chem. Phys.* **2009**, *131*, 114903.
- (70) Golovnev, A.; Trimper, S. Analytical solution of the Poisson–Nernst–Planck equations in the linear regime at an applied dc-voltage. *J. Chem. Phys.* **2011**, *134*, 154902.
- (71) Zhou, S.; Zhang, G. Approximate analytical expressions for electrical potential distribution and surface charge density/surface potential relationship for planar, cylindrical, and spherical entities immersed in a general electrolyte solution. *Colloids Surf., A* **2011**, *385*, 28–39.
- (72) Pabst, M. Analytical solution of the Poisson-Nernst-Planck equations for an electrochemical system close to electroneutrality. *J. Chem. Phys.* **2014**, *140*, 224113.
- (73) Liu, W.; Xu, H. A complete analysis of a classical Poisson–Nernst–Planck model for ionic flow. *J. Differ. Equ.* **2015**, *258*, 1192–1228.
- (74) Brumleve, T. R.; Buck, R. P. Numerical solution of the Nernst-Planck and Poisson equation system with applications to membrane electrochemistry and solid state physics. *J. Electroanal. Chem. Interfacial Electrochem.* **1978**, *90*, 1–31.

- (75) Fåhræus, C.; Borglid, K.; Grampp, W. Properties of electrolyte-filled glass micro-electrodes: an experimental study. *J. Neurosci. Methods* **1997**, *78*, 15–28.
- (76) Fåhræus, C.; Grampp, W. Properties of electrolyte-filled glass microelectrodes: a model analysis. *J. Neurosci. Methods* **1997**, *78*, 29–45.
- (77) Vlassiouk, I.; Smirnov, S.; Siwy, Z. Nanofluidic ionic diodes. Comparison of analytical and numerical solutions. *ACS Nano* **2008**, *2*, 1589–1602.
- (78) Zheng, Q.; Chen, D.; Wei, G.-W. Second-order Poisson–Nernst–Planck solver for ion transport. *J. Comput. Phys.* **2011**, *230*, 5239–5262.
- (79) Zheng, Q.; Wei, G.-W. Poisson–Boltzmann–Nernst–Planck model. *J. Chem. Phys.* **2011**, *134*, 194101.
- (80) Ji, S.; Liu, W. Poisson–Nernst–Planck systems for ion flow with density functional theory for hard-sphere potential: I–V relations and critical potentials. Part I: analysis. *J. Dyn. Differ. Equ.* **2012**, 1–29.
- (81) Liu, W.; Tu, X.; Zhang, M. Poisson–Nernst–Planck systems for ion flow with density functional theory for hard-sphere potential: I–V relations and critical potentials. Part II: numerics. *J. Dyn. Differ. Equ.* **2012**, *24*, 985–1004.
- (82) Rheinlaender, J.; Geisse, N. A.; Proksch, R.; Schaffer, T. E. Comparison of scanning ion conductance microscopy with atomic force microscopy for cell imaging. *Langmuir* **2011**, *27*, 697–704.
- (83) Zhang, S.; Cho, S. J.; Busutil, K.; Wang, C.; Besenbacher, F.; Dong, M. Scanning ion conductance microscopy studies of amyloid fibrils at nanoscale. *Nanoscale* **2012**, *4*, 3105–3110.
- (84) Seifert, J.; Rheinlaender, J.; Novak, P.; Korchev, Y. E.; Schäffer, T. E. Comparison of Atomic Force Microscopy and Scanning Ion Conductance Microscopy for Live Cell Imaging. *Langmuir* **2015**, *31*, 6807–6813.

Chapter 3

Methodology

This chapter provides the foundation of techniques which is used in this dissertation. From the concept of force sensing by a cantilever, the first section describes how atomic force microscopy (AFM) reconstructs the morphological height from measured force, how AFM analyzes the material deformation from the basic model, and how AFM extracts forces from the cantilever dynamics. The second section also explains the principles of scanning ion-conductance microscopy (SICM), and then discussing the principle of the lock-in detection technique to emphasize the different usage of the modulation technique from that of AFM. Finally, the practical information of numerical analysis is presented.

3.1 Atomic Force Microscopy (AFM)

3.1.1 Operating Principle of AFM

A cantilever is a key part of atomic force microscopy (AFM). Usually, AFM uses a laser beam to detect the bending of the cantilever. The illuminated laser beam on the cantilever is reflected, then a position sensitive photodiode (PSPD) receives the beam. When the cantilever as a mirror is bent, the reflection beam path is changed so that the PSPD can calculate how much the cantilever is bent. This bending amount Δ is related to force by Hooke's law, approximately

$$F = k \cdot \Delta \quad (3.1)$$

where F is the applied force to the cantilever, and k is the spring constant of the cantilever. Thus, AFM is named after its nature to detect forces by monitoring bending amount of a cantilever. This behavior is illustrated in Figure 3.1.

Figure 3.2 shows how to reconstruct height from the force. If the cantilever is above an area A , then the distance $z(x = A)$ can be examined how far the cantilever moves to the surface from the initial height to reach a certain force, which is known as a setpoint. Then on another area B , the distance $z(x = B)$ also can be obtained to maintain the force

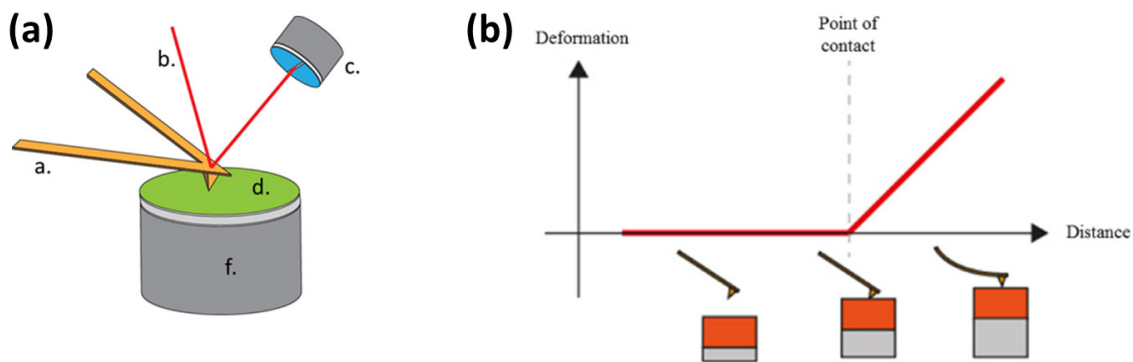


Figure 3.1 Schematics of AFM and force distance curve on a solid sample. (a) AFM consists of a. cantilever and tip, b. laser beam, c. photosensitive photodiode, d. sample, f. piezo-actuator. (b) After approaching at the point of contact, the tip is starting to bend by force. Adapted from Kasas, Longo and Dietler 2013.¹

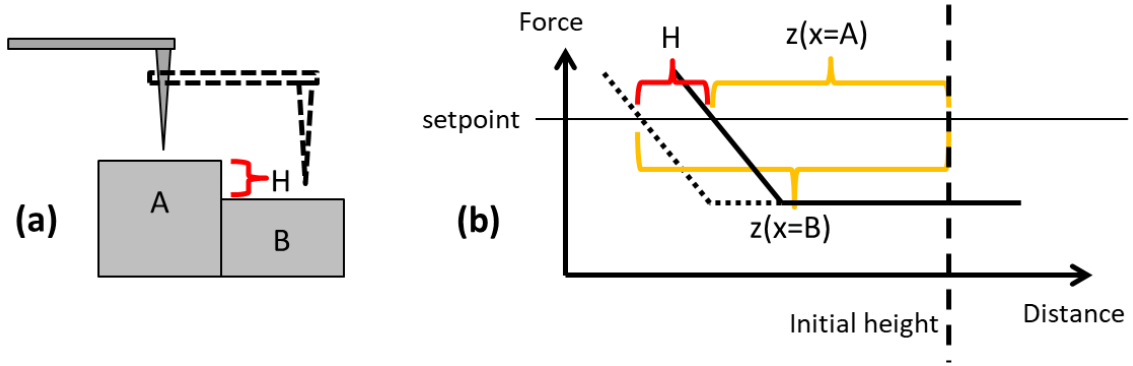


Figure 3.2 Schematic of reconstruction of height of AFM.

at the same setpoint. Then the relative height, H can be calculated by subtraction of two distance. This is the key concept of mapping height of surface variations in every scanning probe technique. If the signal of a probe has a monotonic relationship with the distance between the probe and the surface, then any probes can be used for a scanning probe and can map a surface morphology. The probe signal is not necessary to be linear depending on the distance, because the position is determined by the scanner or the actuator. Only virtue, which the probe must have, is the uniqueness of the position dependency.

3.1.2 Force Spectroscopy

The term of spectroscopy is strictly used to study the matter-radiation interaction, but force spectroscopy is widely used for investigating the interaction between matters or molecules. SPM is not designed for microscopy, so mapping images are not the only main functionality of SPM.² The most promising feature of AFM is force spectroscopy allowing one to investigate the mechanical properties of a sample.

The force-distance curves in Figure 3.1b and Figure 3.2b are the simplest case of the rigid materials, and the sample morphology in those figures is not changed by force from the AFM tip. However, many biological materials are elastic. Hence, the soft sample is easily deformed and indented by the loading force of the AFM tip. Figure 3.3 shows the typical force-distance curves with and without sample deformation. The force-distance curve on a soft sample is sagged in contrast to the curve of a rigid sample. So, one can obtain the

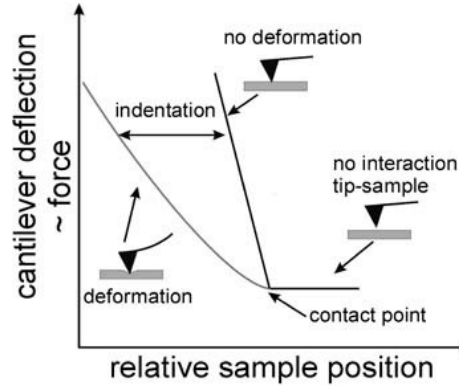


Figure 3.3 Indentation determination from AFM force curve data. Adapted from Lekka and Kulik 2006.³

indentation depth δ by comparing two curves for certain loading forces.

Hertz proposed the first indentation model with the assumption of no adhesion forces in 1881. Since then several theoretical works have been succeeded on the contact mechanics such as Johnson-Kendall-Roberts (JKR) and Derjaguin-Muller-Toporov (DMT).⁴ In this dissertation, Sneddon extension⁵ of Hertzian model is used for simplicity. For paraboloidal tip, the indentation depth δ and the loading force F have a following relation,

$$F(\delta) = \frac{4\sqrt{3}}{3} E' \delta^{1.5} \quad (3.2)$$

where E' is the reduced Young's modulus and R is the radius of the tip. For four-sided pyramid shaped tips, the force-indentation is

$$F(\delta) = \frac{\tan(\alpha)}{\pi\sqrt{2}} E' \delta^2 \quad (3.3)$$

where α is the face angle. The reduced Young's modulus is calculated by

$$\frac{1}{E'} = \frac{1 - \nu_{tip}^2}{E_{tip}} + \frac{1 - \nu_{sample}^2}{E_{sample}} \quad (3.4)$$

with the Poisson ratio ν and the modulus of two materials, the tip and the sample. However, for biology study, assuming the tip is much more rigid than the sample $E_{tip} \gg E_{sample}$, then the reduced Young's modulus becomes

$$\frac{1}{E'} = \frac{1 - \nu_{tip}^2}{E_{tip}}. \quad (3.5)$$

Then, from the force-distance curve data and equations (3.4) and (3.5), the Young's modulus of a specific area can be examined.

One undetermined variable is the spring constant k of the cantilever to calculate the force from the cantilever bending response Δ . The spring constant k can be calculated by the geometrical dimension of the cantilever, or calibrated by a standard sample.⁶ A thermal vibrational calibration is used in the work of this dissertation to determine the spring constant.⁷ The thermal vibrational calibration can be performed at the beginning of every measurement reducing the measurement steps. The thermal vibrational calibration assumes that the thermal energy is equal to the average energy of a harmonic oscillator,

$$\left\langle \frac{1}{2}kz^2 \right\rangle = \frac{1}{2}k_B T \quad (3.6)$$

where z is the displacement of the cantilever, k_B is the Boltzmann constant, and T is the absolute temperature. The average of square of displacement $\langle z^2 \rangle$ can be measured by power spectrum density. Then, the spring constant can be obtained from

$$k = k_B T / P \quad (3.7)$$

with the integral of the power spectrum density of displacement, P .

3.1.3 Modulation Technique

The dynamics of a cantilever is simply modeled by a simple harmonic oscillator

$$m\ddot{z} + \lambda\dot{z} + kz = F(z) \quad (3.8)$$

where the dot operator \dot{z} is Newton notation for time derivatives, z is the displacement, m is the mass of the tip, λ is the damping term, k is the spring constant of the cantilever and F is the external forces. The natural angular frequency ω_0 and the quality factor Q are given by

$$\omega_0 = \sqrt{k/m} \quad (3.9)$$

$$Q = \omega_0 / \lambda. \quad (3.10)$$

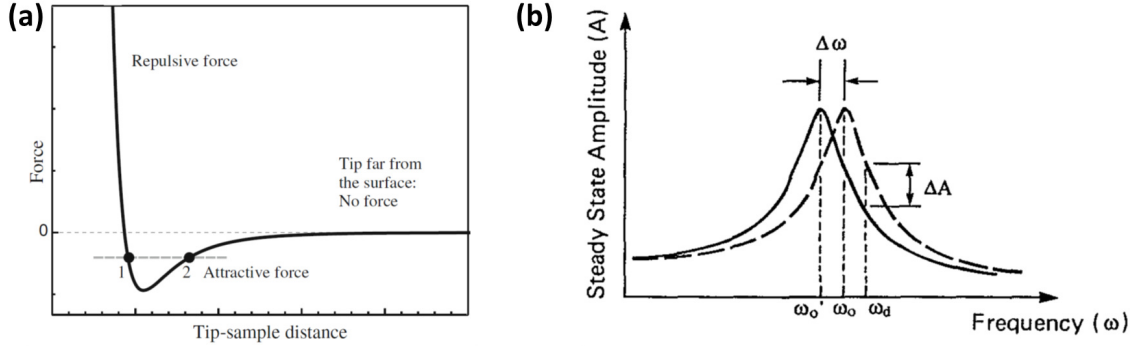


Figure 3.4 The qualitative sketch of the force curve (a) and the resonance frequency shift (b) of the cantilever under force fields. Adapted from Voigtländer 2016⁸ and Albrecht et al. 1991.⁹

For small displacements from the equilibrium position, the external force can be expressed by

$$F(z) = F_0 + (z - z_0) \cdot \left. \frac{\partial F}{\partial z} \right|_{z_0} \quad (3.11)$$

where F_0 is the force at the point z . Rearrangement of equations (3.8) and (3.11) becomes

$$m\ddot{z} + \lambda\dot{z} + k_e z = F_0 + z_0 \cdot \left. \frac{\partial F}{\partial z} \right|_{z_0} \quad (3.12)$$

with the effective spring constant,

$$k_e = k - \left. \frac{\partial F}{\partial z} \right|_{z_0}. \quad (3.13)$$

This result indicates that the effective spring constant changes under force gradient and the effective natural angular frequency ω_e is also changed by the external force gradient,

$$\omega_e = \sqrt{\frac{1}{m} \left(k - \left. \frac{\partial F}{\partial z} \right|_{z_0} \right)}. \quad (3.14)$$

Figure 3.4 shows the qualitative sketch of the force curve and the resonance shift of a cantilever under force gradient. The cantilever has no force when the tip is far from the surface. While the tip is approaching the sample, the tip is starting to feel the attractive force. If the tip is sufficiently close to the sample, the tip and the sample repulse each other. The resonance frequency would be shifted to left when the cantilever is operating in the attractive force regime, e.g. point 2 in Figure 3.4a, whereas the resonance frequency would

be shifted towards right when the cantilever is in the repulsive force regime, e.g. point 1 in Figure 3.4a.

There are two ways to extract the distance information from this resonance shift. One is to vibrate a cantilever at a certain frequency near the resonance frequency, and to read the amplitude changes. If the tip is approaching the attractive regime, then the resonance frequency would be shifted from ω_0 to ω'_0 . While a cantilever is oscillated at the operating frequency ω_d , the amplitude response would be decreased by ΔA as illustrated in Figure 3.4b. Hence, the amplitude will be modulated by depending on the distance, this mode is known as amplitude modulation atomic force microscopy (AM-AFM). The well-known synonyms for AM-AFM are tapping-mode AFM^{10,11} illustrating a tip slightly taps the surface, and non-contact mode (NCM) AFM from the belief of a cantilever is operated in the attractive regime.

The minimum detectable force is given by

$$\delta F_{min} = \sqrt{\frac{2k \cdot k_B T \cdot BW}{\omega_0 Q \langle z_{osc}^2 \rangle}} \quad (3.15)$$

where BW is the measurement bandwidth, and $\langle z_{osc}^2 \rangle$ is the mean-square amplitude of the cantilever vibration.⁹ The settling time of amplitude τ_{AM} is

$$\tau_{AM} = \frac{2Q}{\omega_0}. \quad (3.16)$$

From equations (3.15) and (3.16), one can conclude that high- Q factor offers high-sensitivity but slow-response, and low- Q factor offers low-sensitivity but fast-response. AM-AFM has been successfully utilized in air over three decades because of moderate Q factor of the cantilever in air. The Q value of AM-AFM cantilevers in air is around 300 to 500.

However, it is impractical to use AM-AFM in vacuum because of very high- Q factor. The Q factor of a cantilever is higher than 10^4 in vacuum, and this high Q factor lags the settling time t_A seriously. To overcome this slow response, another modulation technique was introduced in 1991.⁹ This mode is vibrating the cantilever at its resonance frequency

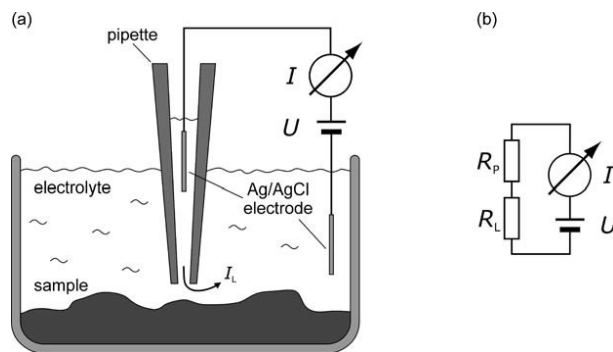


Figure 3.5 Schematic of a basic SICM setup. Adapted from Schäffer, Anczykowski and Fuchs 2006.¹⁴

while tracking the resonance frequency as the distance signal. So, the frequency is modulated by changing the distance, this mode is known as frequency modulation atomic force microscopy (FM-AFM).

It is the most important topic in AFM to research the dynamics of cantilevers. In this section, the cantilever is assumed as a simple harmonic oscillator, but in a real situation, it is not valid. There is a series of work on this topic, and one may start from García and Pérez 2002,¹² and García 2011.¹³ In this Ph.D. research, AM-AFM was mainly employed because AM-AFM is commercially available and well-mature for imaging.

3.2 Scanning Ion-Conductance Microscopy (SICM)

3.2.1 Operational Principle of SICM

As the dynamics of a cantilever is the key physics of AFM, the ion-current flow is the key phenomenon of SICM. Most SICM uses two electrodes unlike with a typical electrochemical experimental setup, which uses three or more electrodes in general. Because many electrochemical experiments have interest in reactions of electrode-electrolyte interfaces, but not in the migration of ions. Electrochemical experiment is necessary to reduce the migration effect or the solution resistance using the additional electrode. SICM is also working in an electrochemical cell, but the main physics of SICM is ion-migration. Therefore, SICM uses two identical stable electrodes in general to ignore electrochemical reactions of electrode-electrolyte interface. Additionally, physiological condition should be maintained

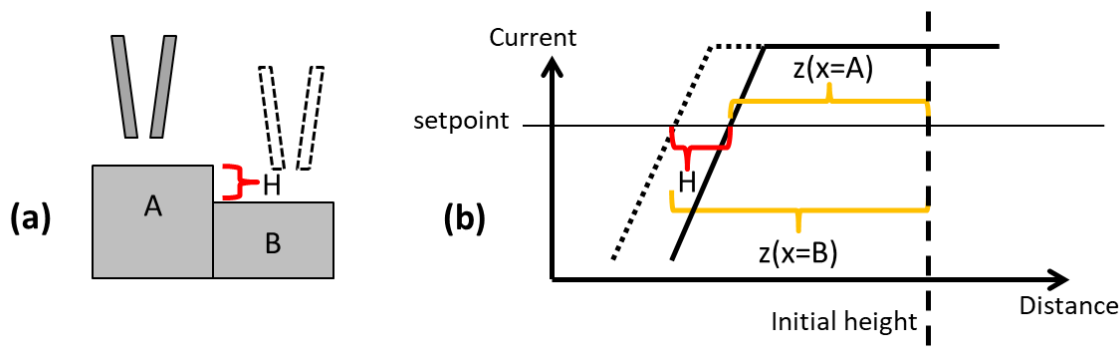
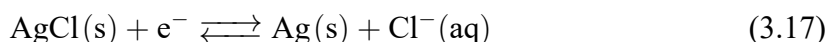


Figure 3.6 Schematic of reconstruction of the height of SICM.

because most applications of SICM are biological studies. Therefore, it is natural to use silver/silver chloride electrodes with the chemical reaction,



where the phase is denoted in parenthesis; (s) is a solid phase, (aq) is an aqueous phase. e^- is the element negative charge or an electron. Figure 3.5 shows a basic SICM setup. The working electrode is inserted in the pipette, and reference electrode is located in the bulk solution. When electrostatic potential is applied between two electrodes, the current start to flow between two electrodes. The pipette apex and the sample surface can make a small channel, in which only ions can migrate. If the pipette and the sample is getting very close, and the channel becomes narrower, then the flow of ions are hindered.

Figure 3.6 shows the qualitative schematic of the current-distance relationship of SICM. If the pipette is located far from the surface at the initial height in Figure 3.6b, there is no significant variation of ion current. When the pipette closely approaches the surface of the area A, the current starts to decrease because of the squeezed channel (solid black line). The same experiment can be conducted at the area B, where the height is lower than the area A. The current starts decreased at the lower position than on the area A (dotted black line). Like the height mapping logic in AFM as described in Subsection 3.1.1, SICM can also map the height between two positions $z(x = B) - z(x = A)$ at a certain ion current value, setpoint. It is also not necessary to approach every single point, but it is possible to map an image by maintaining the ion-current to the setpoint with feedback control. If

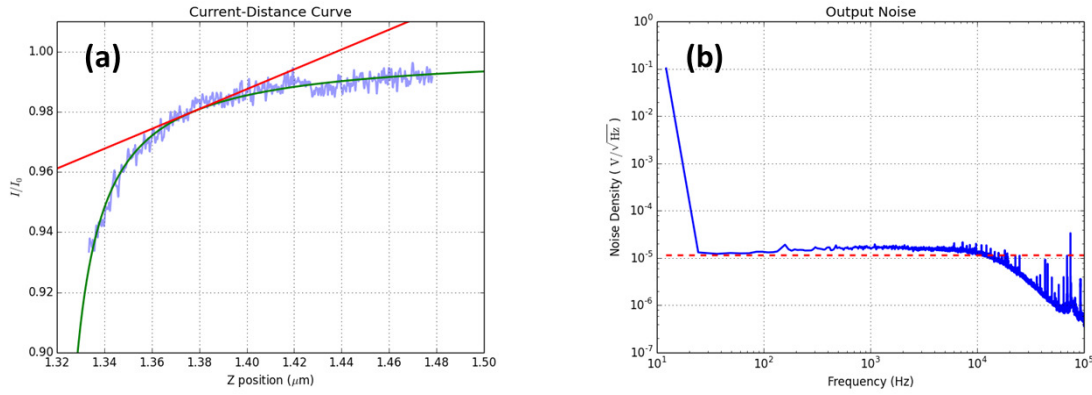


Figure 3.7 Experimental data of the current distance curve and the noise spectrum of the SICM pipette.

the morphological variation is not too large, then the exactly same scanning method can be applied as the way of AFM.

3.2.2 Vertical Resolution of SICM

It is relatively easier to estimate the height resolution (vertical resolution) of SICM than the spatial resolution (lateral resolution) of SICM. Figure 3.7 shows experimental data of the current-distance curve with 0.1 V bias voltage and the noise spectrum of the pipette without sample engagement. This solid green line in Figure 3.7a is a fitted curve from the analytical model,

$$\frac{I}{I_0} = \left(1 + \frac{A}{z - z_0}\right)^{-1} \quad (3.18)$$

with the parameters of $I_0 = 0.6433 \text{ nA}$, $A = 1.214 \times 10^{-3}$ and $z_0 = 1.318 \mu\text{m}$. The red solid line is the tangential slope of $0.21 \text{ nA } \mu\text{m}^{-1}$ at 98 % current point. The measured noise density at 1 kHz is $16.75 \mu\text{V}/\text{Hz}^{1/2}$ with the transimpedance gain of 10^9 . Then the expected root mean squared (RMS) noise with 1 kHz bandwidth is

$$\frac{(16.75 \times 10^{-6} \text{ nA}/\sqrt{\text{Hz}}) \cdot (\sqrt{1 \text{ kHz}})}{(0.21 \text{ nA } \mu\text{m}^{-1})} = 2.5 \text{ nm(RMS)}.$$

This value well corresponds to the value of some literature, which expects the vertical resolution is less 10 nm.^{15–17}

3.2.3 Lock-in Amplifier and Note on AC-mode SICM

The amplitude A at the frequency f_r and the phase difference θ from the reference signal $\cos(2\pi f_r t)$ can be extracted from a signal by the lock-in amplifier (LIA). This can be accomplished by mixing the reference signal and the target signal $A \cos(2\pi f_s t + \theta)$. More specifically, the in-phase signal I is multiplied the target signal by the reference signal, and the quadrature signal Q is multiplied the target signal by the 90°-shifted reference signal,

$$I = A \cos(2\pi f_s t + \theta) \cdot \cos(2\pi f_r t) \quad (3.19)$$

$$Q = A \cos(2\pi f_s t + \theta) \cdot \sin(-2\pi f_r t) \quad (3.20)$$

and with the trigonometric product identities,

$$I = \frac{A}{2} \{ \cos(2\pi(f_s - f_r)t + \theta) + \cos(2\pi(f_s + f_r)t + \theta) \} \quad (3.21)$$

$$Q = \frac{A}{2} \{ \sin(2\pi(f_s - f_r)t + \theta) - \sin(2\pi(f_s + f_r)t + \theta) \}. \quad (3.22)$$

If the target signal contains the reference frequency component $f_s = f_r$, and low-pass filtering with a proper time constant $\tau \ll 1/f_r$ is applied to eliminate the $f_s + f_r$ frequency component, the in-phase and quadrature signals become

$$I \simeq \frac{A}{2} \cos(\theta) \quad (3.23)$$

$$Q \simeq \frac{A}{2} \sin(\theta). \quad (3.24)$$

Therefore, the amplitude A and the phase difference from the reference signal at the f_r frequency can be obtained by

$$A = 2\sqrt{I^2 + Q^2} \quad (3.25)$$

$$\theta = \tan^{-1}(I/Q). \quad (3.26)$$

Figure 3.8 shows this mixing process in time and frequency domains by numerical computation as an instance. The amplitude and frequency of the original signal are $A = 10$ V and $f_s = 10$ kHz. The original signal contains Gaussian normal noise with the deviation of $\sigma = 2$ V (20 % of the amplitude). This signal is plotted in time domain (Figure 3.8a) and in frequency domain (Figure 3.8b). For the comparison, a signal containing less noise

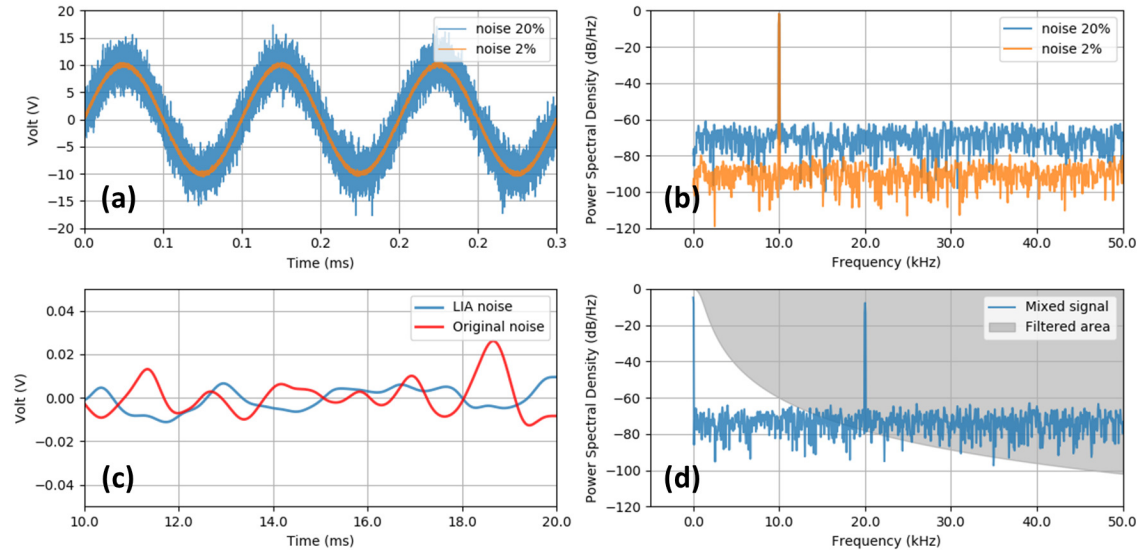


Figure 3.8 Mixing process and noise of the lock-in amplifier (LIA). (a) Signals contain different amount of noises. (b) Power spectrum density of (a). (c) The output noise after LIA, and the original noise filtered by the same filter. (d) Power spectrum density of the mixed signal.

($\sigma = 0.2$ V) is also displayed in same figures. The signal with $\sigma = 0.2$ V(RMS) noise has -20 dB lower power spectrum density than the original signal. The noise shapes a floor or exists in all frequencies. Therefore, this Gaussian normal noise is called as *white noise*. After multiplying the original signal by the reference signal $\cos(2\pi f_r t)$ with $f_r = f_s$, the protrusion at the frequency of f_s in Figure 3.8b is split into two frequencies, the DC (subtracted) and higher (added) frequency according to the equation (3.21). The gray area is filtered out by 3th-order Bessel filter with 1 kHz cut-off frequency. While the signal at 10 kHz will be attenuated by -60 dB, noises in the frequencies of less than 1 kHz still exists in the output signal. The final LIA output signal and the low-pass filtered original noise with the same Bessel filter are displayed in Figure 3.8d. The output signal has a offset of 5 V corresponding to the equation (3.23), but this offset is removed for comparing two noises. The root-mean squared (RMS) value of the filtered original noise is 8 mV(RMS), and the RMS of the LIA output signal is 5 mV(RMS) which is almost same as the filtered original noise.

Figure 3.9 is the experimental current-distance results in AC-mode SICM. The modu-

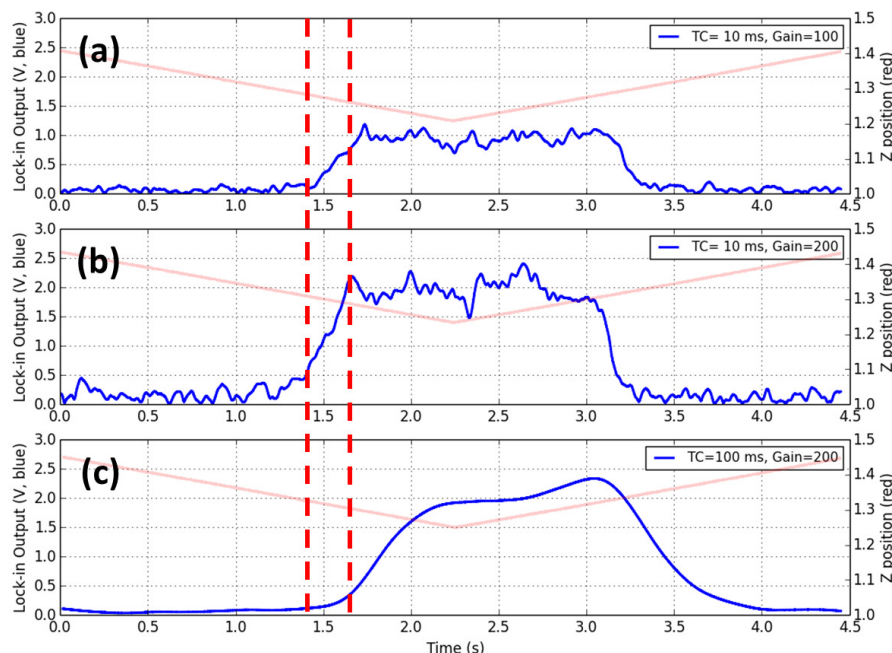


Figure 3.9 Experimental current-distance results in AC-mode SICM with various lock-in amplifier (LIA) settings. Blue lines are the LIA outputs with (a) the time constant $\tau = 10$ ms, gain = 100, (b) $\tau = 10$ ms, gain = 200, and (c) $\tau = 100$ ms, gain = 200. Red lines are Z positions of the pipette. Two red dashed vertical lines are the guide lines for indicating delay of the signal response from different time constants.

lation frequency and amplitude of the pipette are 633 Hz and 0.4 nm(RMS), respectively. The LIA output of ion-current and the Z position are colored in blue and red, respectively. Figure 3.9b is obtained from the same time constant (TC) $\tau = 10$ ms, but two times higher gain than the gain of Figure 3.9a. Therefore, the LIA output of Figure 3.9b is two times amplified than the output of Figure 3.9a, and the noise is also amplified as the same amount of signals. Figure 3.9c is obtained from the same gain as the gain of Figure 3.9b, but ten times higher time constant, i.e. more low-pass filtering. The LIA output in Figure 3.9c is a lot cleaner than others, but there is an apparent time delay, which indicates the signal becomes slower than others with less time constant.

The fundamental concept of LIA is mixing signals to shift the carrier or center frequency of signal band. In the case of AFM, the atomic force between the AFM tip and the sample surface can modulate the resonance frequency of the cantilever as describe in Subsection

3.1.3. Therefore, monitoring the amplitude and the phase changes at the resonance frequency provides important information in AFM, and LIA can shift the signals around the cantilever resonance frequency to lower frequency band which is much easier to handle by electronics.

However, for the case of SICM, there is no obvious relationship between modulated ion-current and the pipette-sample distance. The utilization of LIA in SICM would be a synonym for applying more filtering so that this slows down the system performance. According to the aforementioned reasons, DC-mode SICM was employed in this dissertation.

3.3 Finite Element Method (FEM)

The model of ion-current is not simply described as mentioned in Section 2.3. Modern researchers try to describe the ion-current behavior with Poisson-Nernst-Planck (PNP) equation^{18–21} which assumes continuous media in the form of partial differential equation (PDE). PDE can be solved by finite element method (FEM) numerically. This section formulates some basic equations to solve FEM, and a preliminary numerical solution of the ion-current model can be found in Section 8.4.

3.3.1 Variational Form

Most of FEM problems can be solved by Poisson equation. Poisson equation is

$$-\nabla^2 u(\mathbf{x}) = f(\mathbf{x}), \quad \mathbf{x} \text{ in } \Omega \quad (3.27)$$

$$u(\mathbf{x}) = u_D(\mathbf{x}), \quad \mathbf{x} \text{ on } \partial\Omega \quad (3.28)$$

where $u = u(\mathbf{x})$ is the unknown *trial* function and $f = f(\mathbf{x})$ is a prescribed function of \mathbf{x} . In this section, vectors are notated in normal bold symbols. Ω is the spatial domain, $\partial\Omega$ is the boundary of the domain. $u_D(\mathbf{x})$ is the known value of Dirichlet boundary condition.

FEM tries not to solve the *strong form* of the above equation directly, but to solve using an equivalent integral equation. This integral equation is known as a *weak form* or *variational form*. The integral performs over the domain with multiplying a *test* function

$$v = v(\mathbf{x}),$$

$$- \int_{\Omega} \nabla^2 u(\mathbf{x}) v(\mathbf{x}) \, dx = \int_{\Omega} f(\mathbf{x}) v(\mathbf{x}) \, dx. \quad (3.29)$$

The order of derivatives should be kept as low as possible in common. From the chain rule, $\nabla \cdot (v \nabla u) = \nabla v \cdot \nabla u + v \nabla^2 u$, the derivative of the equation (3.29) can be reduced, and becomes

$$\int_{\Omega} \nabla u \cdot \nabla v \, dx - \int_{\Omega} \nabla \cdot (v \nabla u) \, dx = \int_{\Omega} f(\mathbf{x}) v(\mathbf{x}) \, dx. \quad (3.30)$$

The second term of the left-hand side can be reduced by divergence theorem,

$$\int_{\Omega} \nabla \cdot (v \nabla u) \, dx = \int_{\partial\Omega} (\mathbf{n} \cdot \nabla u) v \, ds \quad (3.31)$$

with the normal outside vector \mathbf{n} on the boundary, and ds is the surface infinitesimal element. $g = -(\mathbf{n} \cdot \nabla u)$ is a known flux function as Neumann boundary condition.

Then, rearrangement of equations (3.30) and (3.31) becomes,

$$a(u, v) = \int_{\Omega} \nabla \cdot (v \nabla u) \, dx \quad (3.32)$$

$$L(v) = \int_{\Omega} f v \, dx - \int_{\Gamma_N} g v \, ds \quad (3.33)$$

$$a(u, v) = L(v) \quad (3.34)$$

with a *bilinear* form $a(u, v)$ and a *linear* form $L(v)$. Γ_N is the Neumann boundary. Since Dirichlet boundary conditions are not included in equations (3.32)–(3.34), Dirichlet boundary conditions are *essential* boundary conditions. Neumann boundary conditions are *natural* boundary conditions, because Neumann boundary conditions are appeared in the equation (3.33).

3.3.2 Numerical Solution of FEM

After discretization to solve equations (3.32)–(3.34) numerically, the variational form the equation (3.34) can be expressed in a matrix form,

$$\mathbf{A}\mathbf{u} = \mathbf{b}. \quad (3.35)$$

Then, the bilinear form $a(u, v)$ becomes $\mathbf{A}\mathbf{u}$, and the linear form $L(v)$ becomes \mathbf{b} after discretization or assembly of finite elements. \mathbf{u} is the discretized solution vector, which

should be found. If the inverse matrix of \mathbf{A} exists, then the solution can be easily calculated by

$$\mathbf{u} = \mathbf{A}^{-1}\mathbf{b} \quad (3.36)$$

However, many problems have no inverse matrix \mathbf{A}^{-1} . Hence, the problem is transformed to find an optimum solution of \mathbf{u}^* minimizing the sum of squared residuals (SSE),

$$h(\mathbf{u}) = \frac{1}{2}\|\mathbf{r}\|_2^2 = \frac{1}{2}\mathbf{r}^T\mathbf{r} = \frac{1}{2}\sum_i r_i^2 \quad (3.37)$$

where $\mathbf{r} = \mathbf{b} - \mathbf{A}\mathbf{u} = (r_1, r_2, \dots, r_n)^T$ is the residual vector with n elements. This optimization problem is known as *least square problem*. Using a matrix operation, the sum of squared residuals is approximated at the optimum point \mathbf{u}^* with some variation \mathbf{s} by

$$h(\mathbf{u}^* + \mathbf{s}) = h(\mathbf{u}^*) + (\nabla_{\mathbf{u}}h(\mathbf{u}^*))^T\mathbf{s} + \frac{1}{2}\nabla_{\mathbf{u}}^2h(\mathbf{u}^*)\mathbf{s}^T\mathbf{s} + \mathcal{O}(\mathbf{s}^3) \quad (3.38)$$

where $\nabla_{\mathbf{u}}$ is gradient with respect to \mathbf{u} , and \mathcal{O} is the big- \mathcal{O} notation. If \mathbf{u}^* is the minimum (or optimum) point of $f(\mathbf{u})$, the differentiation of $h(\mathbf{u})$ with respect to \mathbf{s} should be zero,

$$\frac{\partial h(\mathbf{u}^*)}{\partial \mathbf{s}} = \nabla_{\mathbf{u}}h(\mathbf{u}^*) + \nabla_{\mathbf{u}}^2h(\mathbf{u}^*)\mathbf{s} = \mathbf{0}. \quad (3.39)$$

Then, the *normal equation* (3.39) is expressed by

$$\mathbf{J}^T(\mathbf{u}^*)\mathbf{r}(\mathbf{u}^*) + \mathbf{H}(\mathbf{u}^*)\mathbf{s} = \mathbf{0}. \quad (3.40)$$

with Jacobian matrix \mathbf{J} , the gradient of h , and Hessian matrix \mathbf{H} ,

$$\mathbf{J} = \nabla_{\mathbf{u}}\mathbf{r}, \quad (3.41)$$

$$\nabla_{\mathbf{u}}h = \frac{1}{2}\nabla_{\mathbf{u}}(\mathbf{r}^T\mathbf{r}) = \mathbf{J}^T\mathbf{r}, \quad (3.42)$$

$$\mathbf{H}(\mathbf{u}) = \nabla_{\mathbf{u}}^2h(\mathbf{u}) = \sum_i \nabla_{\mathbf{u}}r_i(\nabla_{\mathbf{u}}r_i)^T + \sum_i r_i\nabla_{\mathbf{u}}^2r_i = \mathbf{J}^T\mathbf{J} + \sum_i r_i\nabla_{\mathbf{u}}^2r_i. \quad (3.43)$$

In the case of a linear problem, \mathbf{A} and \mathbf{b} are independent from the variable \mathbf{u} , then Jacobian is

$$\mathbf{J} = \nabla_{\mathbf{u}}\mathbf{r} = \nabla(\mathbf{b} - \mathbf{A}\mathbf{u}) = -\mathbf{A} \quad (3.44)$$

Table 3.1 Hessian Matrixes

Method	Hessian \mathbf{H}	Comment
Gauss-Newton	$\mathbf{J}^T \mathbf{J}$	
Newton	$\mathbf{J}^T \mathbf{J} + \sum_i r_i \nabla^2 r_i$	
Steepest Descent	$c \mathbf{I}$	c is constant.
Gradient Descent	$\text{diag}(\nabla^2 f)$	
Levenberg-Marquardt	$\mathbf{J}^T \mathbf{J} + \lambda \text{diag}(\mathbf{J}^T \mathbf{J})$	λ is selected by residual.

then, Hessian becomes zero $\mathbf{H} = \mathbf{0}$. The *normal equation* (3.40) in the linear problem becomes

$$\mathbf{J}^T \mathbf{r}(\mathbf{u}^*) + \mathbf{H}(\mathbf{u}^*) \mathbf{s} = -\mathbf{A}^T (\mathbf{b} - \mathbf{A} \mathbf{u}) = \mathbf{0}. \quad (3.45)$$

Finally, the solution can be obtained by

$$\mathbf{u} = (\mathbf{A}^T \mathbf{A})^{-1} \mathbf{A}^T \mathbf{b} = \mathbf{A}^\dagger \mathbf{b} \quad (3.46)$$

where $\mathbf{A}^\dagger = (\mathbf{A}^T \mathbf{A})^{-1} \mathbf{A}^T$ is the Moore-Penrose pseudo-inverse matrix.

For nonlinear problems, which $\mathbf{A} = \mathbf{A}(\mathbf{u})$ has a dependency on \mathbf{u} , the solution can be found by iteration method

$$\mathbf{u}^{(k+1)} = \mathbf{u}^{(k)} + \mathbf{s} \quad (3.47)$$

$$\mathbf{u}^* = \lim_{k \rightarrow \infty} \mathbf{u}^{(k)} \quad (3.48)$$

with the next step \mathbf{s} by solving the *normal equation* (3.40),

$$\mathbf{s} = -\mathbf{H}(\mathbf{u}^{(k)})^{-1} \mathbf{J}(\mathbf{u}^{(k)})^T \mathbf{r}(\mathbf{u}^{(k)}). \quad (3.49)$$

Since the calculation of the inverse of Hessian \mathbf{H}^{-1} is highly complex, there are many variations to approximate the inverse of Hessian matrix \mathbf{H}^{-1} . Most famous Hessian matrixes are summarized in Table 3.1.²² If the residual term is ignored in the equation (3.43), or Gauss-Newton method is used, then the iteration step \mathbf{s} can be calculated by

$$\mathbf{s} = (\mathbf{J}^{(k)})^{-1} (\mathbf{b}^{(k)} - \mathbf{A}^{(k)} \mathbf{u}^{(k)}). \quad (3.50)$$

This algebraic linearization also can be accomplished by PDE level directly. A specific linearization to solve nonlinear Poisson-Boltzmann equation is discussed in the next subsection.

3.3.3 Linearized Poisson-Boltzmann Equation

Poisson-Boltzmann (PB) equation is used for calculating the electrostatic potential from distributions of charged particles. PB equation of dimensionless form is

$$-\epsilon \nabla^2 \phi = \sum_i z_i c_i \quad (3.51)$$

with the concentration of the i -th charged particle

$$c_i = \exp(\bar{\mu}_i - z_i \phi) \quad (3.52)$$

where $\bar{\mu}_i$ is the electrochemical or total chemical potential, z_i is the charge valency. ϵ is dielectric constant of medium, ϕ is electrostatic potential. c_i is a function of ϕ exponentially, then this PB equation is not linear. Therefore, most PB equations have no analytical solution,²³ and should be solved numerically.

The exact electrostatic potential ϕ^* can be approximated around a certain solution $\phi^{(k)}$, then the electrostatic potential and the concentration become

$$\phi^* = \phi^{(k)} + s + \mathcal{O}(\delta^2) \quad (3.53)$$

$$c_i^* = c_i^{(k)} - z_i c_i^{(k)} s + \mathcal{O}(\delta^2). \quad (3.54)$$

By rearrangement of equations (3.51) – (3.54), a new linear equation as a function of s can be obtained,

$$-\epsilon \nabla^2 s + \sum_i z_i^2 c_i^{(k)} s = \sum_i z_i c_i^{(k)} + \epsilon \nabla^2 \phi^{(k)}. \quad (3.55)$$

After discretization of the equation (3.55), the linearized PB equation becomes the same form of the equation (3.50),

$$\mathbf{J}^{(k)} \mathbf{s} = \mathbf{b}^{(k)} - \mathbf{A}^{(k)} \mathbf{u}^{(k)} \quad (3.56)$$

which is derived from the algebraic level. Recalling the equation (3.35), the discretized $a(\phi, v)$ of $-\epsilon \nabla^2 \phi^{(k)}$ is $\mathbf{A}^{(k)} \mathbf{u}^{(k)}$, and the discretized $L(v)$ of $\sum_i z_i c_i^{(k)}$ is $\mathbf{b}^{(k)}$.

Gummel first suggested the linearized PB equation to solve a semiconductor problem in 1964.²⁴ s was calculated from the known solution $\phi^{(k)}$ instead of the exact solution ϕ^* ,

then the next $(k + 1)$ -th solution $\phi^{(k+1)}$ was induced by $\phi^{(k+1)} = \phi^{(k)} + s$. From these iterations, the solution can be converged to the exact solution ϕ^* ,

$$\phi^* = \lim_{k \rightarrow \infty} \phi^{(k)}. \quad (3.57)$$

References

- (1) Kasas, S.; Longo, G.; Dietler, G. Mechanical properties of biological specimens explored by atomic force microscopy. *J. Phys. D: Appl. Phys.* **2013**, *46*, 133001.
- (2) Binnig, G.; Rohrer, H. Scanning tunneling microscopy—from birth to adolescence. *Rev. Mod. Phys.* **1987**, *59*, 615.
- (3) Lekka, M.; Kulik, A. J. In *Applied Scanning Probe Methods II*, 2006, pp 205–239.
- (4) Cappella, B.; Dietler, G. Force-distance curves by atomic force microscopy. *Surf. Sci. Rep.* **1999**, *34*, 15–3104.
- (5) Sneddon, I. N. The relation between load and penetration in the axisymmetric Boussinesq problem for a punch of arbitrary profile. *Int. J. Eng. Sci.* **1965**, *3*, 47–57.
- (6) Clifford, C. A. Summary of ISO/TC 201 standard: ISO 11775: 2015–Surface chemical analysis–Scanning probe microscopy–Determination of cantilever normal spring constants. *Surf. Interface Anal.* **2017**, *49*, 171–172.
- (7) Hutter, J. L.; Bechhoefer, J. Calibration of atomic-force microscope tips. *Rev. Sci. Instrum.* **1993**, *64*, 1868–1868.
- (8) Voigtländer, B., Scanning probe microscopy. Springer: 2016.
- (9) Albrecht, T.; Grütter, P.; Horne, D.; Rugar, D. Frequency modulation detection using high-Q cantilevers for enhanced force microscope sensitivity. *J. Appl. Phys.* **1991**, *69*, 668–673.
- (10) Martin, Y.; Williams, C.; Wickramasinghe, H. K. Atomic force microscope–force mapping and profiling on a sub 100-Å scale. *J. Appl. Phys.* **1987**, *61*, 4723–4729.
- (11) Zhong, Q.; Inniss, D.; Kjoller, K.; Elings, V. Fractured polymer/silica fiber surface studied by tapping mode atomic force microscopy. *Surf. Sci. Lett.* **1993**, *290*, L688–L692.
- (12) García, R.; Perez, R. Dynamic atomic force microscopy methods. *Surf. Sci. Rep.* **2002**, *47*, 197–301.

- (13) García, R., Amplitude modulation atomic force microscopy. John Wiley & Sons: 2011.
- (14) Schäffer, T. E.; Anczykowski, B.; Fuchs, H. In *Applied Scanning Probe Methods II*, 2006, pp 91–119.
- (15) O’Connell, M. A.; Wain, A. J. Combined electrochemical-topographical imaging: a critical review. *Anal. Methods* **2015**, 7, 6983–6999.
- (16) Zhang, S.; Cho, S. J.; Busuttil, K.; Wang, C.; Besenbacher, F.; Dong, M. Scanning ion conductance microscopy studies of amyloid fibrils at nanoscale. *Nanoscale* **2012**, 4, 3105–3110.
- (17) Weber, A. E.; Baker, L. A. Experimental Studies of Resolution in Scanning Ion Conductance Microscopy. *J. Electrochem. Soc.* **2014**, 161, H924–H929.
- (18) Cervera, J.; Schiedt, B.; Ramírez, P. A Poisson/Nernst-Planck model for ionic transport through synthetic conical nanopores. *Europhys. Lett.* **2005**, 71, 35.
- (19) Cervera, J.; Schiedt, B.; Neumann, R.; Mafé, S.; Ramírez, P. Ionic conduction, rectification, and selectivity in single conical nanopores. *J. Chem. Phys.* **2006**, 124, 104706.
- (20) White, H. S.; Bund, A. Ion current rectification at nanopores in glass membranes. *Langmuir* **2008**, 24, 2212–2218.
- (21) Gamble, T.; Decker, K.; Plett, T. S.; Pevarnik, M.; Pietschmann, J.-F.; Vlassiouk, I.; Aksimentiev, A.; Siwy, Z. S. Rectification of ion current in nanopores depends on the type of monovalent cations: experiments and modeling. *J. Phys. Chem. C* **2014**, 118, 9809–9819.
- (22) Wright, S. J.; Nocedal, J. Numerical optimization. *Springer Science* **1999**, 35, 7.
- (23) Kirby, B. J., Micro-and nanoscale fluid mechanics: transport in microfluidic devices. Cambridge University Press: 2010.
- (24) Gummel, H. K. A self-consistent iterative scheme for one-dimensional steady state transistor calculations. *IEEE Trans. Electron Devices* **1964**, 11, 455–465.

Chapter 4*

Structural Analysis by AFM and SEM

Atomic force microscopy (AFM) has been employed to examine the morphology of mouse spermatozoa with submicron resolution. Contact mode AFM imaging was performed to obtain optimized topographic images of the natural surface structures of untreated mouse spermatozoa. Simple spermatozoa preparation protocol is employed to investigate the sperm in 3D with scanning electron microscopy (SEM). In normal air condition, AFM images of the surface structures of fixed mouse sperm clearly visualize all the anatomical features of sub-cellular surface structures on fixed, rapidly prepared, intact mouse spermatozoa. Unlike with AFM images, the focused electron beam of SEM for zooming-in caused damages on spermatozoa surface. The ultrastructural investigation also identified a new possible structure, named end knob in end piece region which could have a role in propulsion. Consequently, the convenient AFM imaging with minimized sample preparation proved its values for studying structural abnormalities of sperms. Morphological alterations and their effects on infertility could be understood by identifying structural abnormalities of spermatozoa.

*This chapter is prepared to submit under the title of “Ultra-structural AFM investigation of mouse sperm gives new insight in sperm fertilization.”

4.1 Introduction

The mammalian spermatozoon, or sperm has a complex structure; it consisted of three parts, head, middle piece and tail. The middle piece stores energy in mitochondria and provides the energy for the tail to move. The sperm head contains acrosome and nucleus, which contains a half set of chromosomes.¹ Spermatozoa are initially non-motile as they enter the caput epididymis from seminiferous tubules. Spermatozoa move slowly to cauda epididymis and undergo maturation for about 2 to 3 months and acquire the ability to swim forward and to fertilize an egg. The spermatozoa from the caput and the cauda are employed in this study.¹

The evaluation of sperm morphology is important in breeding soundness exam in any species. The size and shape of the head, midpiece, and tail are examined in most cases. The abnormal sperms are always found, but when the percentage of abnormal sperms becomes excessive, fertility decreases.² The anatomic side of the defect is mainly inspected by optical microscopy. An eosin-nigrosin staining, so-called live-dead staining or toluidine blue staining is mainly used in microscopy inspection.³ In addition, differential interference contrast (DIC) microscopy without staining is also used to inspect sperms after glutaraldehyde fixation.⁴ However, all of these visualization techniques are inadequate for detailed inspection because of poor resolution. Scanning electron microscopy (SEM) has been suggested as an alternative, but the complex, time-consuming, and harsh sample preparation prevent its usage in everyday practice. On the other hand, scanning probe microscopy (SPM) techniques demonstrated its potential to probe the physical and chemical properties of nanoscale materials since its invention in 1981.⁵⁻⁸ Among SPMs, atomic force microscopy (AFM) and scanning ion-conductance microscopy (SICM) are uniquely capable of imaging biological samples under physiological conditions. Even though operating AFM in liquid is not suitable for routine sperm inspection and the resolution of measurement in liquid is not as high as the resolution of measurement performed in air,⁹ AFM has been optimized for over 30 years in measurement in the ambient condition enough to perform routine sperm inspection.¹⁰ The convenient AFM imaging with minimized sample preparation of sperm, high-resolution and 3D construction can provide invaluable analysis not only in research

but the infertility test in the hospital. The ultrastructural investigation of spermatozoa by AFM identifies the possible new structure which could have an important role in increasing propulsion efficiency of sperm. The quick protocol to prepare sperm samples for AFM inspection is also introduced in ‘Materials and Methods’ section.

4.2 Materials and Methods

4.2.1 Atomic Force Microscopy (AFM)

All images were obtained using a commercial XE-100 AFM (Park Systems, Korea) under ambient conditions. AFM system has an XY flat scanner $50\text{ }\mu\text{m} \times 50\text{ }\mu\text{m}$ and a separate AFM head with $14\text{ }\mu\text{m}$ Z scanner. Before AFM imaging, air dried samples on a glass slide were surveyed using 10X objective equipped on XE-100 (M Plan Apo 10X, Mitutoyo, Japan). Once the target is determined, then the AFM cantilever approaches and scans to generate 3D topography of the sperm. The whole process took about 15 minutes to generate one AFM image. Silicon nitride cantilevers (DNP-S, Bruker, USA) with a typical resonance frequency of 56 kHz, a spring constant of 0.24 N m^{-1} , and a typical tip radius of 10 nm were used to image sperms in ambient conditions. AFM imaging was performed in contact mode at a scan frequency of 0.3 Hz to 1 Hz with an applied minimal loading force of 100 pN and optimized feedback parameters. The images presented in this chapter are contact mode images. The resolution of all original AFM images was 256×256 pixels per image. The images were flattened and analyzed by using the XEI software program (Park Systems, Korea). The images presented in this chapter are topographical (Figure 4.1c, and Figure 4.3) and deflection (Figure 4.1b,d, Figure 4.2, and Figure 4.4) images. The deflection images were generated at the same time with topographical images by error signal of the AFM cantilever. The bigger AFM images than $50\text{ }\mu\text{m}$, shown in Figure 4.1b-d, and Figure 4.2, were made by manually stitching deflection images and topographical images using Adobe Photoshop (Adobe Systems, USA).

4.2.2 Scanning Electron Microscopy (SEM)

After AFM imaging, some of the specimens were prepared for SEM imaging. Samples for SEM imaging were already air dried for AFM imaging. This was followed by mounting

on aluminum stubs, coating with platinum-palladium in an ion coater, and observation in a field emission SEM (S-4300SE/N, Hitachi High-Technologies, Japan) using an acceleration potential of 15 kV at different magnifications.

4.2.3 Preparation of Epididymis Spermatozoa

Completely reproductive postnatal 8 weeks ICR (institute of cancer research) male mice were euthanized by CO₂ asphyxiation, and the epididymis was removed at room temperature. Cauda epididymis was submerged in modified sperm washing medium (Irvine Scientific, USA) and the spermatozoa were collected by gentle squeezing out the epididymis with forceps. The spermatozoa from caput epididymis were also collected by the same procedure for comparison. The collected spermatozoa were transferred to a conical tube, incubated at 37 °C for 15 minutes, and then the active spermatozoa located in the top fraction in the tube were again collected. The epididymal fluid was removed from spermatozoa by centrifugation at 550 g for 10 minutes. The spermatozoa were fixed with 1 % paraformaldehyde and 1 % glutaraldehyde mixture, and deposited on a glass slide for air drying. Dried samples were carefully washed out with distilled water several times to remove residual salt and dirt for better imaging. All animal experiments were performed in accordance with the guide for care and use of laboratory animals at Hanyang University and Nanyang Technological University.

4.3 Results

AFM images show detailed 3D structures of mouse spermatozoa with high-resolution, which is only achievable with SEM before. AFM can image samples right after placing spermatozoa on a glass slide and air drying, compared with complex sample preparation involving fixation, drying, metal coating and imaging in vacuum condition of SEM. Topographical and deflection images can be obtained simultaneously, and those can be compared and overlaid on the optical images as shown in Figure 4.1.

The 3D topography images of AFM are presented as a map of differently colored pixels, with a color bar relating the color to a height on the left side of the images. The color bar

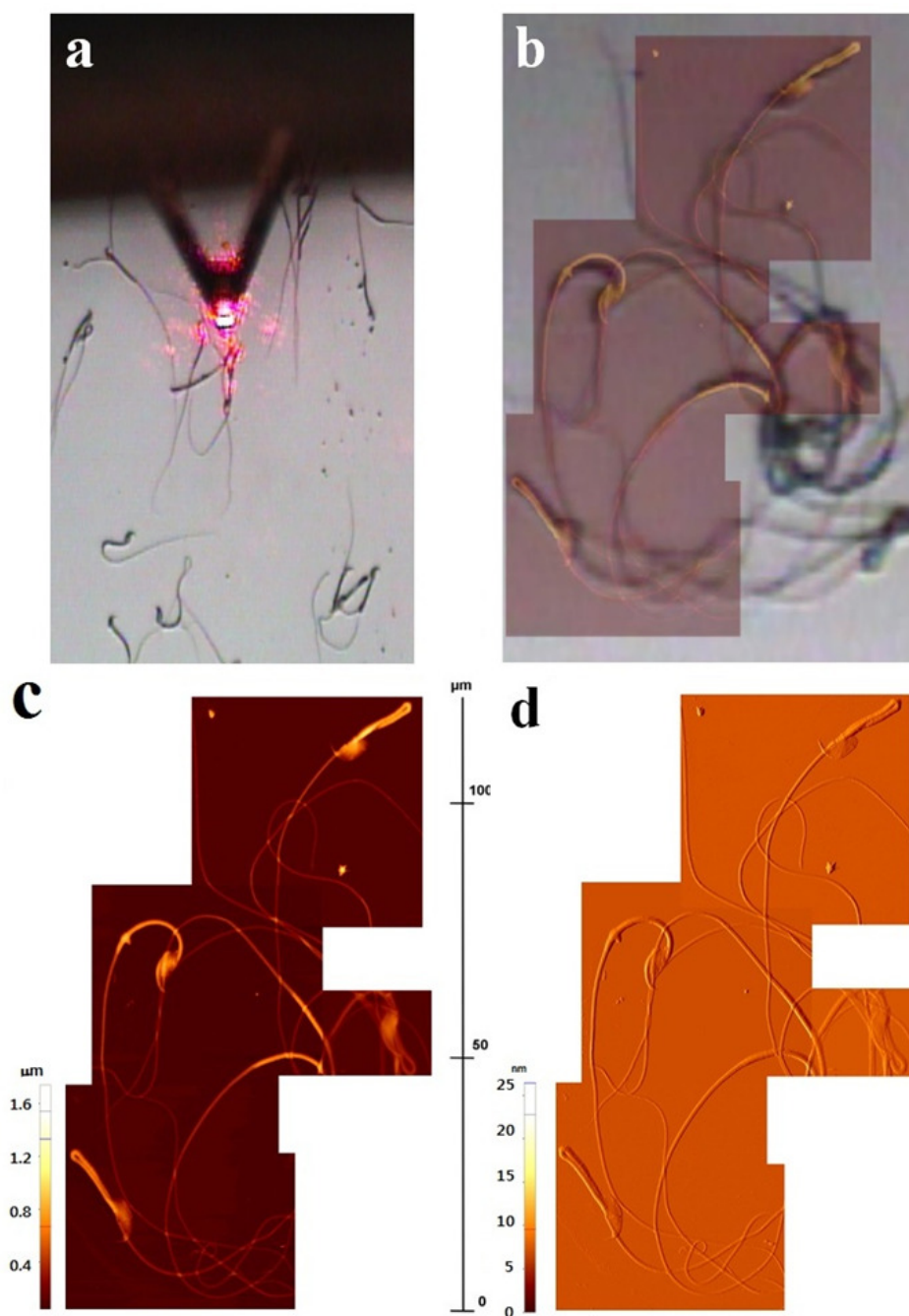


Figure 4.1 Optical view and AFM images of a mouse spermatozoon. (a) Optical view indicates that the AFM cantilever is approaching the air-dried mouse spermatozoa sample. (b) Four deflection (error signal) high-resolution images of AFM were stitched and overlaid on the low resolution optical view produced by a 10X objective. (c) Stitched 3D topographical AFM images. (d) Stitched deflection AFM images.

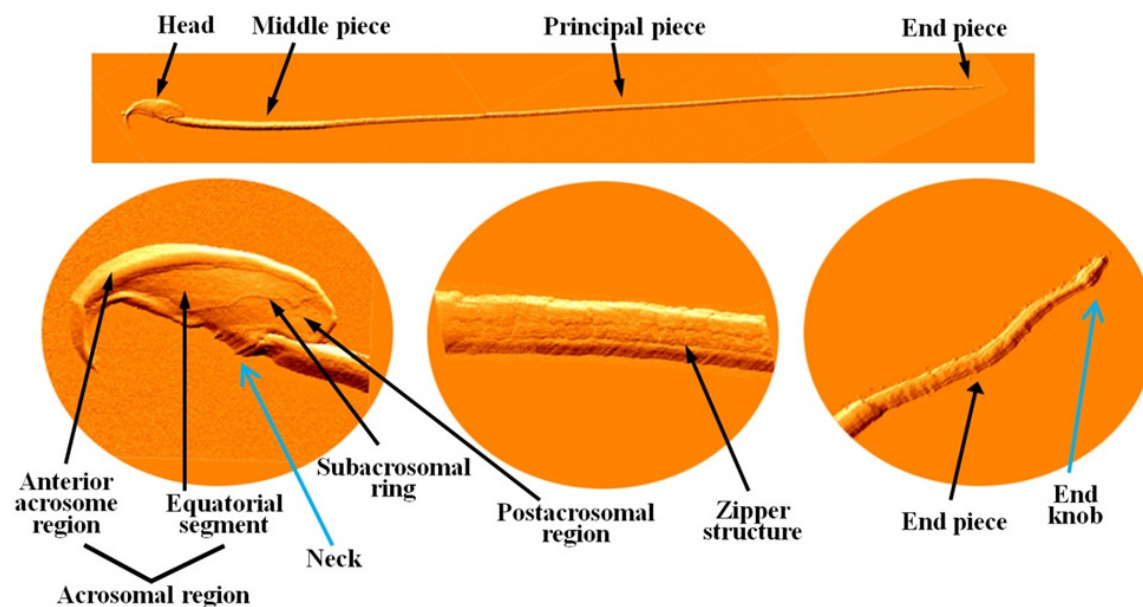


Figure 4.2 The stitched high-resolution AFM image in deflection mode of a mouse spermatozoon.. The major domains on the sperm head are the acrosomal region and the postacrosomal region. They are separated from each other by the subacrosomal ring. The acrosomal region can be further subdivided into the anterior acrosome region (acrosomal cap) and the equatorial segment. The sperm head is connecting to the middle piece via neck structure (sky blue arrow). The plasma membrane of the sperm tail consists of the middle piece, the principal piece, and the end piece. On the principal piece, zipper structure is visible in the AFM image, and the end piece shows unidentified structure we named *end knob* (sky blue arrow.)

of the topographical image indicates that the height of the spermatozoa imaged with AFM is approximately $1\ \mu\text{m}$ (Figure 4.1c). Figure 4.1d represents deflection images which are equivalent to a map of the slope of the sample. AFM makes images as the tip deflects when it encounters sample topography which is also called error signal of AFM. Hence this deflection image enhances the height variation of samples. Even though the z-scale in deflection is meaningless in terms of the sample structure, a deflection image usually displays the shape of the sample more easily.

The detailed anatomical structure can be distinguished in the stitched AFM images of a mouse spermatozoon as shown in Figure 4.2. The acrosomal region with anterior acrosome, equatorial segment, and the postacrosomal region separated by a subacrosomal ring

of the sperm head are clearly visible. The connecting neck structure with sky blue arrow between head and midpiece looks like an accordion in AFM images which is usually not clear and easy to be overlooked in SEM picture. Zipper structure appears as a double row of intramembranous particles running longitudinally within the plasma membrane of the principal piece which is usually observed in freeze-fracture SEM.¹¹ The zoomed in picture of the end piece shows the unidentified structure and named *end knob* from hence.

The deflection mode shows detailed anatomical structures because the movement of cantilever is sensitive to the structural changes, but it cannot be used in the dimensional measurement. On the other hand, the subtle and detailed structural changes are quite difficult to be identified because it became obscured by bigger structures, but topographical images contain 3D information and provide a dimensional value at the location of interest. Figure 4.3a profile indicates that the height of the dried spermatozoon head is about 500 nm which is about 400 nm lower than the head of the hydrated condition (data not shown). Figure 4.3b shows the principal piece with zipper structure with approximately 160 nm height and 700 nm width. Figure 4.3c shows the area where the principal piece connects to the end piece. It is easily distinguished between principal and end piece by its size difference. The profiles of Figure 4.3 show that the tail tapered to the end. The high-resolution picture of Figure 4.3d displays cone shaped *end knob* at the end of the tail.

In order to be sure of the existence of the end knob structure, spermatozoa separated from caput and cauda were examined with AFM and SEM. Not all of spermatozoa demonstrate end knob structure as found in Figure 4.4. Also, the electron beam of SEM is quite destructive compared to the AFM imaging technique. Arrows in SEM images indicate the damages caused by the electron beam of SEM. The end knob structure has not been reported before because it could be quite fragile compared to the other structures and it is easily damaged by electron beam or even with force exerted by AFM tip. However, the results in this chapter demonstrate that AFM is less destructive than SEM on imaging fragile biological samples.

Further to verify whether the end knob is a physiologically meaningful structure or it

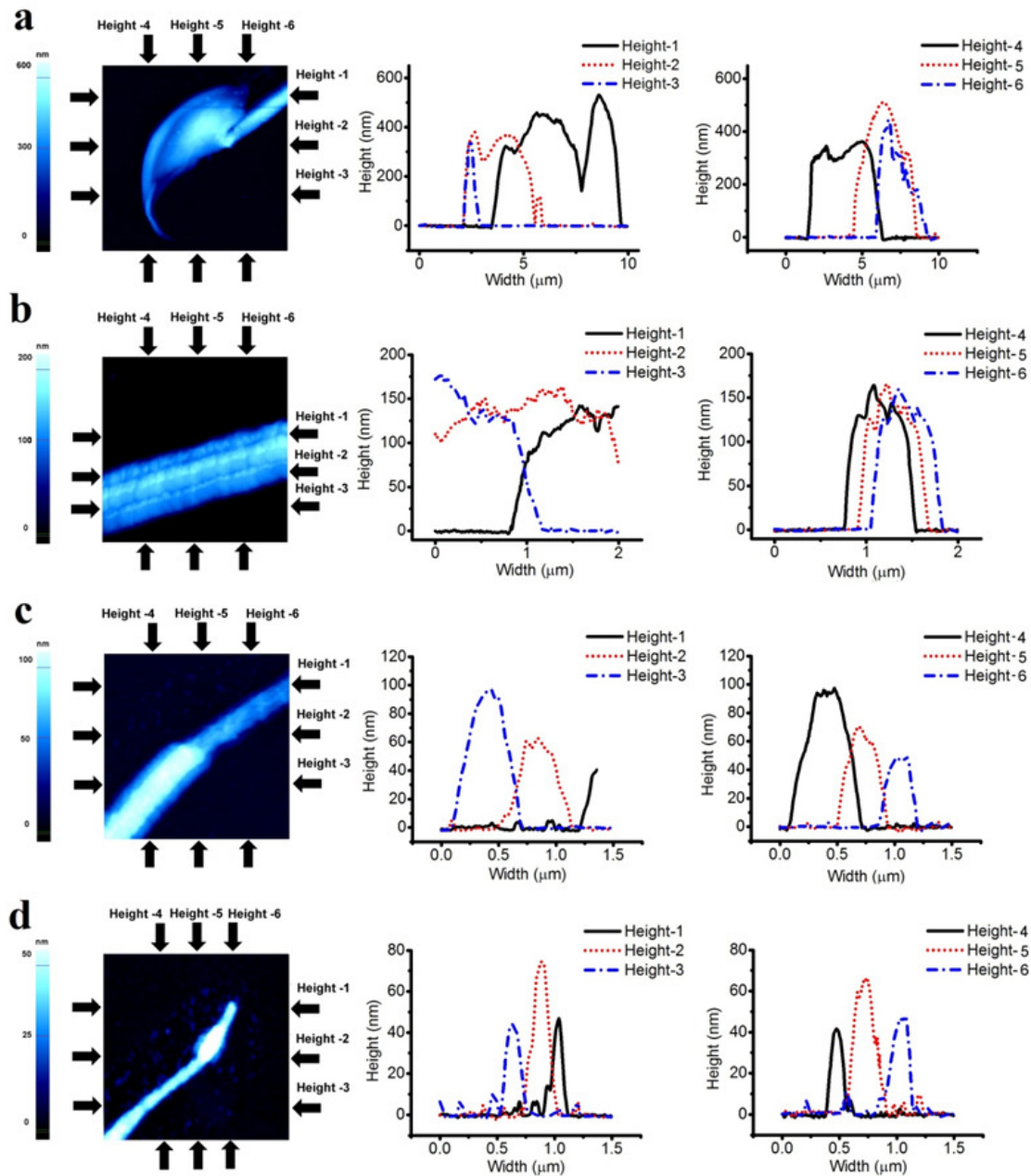


Figure 4.3 The topographical image of AFM gives profiles of detailed sperm structures.

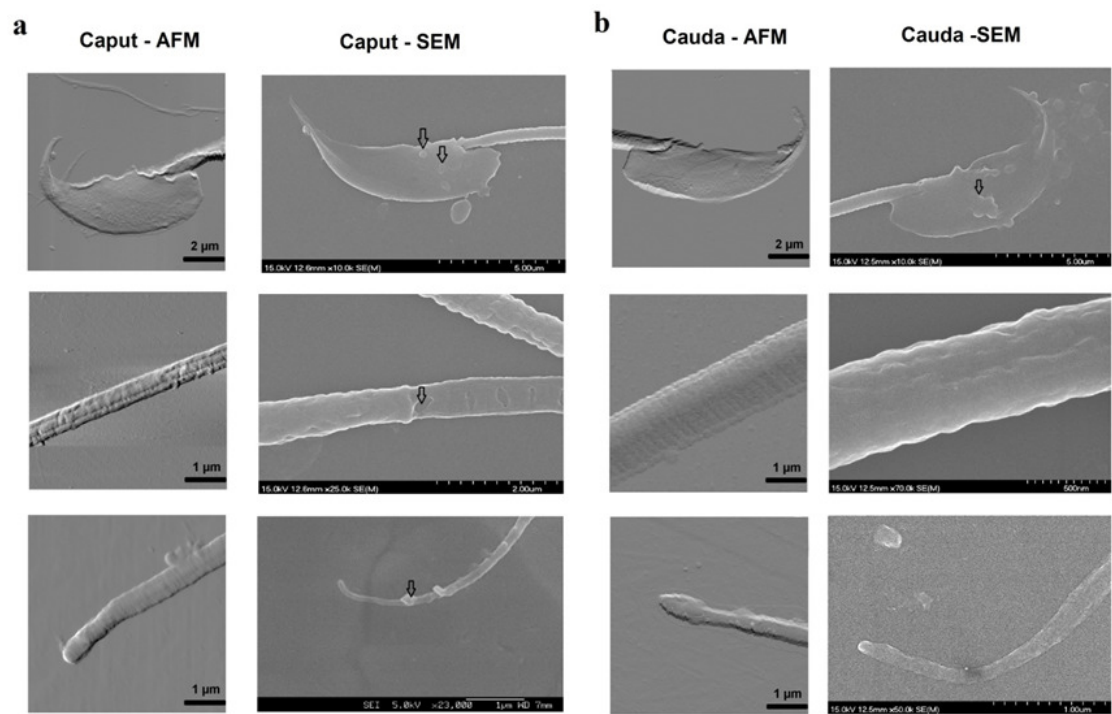


Figure 4.4 Spermatozoa from caput and cauda were examined by AFM and SEM. The arrows indicate damages caused by the electron beam of the SEM.

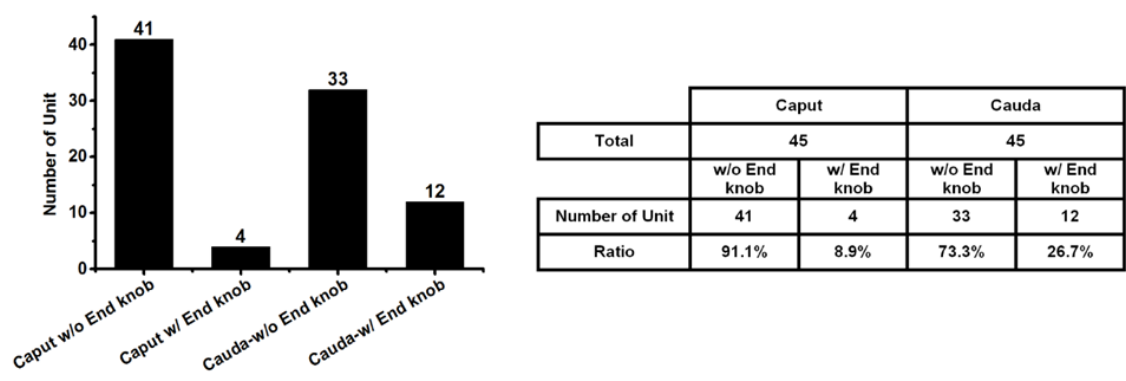


Figure 4.5 End knob structure statistics among 45 mouse spermatozoa. Spermatozoa from cauda have more end knob structure compared with caput.

happens due to the sample preparation or AFM imaging artifact, 45 mouse spermatozoa from caput and cauda were inspected in Figure 4.5 after discarding abnormal shaped or severe damaged spermatozoa. Among 45 spermatozoa from caput, only 4 spermatozoa show end knob like structure, and it was not clearly observed in the other 41 spermatozoa. However, among spermatozoa from cauda, 12 out of 45 spermatozoa were appeared to have end knob structure. Spermatozoa from cauda have 17.8 % more end knob structure than the one from caput.

4.4 Discussion

The male partners of four couples among ten infertile couples are the sole or a contributing cause of infertility.¹² In order to determine if a man is infertile, doctors conduct a semen analysis, which is also called a sperm test. A semen analysis measures three major factors of sperm health: number of sperm, the shape of sperm and mobility of sperm.² The sperm morphology may be correlated with a man's fertility potential,² but it has not been demonstrated the direct correlation between the morphology and the ability to conceive in natural condition. However, it is easily surmised that the importance of the sperm morphology in male fertility from the fact that the percentage of abnormal sperm is higher in the male infertility cases.¹³ Currently, one of the best visualization methods is the high magnification sperm inspection technique used for intracytoplasmic morphologically selected sperm injection for *in vitro* fertilization which is using high magnification differential interference contrast (DIC) microscopy with oil emergent 100X objective described by Bartoov et al.¹⁴ However, the method has still low resolution to fully inspect spermatozoa. This optical method only provides head size, head shape, the mid-piece number of vacuoles as well as the ratio between head size and size of the vacuoles. Detailed inspection of the anatomy of spermatozoa is severely limited with the optical method. SEM may provide high-resolution information, but the complex sample preparation hinders its use for daily inspection even without the fact that the electron beam for high-resolution imaging easily damages the fragile biological structure. Figure 4.1 demonstrates that AFM could be a simple solution for high-resolution sperm morphological test. After the isolation of spermatozoa, the sample can be smeared on a slide glass, washed and dried in 10 minutes for AFM imaging. Al-

though sample preparation for mouse spermatozoa AFM inspection has been optimized in this work, sample preparation for human spermatozoa, which may not be different much, should be optimized for the medical infertility test.

The high-resolution AFM inspection identifies detailed anatomical structures of mouse spermatozoa as seen in Figure 4.2. The AFM investigation of spermatozoa not only confirmed previously identified structures by scanning electron microscopy, but also lead to the anatomical structures which have never been investigated or explained before. The AFM image shows the detailed structure of connecting neck between head and midpiece. The accordion shaped structure may ensure the flexible movement of the head. Since the head shape of the mouse sperm is quite different from human sperm, this particular structure may not be similar. The unidentified structure at the end of the tail was found and named as *end knob* since it resembles the structure at the grip of the baseball bat or door knob. Unlike any other optical microscopy and SEM, the AFM topography image provides 3D profiles with dimensional values. The end knob structure demonstrated approximately twice the height (about 80 nm) compared to the end piece (about 40 nm).

The end knob could be the evolutionary structure which could help spermatozoa to propel toward an egg. If the end knob structure is for propulsion, it could form in the last stage of maturation. Since it is commonly believed that spermatozoa acquire their maturity while passing the epididymis,¹⁵ the spermatozoa from cauda epididymis should have a distinct end knob structure compared to the one from caput epididymis. The result from AFM and SEM examination of epididymal spermatozoa shows the existence of the end knob structure but not in all of spermatozoa as shown in Figure 4.4. The end knob structure was identified in only a quarter of spermatozoa in AFM images and even much less in SEM images. The end knob structure was quite small with only few hundred nm so it could be easily damaged by the electron beam of SEM and a probe of AFM. AFM was better in imaging such delicate structures but it also easily damages the structures when the force applied by the probe was not carefully controlled. Therefore, it was not easy to determine exact proportion of spermatozoa with an end knob structure. Since there is no better way to visualize the end knob structure, AFM was utilized to count the spermatozoa with the end

knob structure from caput and cauda epididymis separately as displayed in Figure 4.5. More end knob structures from the spermatozoa of cauda epididymis were found than the one of caput epididymis. The result may suggest the possibility that the spermatozoon acquires an end knob structure at the end of maturation. However, the sample preparation and AFM imaging need to be more optimized, and more samples should be investigated to be certain, because one paper reported there is no significant difference in live sperm in different parts of epididymis in respect of containing protoplasmic droplets.¹⁶

References

- (1) Carlson, B. M., Human Embryology and Developmental Biology. Elsevier Health Sciences: 2012.
- (2) Guzick, D. S.; Overstreet, J. W.; Factor-Litvak, P.; Brazil, C. K.; Nakajima, S. T.; Coutifaris, C.; Carson, S. A.; Cisneros, P.; Steinkampf, M. P.; Hill, J. A. Sperm morphology, motility, and concentration in fertile and infertile men. *N. Engl. J. Med.* **2001**, *345*, 1388–1393.
- (3) Salisbury, G.; Van Dongen, C. A comparison of several methods of estimating nuclear size of bovine spermatozoa. *J. Anim. Sci.* **1964**, *23*, 1098–1101.
- (4) Cross, N. L.; Meizel, S. Methods for evaluating the acrosomal status of mammalian sperm. *Biol. Reprod.* **1989**, *41*, 635–641.
- (5) Binnig, G.; Rohrer, H.; Gerber, C.; Weibel, E. Surface studies by scanning tunneling microscopy. *Phys. Rev. Lett.* **1982**, *49*, 57.
- (6) Binnig, G.; Rohrer, H.; Gerber, C.; Weibel, E. Tunneling through a controllable vacuum gap. *Appl. Phys. Lett.* **1982**, *40*, 178–180.
- (7) Binnig, G.; Rohrer, H.; Gerber, C.; Weibel, E. Vacuum tunneling. *Physica B+ C* **1982**, *109*, 2075–2077.
- (8) Binnig, G.; Rohrer, H.; Gerber, C.; Weibel, E. 7×7 reconstruction on Si (111) resolved in real space. *Phys. Rev. Lett.* **1983**, *50*, 120.
- (9) Usukura, J.; Yoshimura, A.; Minakata, S.; Youn, D.; Ahn, J.; Cho, S.-J. Use of the unroofing technique for atomic force microscopic imaging of the intra-cellular

- cytoskeleton under aqueous conditions. *J. Electron Microsc. (Tokyo)* **2012**, *61*, 321–326.
- (10) Lee, D.-Y.; Kim, D.-M.; Gweon, D.-G.; Park, J. A calibrated atomic force microscope using an orthogonal scanner and a calibrated laser interferometer. *Appl. Surf. Sci.* **2007**, *253*, 3945–3951.
- (11) Dallai, R.; Beani, L.; Kathirithamby, J.; Lupetti, P.; Afzelius, B. New findings on sperm ultrastructure of *Xenos vesparum* (Rossi)(Strepsiptera, Insecta). *Tissue Cell* **2003**, *35*, 19–27.
- (12) Brugh, V. M.; Lipshultz, L. I. Male factor infertility: evaluation and management. *Med. Clin. North Am.* **2004**, *88*, 367–385.
- (13) Chemes, H. E.; Rawe, V. Y. Sperm pathology: a step beyond descriptive morphology. Origin, characterization and fertility potential of abnormal sperm phenotypes in infertile men. *Hum. Reprod. Update* **2003**, *9*, 405–428.
- (14) Bartoov, B.; Berkovitz, A.; Eltes, F.; Kogosowski, A.; Menezo, Y.; Barak, Y. Real-Time Fine Morphology of Motile Human Sperm Cells is Associated With IVF-ICSI Outcome. *J. Androl.* **2002**, *23*, 1–8.
- (15) Cooper, T. G. The epididymis, cytoplasmic droplets and male fertility. *Asian J. Androl.* **2011**, *13*, 130–138.
- (16) Tajik, P.; Arman, A.; Taktaz, T. Bovine epididymal sperm morphology obtained from caput, corpus and cauda epididymides. *Pak. J. Biol. Sci.* **2007**, *10*, 3936–9.

Chapter 5*

Dimensional Comparison between AFM and SICM

The growing range of scanning probe microscopy (SPM) applications for atomic force microscopy (AFM) in biological sciences indicates the demand for tools in understanding the fundamental physics of biological systems. However, the complexity associated with applying SPM techniques for biomedical research overshadows its usefulness. In recent times, the development of scanning ion conductance microscopy (SICM) has overcome these limitations and enabled contact-free, high-resolution imaging of live biological specimens. This work demonstrates the limitation of AFM imaging of biological samples in liquid caused by AFM tip-sample interaction artifact, and how SICM imaging could overcome those limitations with contact-free scanning. Compared to AFM, a better fit of the SICM measurement with the actual dimension of the biological samples is demonstrated. The results indicate that the superior SICM imaging capability enables SICM to become widely adopted as a general and versatile research tool for biological studies in nanoscale.

*This chapter published substantially as Kim, J.; Choi, M.; Jung, G.-E.; Ferhan, A. R.; Cho, N.-J.; Cho, S.-J. Dimensional comparison between amplitudemodulation atomic force microscopy and scanning ion conductance microscopy of biological samples. *Jpn. J. of Appl. Phys.* **2016**, 55, 08NB18.

5.1 Introduction

Among various scanning probe microscopy (SPM) techniques, atomic force microscopy (AFM) has been widely utilized for biological studies since its invention because of its feasibility to be operated in vacuum, air and even liquid.^{1,2} However, the sharp tips used in AFM easily interacts with the adhesive and soft nature of the biological surface, often causing it to drag and damage soft biological tissues.^{3,4}

To overcome these technical difficulties, a particular variation of SPM known as scanning ion conductance microscopy (SICM) was employed. SICM was first developed by Hansma et al. in 1989⁵ and widely tested its biological applications in Korchev's group.⁶⁻⁹ The measurement principle of SICM is based on monitoring changes in ion conductance via a glass nanopipette between two electrodes.¹⁰⁻¹² The pipette functions as an AFM tip where the monitored ion current signal is modulated by the gap between the sample surface and the tip apex for feedback control of the pipette-sample distance.¹³ The SICM device positions a scanning nanopipette^{7,8} at a certain distance above the sample (i.e., typically within the tip diameter range)¹⁴ and follows topographical changes of the sample without making any physical contact.

Over the years, sensitivity and stability of SICM have been improved with the development of various vertical approach methods such as hopping,¹⁵ backstep,^{16,17} standing approach,¹⁸ and approach-retract-scanning (ARS) methods.^{13,19} The advantage of the vertical approach lies in its ability to decouple lateral and vertical motions of the pipette, thereby minimizing potential tip-sample interactions and leading to more accurate dimensional measurements. This study compares the dimensional measurements of AFM and SICM images to describe AFM artifacts and advantages of SICM imaging technique.

5.2 Materials and Methods

5.2.1 Atomic Force Microscopy (AFM)

AFM images were obtained with a commercial SPM (XE-Bio System, Park Systems, Korea). This system has an SPM system on the stage of an inverted optical microscope

(TE2000, Nikon, Japan). The SPM system has an $100\text{ }\mu\text{m} \times 100\text{ }\mu\text{m}$ XY scanner and an AFM or SICM head with a $25\text{ }\mu\text{m}$ Z scanner.

All AFM images in this chapter were obtained with amplitude modulation AFM mode both in the air and the liquid environments. For a direct comparison between AFM and SICM, AFM images were taken by raster scanning and ARS method. The raster scanning method has been typically used in AFM measurement which drags the tip maintaining the tip-sample distance in a given value. The corresponding ARS method in AFM is known as hopping mode,^{20,21} force mapping mode,²² and pulsed force mode.²³ The force mapping method is usually operated in contact mode AFM, but all AFM results reported in this work are from the amplitude modulation technique in order to keep the loading forces as low as possible.

The cantilevers used were Biolever-mini (rectangular cantilever with typical spring constant of 0.1 N m^{-1} and resonance frequency of about 110 kHz , Olympus, Japan) for collagen fibrils and PNP-TR (triangle cantilever with typical spring constant of 0.32 N m^{-1} and resonance frequency of about 67 kHz , NanoWorld, Switzerland) for fibroblast cells. The free oscillation amplitude and setpoint of air dried collagen fibrils were 21 nm and 7 nm , respectively. Those parameters of the collagen immersed in saline were 16 nm and 10 nm for raster scanning and 12 nm and 4 nm for ARS with 28 kHz operating frequency, respectively. The fibroblast cell image was taken with 37 nm free oscillation frequency, 2 nm setpoint and 20 kHz operating frequency.

5.2.2 Scanning Ion-Conductance Microscopy (SICM)

SICM images were obtained with the same SPM platform after the head was exchanged for SICM imaging. SICM Probe, nanopipettes were pulled from borosilicate capillaries of 1.0 mm outside diameter, 0.58 mm inside diameter (Warner Instruments, CT) using a P-2000 CO_2 laser puller (Sutter Instrument, CA). Fabricated nanopipette tips have an inner diameter of 100 nm typically with laser puller pulling parameters: HEAT 265, FIL 4, VEL 30, DEL 225, PUL 150. One Ag/AgCl electrode located in bulk bath solution serves as the reference electrode for all applied potentials. A separate Ag/AgCl electrode was placed

inside the nanopipette tip and biased in order to generate ion current through the tip. For the feedback signal, the ion current was amplified with an analog current-to-voltage converter.

Prior to measurement and imaging, the bias potential at the nanopipette was set to -150 mV, which roughly corresponded to 0.8 nA current. In the present study, images were primarily obtained in the ARS method with 99 % setpoint.

5.2.3 Edge-enhanced coloring

All images in this chapter are displayed twice with two different color schemes; gray-scaled and edge-enhanced. Gray-scaled images from four different imaging conditions have the same color scale to compare the height differences among the conditions. Edge-enhanced images show more stereoscopic features than gray-scaled images. In the edge-enhanced image, the topographical information is reflected in red channel. The gradient of the topography is colored in blue channel reversely so that smoother surfaces are appeared as bluer, and edges as darker. The gradient is obtained by Sobel filter. The green channel reflects both of topography and gradient evenly.

5.2.4 Buffer Solution

Deionized water (resistivity: 18.2 M Ω cm at 25 °C) was obtained from a Milli-Q water (Millipore, MA) and used to prepare all buffer solutions. Phosphate buffered saline (PBS; 10 mM phosphate buffer, 137 mM sodium chloride, and 2.7 mM potassium chloride) was used as the standard electrolyte solution for the SICM measurements. The nanopipette tip and petri dish used in experiments were also filled with PBS solution.

5.2.5 Collagen Fibrils

Collagen fibrils were obtained from the tail tendon of Wistar rats and stored in physiological saline with 1 % to 10 % tymol (2-isopropyl-5-methylphenol) at 4 °C for a minimum of one day. A small piece of the tendon was then stretched on the surface and air dried overnight, followed by immersion of the sample in physiological saline (NaCl) or phosphate buffer saline (PBS) before AFM and SICM imaging.

5.2.6 Fibroblast Cells

COS-7 cells were cultured in a petri dish (20035, SPL Lifescience, Korea) for 24 hours before the experiment in order to promote cell adhesion. It was fixed with 4 % formaldehyde for 2 hours prior experiment and observed by AFM and SICM.

5.3 Results and Discussion

5.3.1 Imaging Collagen Fibrils

The capabilities of AFM and SICM to image collagen fibrils were compared in Figure 5.1. The air-dried collagen fibrils were prepared and imaged first using amplitude-modulation AFM with raster scanning (i.e., scanning in line-by-line with the AFM tip moving back and forth). It showed the supertwisted structure having dimensions of 140 nm in height and 370 nm in width. The width was taken at 50 nm height from the baseline.

When the collagen fibril was immersed in saline, it billowed; the height and width increased to 200 nm and 530 nm, respectively. The use of raster scanning indicated the inclusion of tip artifact. When the ARS method was employed to minimize lateral artifacts, the width decreased by 100 nm to 430 nm. Even so, the height-to-width ratio still remained at about 1:2, indicating the persistent presence of tip artifacts.

On the other hand, by using SICM with ARS, the dimensions were 340 nm and 410 nm in height and width, respectively. It is a good indicator that the height-to-width ratio is close to 1:1 because collagen fibrils are supertwisted of microfibrils,^{24,25} and this supports that the SICM measurement of the collagen shows the actual dimensions quite well.

Figure 5.2 demonstrates the line profile comparison of AFM and SICM imaging of the collagen intersection. D-periodic spacing of the dried collagen can be observed in the edge enhanced image (Figure 5.2a') and the scanning electron microscopy image (Figure 5.2f), and the characteristic length is 67 nm in this work.²⁵ A small protrusion indicated as point 1 in Figure 5.2e began appearing even in the raster scanning AFM image, but it is not obvious. In comparison, the AFM ARS and SICM images show the apparent contrast of

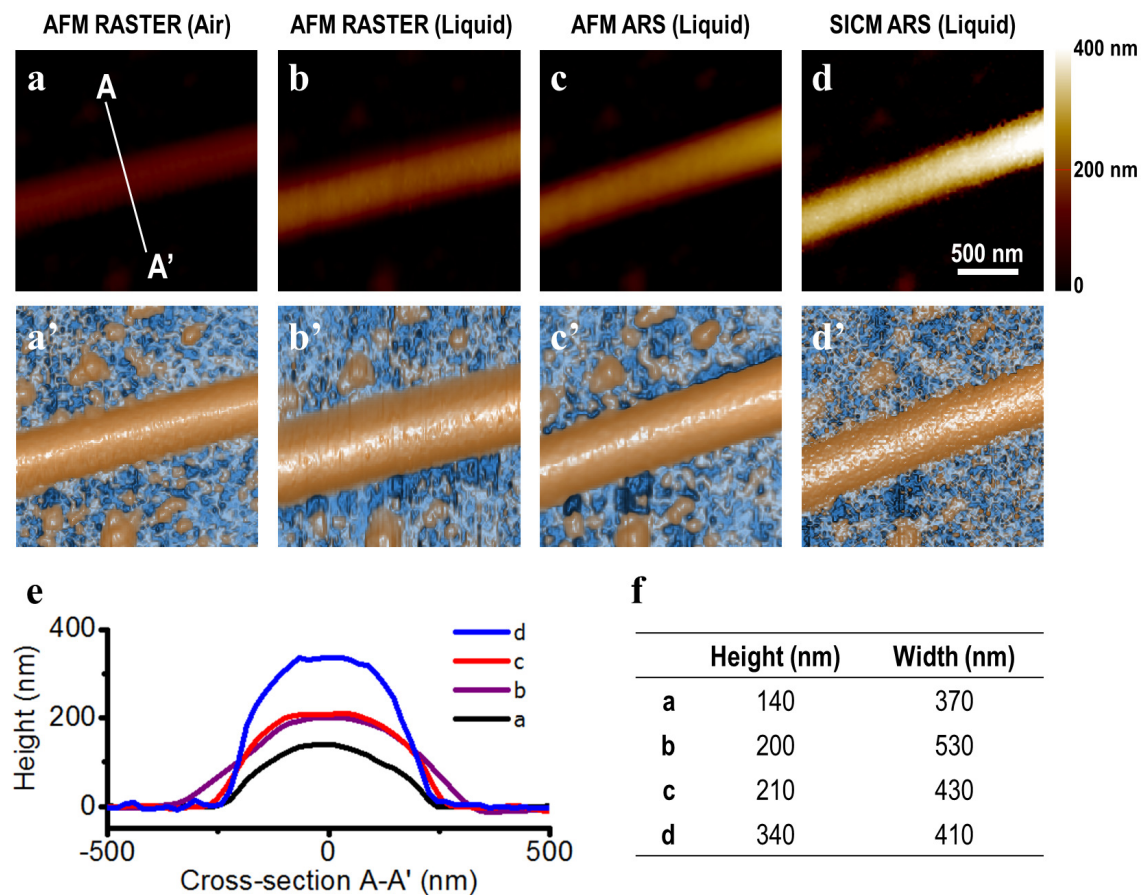


Figure 5.1 Comparison of AFM and SICM imaging capabilities of collagen fibrils. (a) Air dried collagen fibril on a petri dish was first imaged via AFM with raster scanning. The same sample immersed in saline; (b) was imaged via AFM with raster scanning, (c) was imaged via AFM with the approach and retract scanning (ARS) to minimize lateral artifact, and (d) was imaged via SICM with ARS. (a'-d') are edge-enhanced corresponding images in order to show the detailed structure. (e) Height profiles of cross-section A-A' of each image. (f) Measured height and width values for each profile.

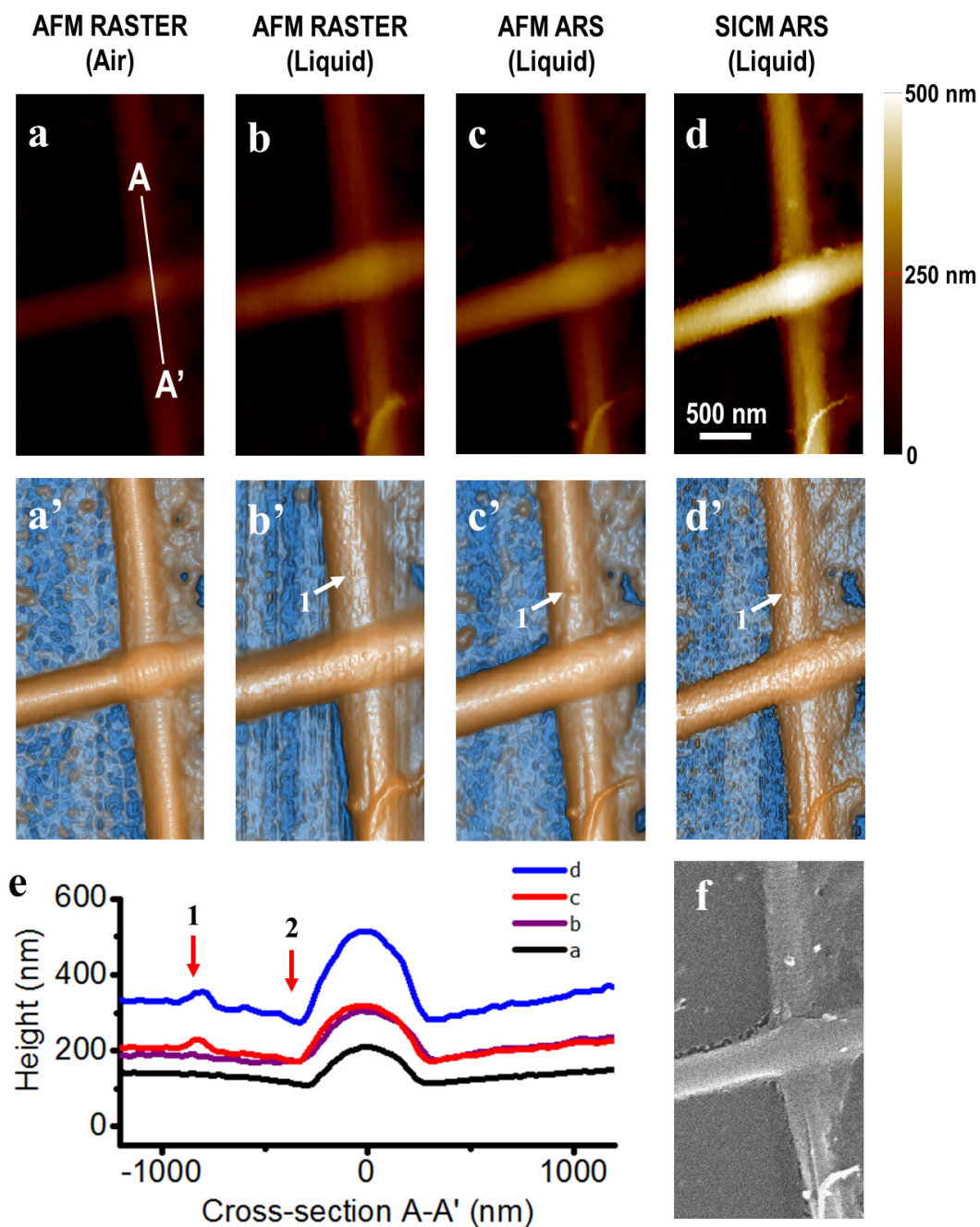


Figure 5.2 Line profile comparison of AFM and SICM imaging of the collagen intersection. (a) was air dried, (b-d) were immersed in saline collagen sample. (a) and (b) were imaged via AFM with raster scanning, (c) was imaged via AFM with ARS, and (d) was imaged via SICM with ARS. (a'-d') are edge-enhanced corresponding images showing the detailed structure. (e) Height profiles of cross-section A-A' of each image. (f) Scanning electron microscopy image of the same collagen fibril.

the protrusion even in corresponding images. The point 2 also clearly shows that the only SICM displays the deformation of the lower collagen from the strain of the upper collagen, and how each imaging mode could greatly affect the dimensional measurement.

5.3.2 Imaging a Cell

Figure 5.3 demonstrates AFM and SICM images of a fixed fibroblast cell. Unlike collagen fibrils, a fibroblast cell showed a higher degree of interaction between the AFM tip and the sample surface, even in a fixed condition. It was impossible to image the cell via raster scanning in AFM due to too much artifact.

Therefore, ARS was adopted to measure the height in pixel by pixel with minimized lateral disturbance both via AFM and SICM. However, even with minimized interactions, stretch marks were still visible in the fast scanning direction in AFM. Although ARS did not involve a lateral dragging force, AFM tip still applied vertical downward force on the sample so that the normal force deformed soft sample. In addition, outlines of the fibroblast cell were not distinct in AFM images (red arrows in Figure 5.3). On the other hand, SICM was capable of imaging the fibroblast three dimensionally without any noticeable artifact, and detailed structures on the cell surface were identifiable when certain areas were zoomed in. Line profile comparison of AFM and SICM images in Figure 5.3e also shows how the AFM tip could have exerted a downward force on the cell membrane causing the cell to appear smaller than its actual size.

The both AFM and SICM line profiles were processed with the zero height point at the around 16 μm position. The height of the fibroblast obtained in AFM was about 5 μm , which was significantly lower than the SICM measurement of about 9 μm .

5.4 Conclusions

In recent years, the SPM technique has become an increasingly versatile tool in the biological studies, especially in addressing critical questions associated with biological surfaces. Indeed, the biological surface and interface supports a wide range of biological pro-

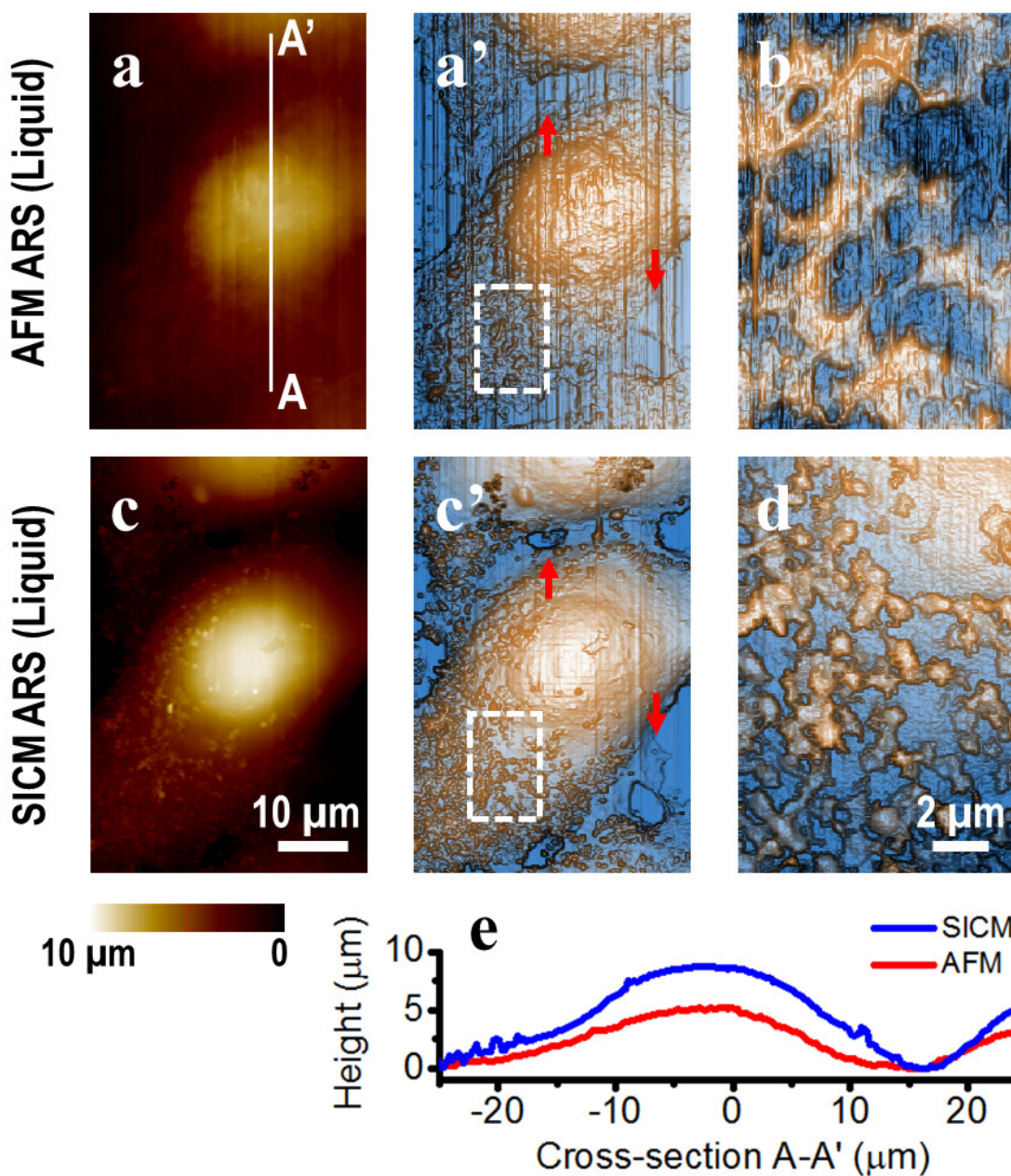


Figure 5.3 AFM and SICM images of fixed fibroblast. (a), (a') and (b) were obtained via AFM ARS method. The tip-sample interaction artifact was manifested as stretch marks in the direction of the fast scan. (c), (c') and (d) were obtained from SICM ARS method. (a') and (c') are edge-enhanced images. (b) and (d) are edge-enhanced zoomed in images corresponding to areas bound by the white dotted boxes in (a') and (c'), respectively. (e) Line profile comparison of AFM and SICM images along to the line A-A'. The line profile comparison suggested that the downward force applied in AFM is greater than in SICM.

cesses such as transport, cellular recognition, and signal transduction, to name a few. With the capability to study these structures and their respective functions in a *contact-free* liquid format with nanoscale resolution, there are many opportunities for the SPM technique to improve on current measurement capabilities in the biomedical sciences.^{26–28}

The present study shows the capability of AFM and SICM for imaging different types of biological samples in a liquid environment. There have been many reports showcasing AFM and SICM images separately, but few on the comparison of the two types of images.^{19,29,30} However, there has been no reports comparing amplitude-modulation AFM with the vertical approach method and SICM performed on the same sample. This work shows how different AFM and SICM imaging modes can affect the dimensional measurement of the sample.

Although there have been plenty of reports involving AFM images used for dimensional measurement of various biological samples, many did not consider artifacts arising from the tip-sample interactions. AFM measurement varies quite dramatically upon changes in the bulk and local environment, type of cantilever used as well as imaging mode. Therefore, for the determination of actual dimensions, AFM tip artifacts must be taken into account.

However, SICM can be utilized for obtaining *contact-free* images of the surface topography of biological samples, and it minimizes the alteration of the dimensional measurement. SICM conducted in ARS mode is especially powerful for imaging samples with steep slopes.¹⁵ The lateral resolution of ARS mode SICM is estimated about 150 nm in this work, and it is dependent on the pipette radius.³¹ The resolution of SICM could affect the dimensional measurement, but the measurement changes correlate with pipette radius regularly (data not shown). The minimized error associated with SICM imaging opens up the possibility of using it as a quantitative tool to measure dimensions of biological samples. While image resolution is still better in AFM than in SICM for some samples, an obvious advantage of the latter lies in the ability to obtain images *contact-free*. As such, SICM is an excellent tool for observing live cells and non-fixed soft samples. Taken together, SICM imaging, especially when conducted in ARS mode, is expected to be useful for ob-

taining images that reveal the actual three-dimensional topography of biological samples with accurate dimensions.

There are many important applications in the biomedical sciences where a balance among imaging resolution, a method of sample preparation, and a measurement principle must be achieved in order to effectively probe the surfaces of live biological samples. The imaging capabilities of SICM lend the technique significant potential to meet this balance and reveal physiologically relevant insights for clinical diagnosis, molecular toxicology, and pharmaceutical drug development.

References

- (1) Binnig, G.; Quate, C. F.; Gerber, C. Atomic force microscope. *Phys. Rev. Lett.* **1986**, *56*, 930–933.
- (2) Butt, H.-J.; Wolff, E.; Gould, S.; Northern, B. D.; Peterson, C.; Hansma, P. Imaging cells with the atomic force microscope. *J. Struct. Biol.* **1990**, *105*, 54–61.
- (3) Henderson, E.; Haydon, P.; Sakaguchi, D. Actin filament dynamics in living glial cells imaged by atomic force microscopy. *Science* **1992**, *257*, 1944–1946.
- (4) You, H. X.; Lau, J. M.; Zhang, S.; Yu, L. Atomic force microscopy imaging of living cells: a preliminary study of the disruptive effect of the cantilever tip on cell morphology. *Ultramicroscopy* **2000**, *82*, 297–305.
- (5) Hansma, P. K.; Drake, B.; Marti, O.; Gould, S. A.; Prater, C. B. The scanning ion-conductance microscope. *Science* **1989**, *243*, 641–3.
- (6) Korchev, Y. E.; Milovanovic, M.; Bashford, C. L.; Bennett, D. C.; Sviderskaya, E. V.; Vodyanoy, I.; Lab, M. J. Specialized scanning ion-conductance microscope for imaging of living cells. *J. Microsc.* **1997**, *188*, 17–23.
- (7) Korchev, Y. E.; Bashford, C. L.; Milovanovic, M.; Vodyanoy, I.; Lab, M. J. Scanning ion conductance microscopy of living cells. *Biophys. J.* **1997**, *73*, 653–658.
- (8) Korchev, Y. E.; Gorelik, J.; Lab, M. J.; Sviderskaya, E. V.; Johnston, C. L.; Coombes, C. R.; Vodyanoy, I.; Edwards, C. R. W. Cell volume measurement using scanning ion conductance microscopy. *Biophys. J.* **2000**, *78*, 451–457.

- (9) Klenerman, D.; Korchev, Y. E.; Davis, S. J. Imaging and characterisation of the surface of live cells. *Curr. Opin. Chem. Biol.* **2011**, *15*, 696–703.
- (10) Anariba, F.; Anh, J. H.; Jung, G. E.; Cho, N. J.; Cho, S. J. Biophysical Applications of Scanning Ion Conductance Microscopy (SICM). *Mod. Phys. Lett. B* **2012**, *26*, 1130003.
- (11) Happel, P.; Thatenhorst, D.; Dietzel, I. D. Scanning ion conductance microscopy for studying biological samples. *Sensors* **2012**, *12*, 14983–15008.
- (12) Kim, J.; Kim, S.-O.; Cho, N.-J. Alternative configuration scheme for signal amplification with scanning ion conductance microscopy. *Rev. Sci. Instrum.* **2015**, *86*, 023706.
- (13) Jung, G.-E.; Noh, H.; Shin, Y. K.; Kahng, S.-J.; Baik, K. Y.; Kim, H.-B.; Cho, N.-J.; Cho, S.-J. Closed-loop ARS mode for scanning ion conductance microscopy with improved speed and stability for live cell imaging applications. *Nanoscale* **2015**, *7*, 10989–10997.
- (14) Edwards, M. A.; Williams, C. G.; Whitworth, A. L.; Unwin, P. R. Scanning ion conductance microscopy: a model for experimentally realistic conditions and image interpretation. *Anal. Chem.* **2009**, *81*, 4482–92.
- (15) Novak, P.; Li, C.; Shevchuk, A. I.; Stepanyan, R.; Caldwell, M.; Hughes, S.; Smart, T. G.; Gorelik, J.; Ostanin, V. P.; Moss, G. W. J.; Frolenkov, G. I.; Klenerman, D.; Korchev, Y. E. Nanoscale live-cell imaging using hopping probe ion conductance microscopy. *Nat. Methods* **2009**, *6*, 279–282.
- (16) Happel, P.; Hoffmann, G.; Mann, S. A.; Dietzel, I. D. Monitoring cell movements and volume changes with pulse-mode scanning ion conductance microscopy. *J. Microsc.* **2003**, *212*, 144–151.
- (17) Happel, P.; Dietzel, I. D. Backstep scanning ion conductance microscopy as a tool for long term investigation of single living cells. *J. Nanobiotechnol.* **2009**, *7*, 7.
- (18) Takahashi, Y.; Murakami, Y.; Nagamine, K.; Shiku, H.; Aoyagi, S.; Yasukawa, T.; Kanzaki, M.; Matsue, T. Topographic imaging of convoluted surface of live cells by scanning ion conductance microscopy in a standing approach mode. *Phys. Chem. Chem. Phys.* **2010**, *12*, 10012–10017.

- (19) Ushiki, T.; Nakajima, M.; Choi, M.; Cho, S.-J.; Iwata, F. Scanning ion conductance microscopy for imaging biological samples in liquid: A comparative study with atomic force microscopy and scanning electron microscopy. *Micron* **2012**, *43*, 1390–1398.
- (20) Kado, H.; Yamamoto, S.-i.; Yokoyama, K.; Tohda, T.; Umetani, Y. Observation of contact holes by atomic force microscopy with a ZnO whisker tip. *J. Appl. Phys.* **1993**, *74*, 4354–4356.
- (21) Hosaka, S.; Morimoto, T.; Kuroda, H.; Minomoto, Y.; Kembo, Y.; Koyabu, H. New AFM imaging for observing a high aspect structure. *Appl. Surf. Sci.* **2002**, *188*, 467–473.
- (22) Radmacher, M.; Cleveland, J. P.; Fritz, M.; Hansma, H. G.; Hansma, P. K. Mapping interaction forces with the atomic force microscope. *Biophys. J.* **1994**, *66*, 2159.
- (23) Rosa-Zeiser, A.; Weilandt, E.; Hild, S.; Marti, O. The simultaneous measurement of elastic, electrostatic and adhesive properties by scanning force microscopy: pulsed-force mode operation. *Meas. Sci. Technol.* **1997**, *8*, 1333.
- (24) Orgel, J. P. R. O.; Irving, T. C.; Miller, A.; Wess, T. J. Microfibrillar structure of type I collagen in situ. *Proc. Natl. Acad. Sci.* **2006**, *103*, 9001–9005.
- (25) Fang, M.; Holl, M. M. B. Variation in type I collagen fibril nanomorphology: the significance and origin. *BoneKEy Reports* **2013**, *2*, DOI: 10.1038/bonekey.2013.128.
- (26) Mizutani, Y.; Choi, M.-H.; Cho, S.-J.; Okajima, T. Nanoscale fluctuations on epithelial cell surfaces investigated by scanning ion conductance microscopy. *Appl. Phys. Lett.* **2013**, *102*, 173703.
- (27) Yoo, Y.-Y.; Jung, G.-E.; Kwon, H.-M.; Bae, K.-H.; Cho, S.-J.; Soh, K.-S. Study of Mast Cells and Granules from Primo Nodes Using Scanning Ionic Conductance Microscopy. *J. Acupunct. Meridian Stud.* **2015**, *8*, 281–287.
- (28) Tanaka, A.; Tanaka, R.; Kasai, N.; Tsukada, S.; Okajima, T.; Sumitomo, K. Time-lapse imaging of morphological changes in a single neuron during the early stages of apoptosis using scanning ion conductance microscopy. *J. Struct. Biol.* **2015**, *191*, 32–38.

- (29) Rheinlaender, J.; Geisse, N. A.; Proksch, R.; Schaffer, T. E. Comparison of scanning ion conductance microscopy with atomic force microscopy for cell imaging. *Langmuir* **2011**, *27*, 697–704.
- (30) Seifert, J.; Rheinlaender, J.; Novak, P.; Korchev, Y. E.; Schäffer, T. E. Comparison of Atomic Force Microscopy and Scanning Ion Conductance Microscopy for Live Cell Imaging. *Langmuir* **2015**, *31*, 6807–6813.
- (31) Rheinlaender, J.; Schaffer, T. E. Lateral Resolution and Image Formation in Scanning Ion Conductance Microscopy. *Anal. Chem.* **2015**, *87*, 7117–24.

Chapter 6*

Mechanical Property Measurement by AFM and SICM

Cell fixation is a necessary step to preserve cell samples for a wide range of biological assays involving histochemical and cytochemical analysis. Paraformaldehyde (PFA) has been commonly used as a cross-linking fixation agent. It has been empirically recognized in a standard protocol that the PFA concentration C_{PFA} for the cell fixation is 4%. However, it is still not clear how the conventional protocol of C_{PFA} is optimized. Here, the detailed process of cell fixation as a function of C_{PFA} in terms of mechanical properties is investigated. The Young's modulus E of cells and the apparent fluctuation amplitude a_m of apical cell membrane were almost constant in a lower $C_{PFA} < 0.1\%$ and the same as the untreated cells. In an intermediate C_{PFA} between 0.1% and 4%, E was dramatically increased and a_m was abruptly decreased, indicating that cells begin to fix at $C_{PFA} = \text{ca. } 0.1\%$. Moreover, these quantities were unchanged in a higher $C_{PFA} > 4\%$, indicating that the cell fixation is stabilized at $C_{PFA} = \text{ca. } 4\%$, which corresponds to the empirical concentration of cell fixation optimized in a biological protocol. These results suggest that the mechanical property of cells probed by scanning probe microscopy could be a useful measurement to quantitatively estimate the validity of various biological protocols and techniques such as fixation processes.

*This chapter published substantially as Kim, S.-O.†; Kim, J.†; Okajima, T.; Cho, N.-J. Mechanical properties of paraformaldehyde-treated individual cells investigated by atomic force microscopy and scanning ion conductance microscopy. *Nano Convergence* **2017**, 4, 5. († denotes equal contribution)

6.1 Introduction

Cell fixation is an essential process for histology analyses in the clinical diagnosis. The main purpose of cell fixation is to preserve cells or cellular components as lifelike-state. Typically, when cells are degraded or dehydrated, cell components, such as protein, membrane, and intracellular structures can also get altered or degraded.¹ Additionally, the cell surface structure collapses and diffuses away during the antibody incubations and washing steps. However, cell fixation can prevent unexpected changes, and chemical and physical characteristics of cells can be observed consistently. Furthermore, cell fixation provides an efficient approach for immunostaining by allowing the antibodies to access intracellular structures.²

Among various fixation agents for cross-linking cell membrane and cytoplasmic protein, paraformaldehyde (PFA) is one of the most widely used chemical agents for cell and even tissue samples.¹⁻³ Generally, PFA causes covalent cross-links between molecules, effectively gluing them together into an insoluble meshwork so that mechanical properties of cell surface changes. Previous studies reported that the cell surface could be hardened after fixative treatment.⁴⁻⁷ Also comparing with an unfixed cell, mechanical properties of a fixed cell is more uniform on the entire cell surface.⁸ However, there is no systematic assessment of correlation between changes in mechanical properties of live and fixed cells. The understanding of the detailed process of cell fixation in various states from live cells to completely fixed cells will provide optimized cell fixation protocol.

This study investigates the mechanical properties of cell surface structures as a function of PFA concentration C_{PFA} by scanning probe microscopy (SPM) such as atomic force microscopy (AFM) and scanning ion conductance microscopy (SICM) by measuring the elastic modulus and the surface fluctuation amplitude, respectively, of cells in both living and fixed states. SICM uses ion current passing through the probe, nanopipette, to generate the feedback signal. This means, theoretically, there is no physical contact or damage between the SICM nanopipette and the sample surface. Since AFM is a force-based technique, nonzero forces are typically encountered during imaging, even in non-contact and

tapping mode.^{9,10} These forces increase the probability of damage to or deformation of soft and fragile features of biological samples.^{11,12} However, AFM has a powerful method for sensitive force measurements, force spectroscopy.¹³ Force spectroscopy is used for investigating mechanical properties of samples. Force-distance plot shows the sample changes as its loading force.^{14,15} In AFM force spectroscopy, the cantilever and the tip are moved directly towards the sample until they are in contact, then retracted again, so that the interaction force between the tip and the sample is measured.¹⁶

In here, mouse fibroblast as L929 cell was used for observing cell responses along with various PFA concentration C_{PFA} . To estimate the changes of the cell surface due to PFA treatment, SICM imaging mode and ion current-distance (I-D) mode were performed. The cell surface morphology changes can be monitored using SICM imaging mode and fluctuation of cell surface can also be determined by I-D mode.^{17,18} The Young's modulus, which is one of the most important mechanical properties, of each cell was performed by AFM force spectroscopy.^{7,19} The direct comparison of biological and physical changes of cells due to C_{PFA} was carried out. Based on the sequential concentration of PFA, they have different roles and present different cell behaviors depending on concentration. To allow appropriate and reproducible result, the live cell chamber was used for all measurements.

6.2 Materials and Methods

6.2.1 L929 Cells and Viability Assay

L929 fibroblast cells (ATCC, US) were cultured in Dulbecco's modified eagle medium (DMEM, Invitrogen, US) supplemented with 10 % fetal bovine serum (Thermo Fisher Scientific, US) and 1 % penicillin/streptomycin (Invitrogen Life Technique, US) at 37 °C temperature in humidified atmosphere containing 5 % CO₂. The cells with the density of 10⁴ mL⁻¹ on a 35 mm diameter cell culture petri dish (NUNC, Denmark) were washed with phosphate buffered saline (PBS, Sigma-Aldrich, US) three times and then treated with different PFA solutions (10⁻⁵ %, 10⁻⁴ %, 0.1 %, 1 %, 4 %, 8 % and 10 %) for 5 minutes. Before AFM and SICM experiments, the treated cell samples were washed three times again with PBS.

To evaluate the viability of PFA-treated cells, a LIVE/DEAD[®] Viability/Cytotoxicity Kit (L3224; Invitrogen, US) was used. Briefly, the PFA treated cells were immediately incubated using the live and dead stain fluorescence dye for 10 minutes. Then the final 2 μ M calcein AM and 4 μ M EtD-1 mixture solution were added to the PFA treated cell sample. For the fluorescence imaging, the commercial fluorescence microscope (Eclipse Ti, Nikon, Japan) was adopted. In fluorescence images, the green color was used to identify live cells, and the red color was used to identify dead cells.

6.2.2 SPM Apparatus

A commercial SPM system (NX-Bio, Park Systems, Korea) equipped with an inverted optical microscope (Nikon, Japan) was employed for AFM and SICM measurement in this study. All experiments using live cells were performed in the customized live cell chamber. Live cell chamber (Live Cell Instrument, Korea) provides a specific environment needed for live cell culture in particular space. In the live cell chamber, it is possible to set the temperature at 37 °C, 5 % CO₂ to maintain 7.4 pH, and around 95 % humidity to prevent medium evaporation. In this environment, live cell imaging by SICM and force spectroscopy by AFM are possible for a long period with optical monitoring such as phase contrast and differential interference contrast (DIC) microscopy.

6.2.3 Cell Fluctuation Analysis by SICM

SICM imaging and ion current-distance (I-D) curve experiments were performed with 100 nm inner diameter nanopipette which fabricated from borosilicate capillaries (inner diameter 0.6 mm, outer diameter 1.0 mm, World Precision Instruments, US) using CO₂ laser pipette puller (P-2000, Sutter Instruments, US). SICM cell surface images were obtained in hopping mode,²⁰ while the cell was being cultured in the live cell chamber. The nanopipette approached a sample surface until the pre-set threshold, which was 98.8 % in this study.

To evaluate the cell fluctuation, Mizutani et al. model was employed.¹⁸ This model proposed the relationship between cell surface fluctuation and I-D curve measurement. The measured ion current with cell fluctuation is convolution of non-fluctuation ion-current

relation, I_0 , and the probability of fluctuation, P ,

$$\langle I(z - z_0, \delta z_s) \rangle = \int_{-\infty}^{\infty} I_0(z - z_s) P(z_s - z_0, \delta z_s) dz_s. \quad (6.1)$$

The $\langle \cdot \rangle$ represents the expectation or the measured value. z and z_s are the absolute position of the pipette and the sample. z_0 and δz_s are the average position and the deviation of the sample fluctuation. The non-fluctuation ion-current relation is well known as the following form,

$$I_0(z - z_0) = I_{sat} \left(1 + \frac{A}{z - z_0} \right)^{-1} \quad (6.2)$$

where I_{sat} is the reference current when the pipette is far enough from the sample surface, and A is a constant from the pipette geometry.²¹ If the cell fluctuation obeys the Gaussian distribution,

$$P(z_s - z_0, \delta z_s) = \frac{1}{\delta z_s \sqrt{2\pi}} \exp \left(-\frac{1}{2} \left(\frac{z_s - z_0}{\delta z_s} \right)^2 \right). \quad (6.3)$$

Sixty I-D curves were performed at the center of cells, and the measured I-D curves were fitted with the equation (6.3) to identify the fluctuation deviation δz_s . I_{sat} and A were determined experimentally, and $I_{sat} = 1$ nA and $A = 4.9 \times 10^{-2}$ nm in this study.

6.2.4 AFM Measurements of Young's Modulus of Cells

The force curve measurements of AFM were performed to estimate the Young's modulus of cells. A commercial AFM cantilever (Biolever mini, Olympus, Japan) with 0.1 N m^{-1} of a typical spring constant was used. Since a cantilever with a small spring constant makes a relatively large deflection for a small force, the cantilever used in this study provides a reliable data of the cell surface structure. The spring constant of the AFM cantilevers was calibrated using the thermal vibration method.²² The AFM cantilever was cleaned using ethanol and exposed to UV for 30 minutes to remove contamination on the AFM cantilever and tip. More than fifty force-distance curves with 512 data points were measured. The scan rate of the AFM cantilever and the maximum loading force were set to be $1 \mu\text{m s}^{-1}$ to $2 \mu\text{m s}^{-1}$ and 3 nN to 8 nN, respectively.

The force curves were analyzed with a Hertz model using XEI, a commercial SPM data analysis program (Park Systems, Korea). If the AFM tip shape is four-sided pyramid with

a half cone angle α , so that the force on cantilever F is expressed by

$$F = \frac{E}{1 - \nu^2} \frac{\tan(\alpha)}{\sqrt{2}} \delta^2 \quad (6.4)$$

where E is the Young's modulus, ν is Poisson's ratio and δ is the indentation value.^{23,24} In this measurement, The Poisson's ratio and the cone angle were set to be 0.5 and 35°, respectively.

6.3 Results and Discussion

6.3.1 Topographic Images of Live and Fixed L929 Cell using SICM

Figure 6.1 shows the topography of an L929 cell imaged by SICM before and after treating with 4 % PFA, which is the conventional PFA concentration of cell fixation. No clear difference between the untreated and treated cells on the cell height is observed, but a small difference in the cell shape. The shapes of cell bodies look almost same in both images. The heights of the live and the fixed cell bodies are very similar. The live cell shows a maximum height of 2.5 μm (Figure 6.1c), the corresponding height in 4 % PFA treated cell appears around 2.5 μm (Figure 6.1d). However, the PFA-treated cells are slightly shrunken so that the cell adhesive area and the cell volume were lower than those of the untreated cell: the measured cell area and volumes are 910 μm^2 , and 770 μm^3 in the live cell and 880 μm^2 (3.5 % lower) and 720 μm^3 (7.4 % lower) in the 4 % PFA treated cell. Furthermore, the roughness of cell surface is larger in the treated cells. This is probably due to the cell shrinkage and the aggregated structures of cell surface protein.

6.3.2 Surface Fluctuations of Untreated and PFA-treated Cells

The I-D curves of the cell surface with various C_{PFA} were monitored. To estimate cell surface fluctuation, the measurement time of the I-D curve was about one second which means only a few nanometer surface dynamic morphological changes on the cell surface.¹⁸ Figure 6.2b indicates the representative I-D curves for untreated and PFA treated cells. The I-D curve on the solid substrate (petri dish) shows the steepest slope, and the I-D curve on the cell treated with 4 % PFA has the similar slope to the slope of the solid substrate. The

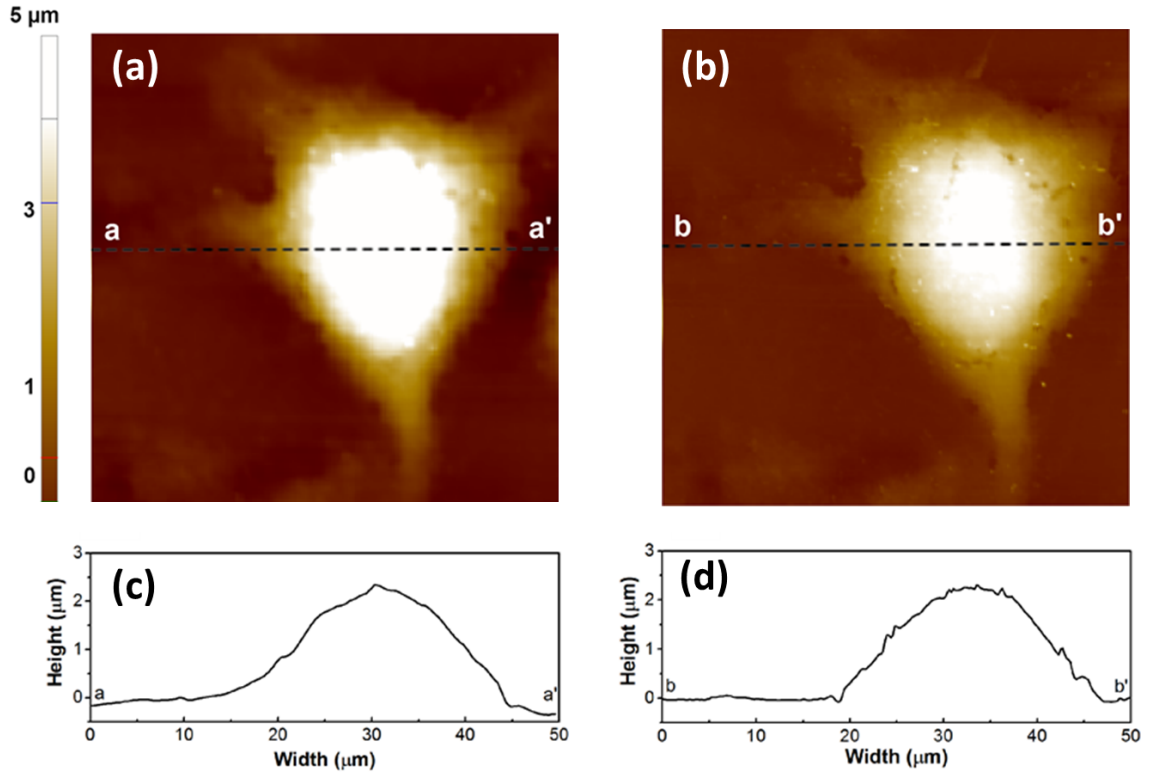


Figure 6.1 Single L929 fibroblast cell surface image using SICM before and after 4 % PFA treatment. (a) Height image of live fibroblast cell surface, (b) Height image of fixed fibroblast cell surface. The size of all images are $50\ \mu\text{m} \times 50\ \mu\text{m}$. (c) and (d) indicate line profiles of each image. Imaging time of each image is around 30 minutes.

I-D curve on the lower concentration PFA treated cell shows the gentlest slope. The all I-D curves in Figure 6.2b were fitted by the equation (6.3).

6.3.3 Young's Modulus of Untreated and PFA-treated Cells

To investigate the effect of PFA treatment on cell surface stiffness, the force spectroscopy measurements were performed on live and PFA treated cells (Figure 6.3a). Fifty force-distance curves at apex position on each cell surface were measured. Figure 6.3b indicates the typical force-separation curve for a live, 4 % PFA treated cell and a solid substrate (petri dish). The start point is the AFM tip far above the sample surface, corresponding to positions on the right side of the force-separation curve graph. As the AFM tip approaches the sample surface, the tip contacts the sample, after which the cantilever is deflected (the

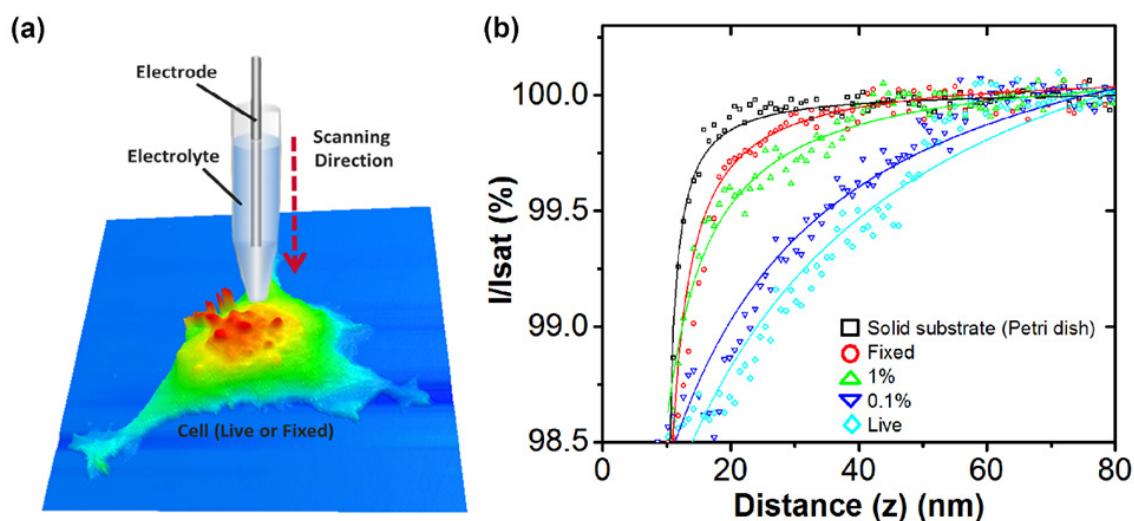


Figure 6.2 (a) Schematic view of the cell surface fluctuation setting by SICM, (b) Typical Ion current. Distance curve of the solid substrate (black), fixed cell (red), 1 % PFA treated cell (green), 0.1 % PFA treated cell (blue) and live cell (sky blue). The I-D curve on the solid substrate (petri dish) is the steepest, and the curve on the fixed cell is relaxed than on the solid substrate. The I-D curve of the live cell has the gentlest slope.

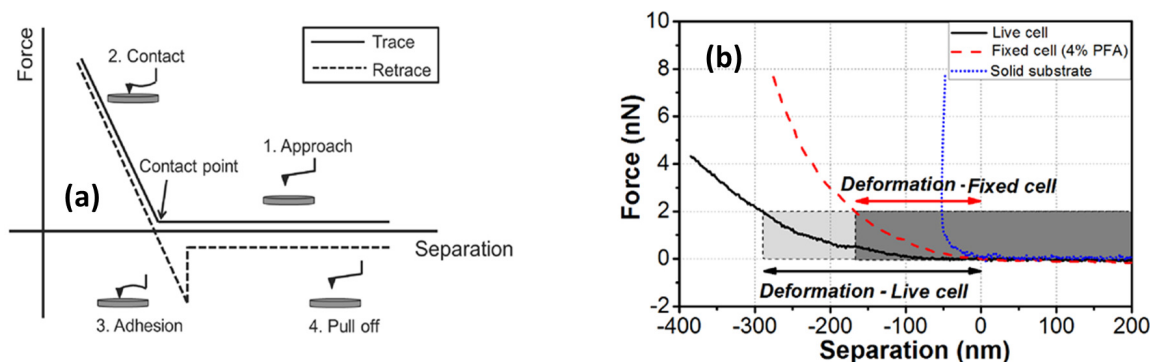


Figure 6.3 Force spectroscopy. (a) Schematic diagram of force spectroscopy. Force spectroscopy measures interaction between tip and sample on one point through Z scanner movement. As Z scanner is extended and shrunk, the tip pulls down on one point of the sample (solid line) and pulls off (dashed line). (b) The typical force-distance curve for fixed cell (4 % PFA treated cell, dashed-red) and live cell (solid-black). Compared with live cell case, the slope of fixed cell approach curve is steeper which means Young's modulus of fixed cell is bigger than live cell's one.

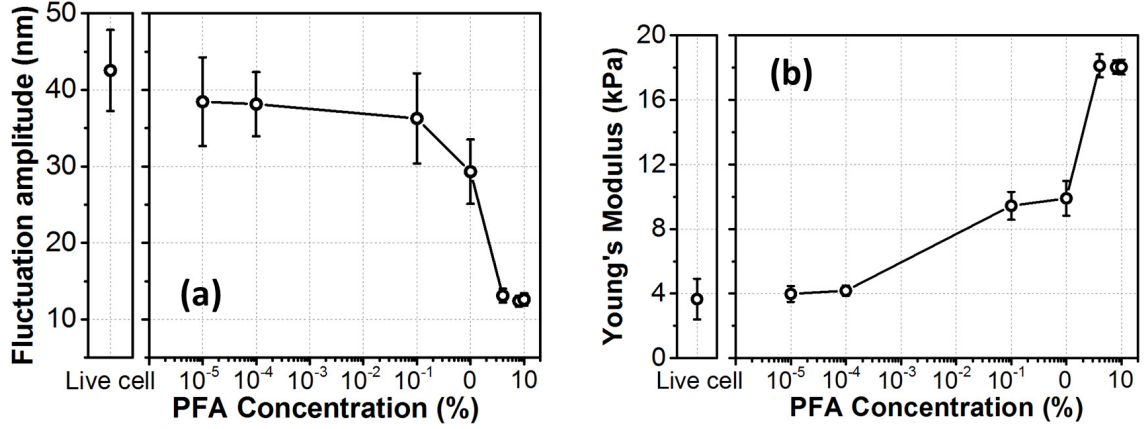


Figure 6.4 Surface fluctuation and Young's modulus. (a) RMS displacements of cell surface fluctuations. The displacements are approximately 12 nm on a fixed cell but, much larger on the live cell surface (43 nm). Live cell shows more active movement than fixed cell ($N = 60$). (b) Young's modulus for various kinds of PFA concentration of fibroblast cell. As expected, it indicates the higher concentration, the higher Young's modulus. Around 3.5 kPa on the live cell, approximately 18 kPa on fixed cell ($N = 50$).

left side of the force-separation curve graph). As expected, 4 % PFA treated cell exhibits much steeper slope than a live cell in force curve and the required force for surface indentation is also bigger than a live cell.

6.3.4 Cell Changes in Various PFA Concentrations

Figure 6.4a shows the root mean square (RMS) displacement of cell surface fluctuations on the treatment of different C_{PFA} . The estimated RMS displacement of surface fluctuations is approximately 12 nm on 4 % PFA treated cell. However, it increases gradually depending on the lower concentration. In the live cell, the displacements show the highest value around 43 nm, even though the chemical fixation caused no difference on cell surface topography (Figure 6.1c,d). It means that the live L929 cell had more active movement compared with PFA treated cell. One of the reasons of small surface fluctuation on PFA treated cell is that the PFA treatment causes cross-linking the proteins on membrane and cytoplasmic protein.

Table 6.1 shows apparent fluctuation amplitude and averaged Young's modulus values.

Table 6.1 Mean values and standard deviation (SD) of Young's modulus and fluctuation amplitude investigated at various PFA concentrations from live cell to 10 %

Paraformaldehyde Concentration (%)	Fluctuation Amplitude (nm)		Young's Modulus (kPa)	
	Mean	SD	Mean	SD
Live cell (0)	42.53	5.32	3.65	1.26
10^{-5}	38.45	5.81	3.97	0.49
10^{-4}	38.13	4.25	4.18	0.32
0.1	36.26	5.96	9.43	0.86
1	29.3	4.20	9.89	1.08
4	13.1	0.94	18.11	0.71
8	12.4	0.79	18.03	0.41
10	12.6	0.81	18.03	0.46

There is a distinguishable difference between the live and PFA treated cells (Fixed with 10^{-5} %, 10^{-4} %, 0.1 %, 1 %, 4 %, 8 % and 10 % PFA). The stiffness of the higher C_{PFA} treated cells (4 % the highest C_{PFA} treated cell is 18 kPa) increases gradually compared with the live cell (3.5 kPa). This difference in mechanical stiffness of cells on C_{PFA} is highly consistent with the I-D curve study, which means PFA treatment affects the cross-linking of cell surface proteins, like F-actin filaments.^{2,7,25-27} Specifically, it is assumed that the PFA fixation caused an increase of the cell stiffness depending on the available number of randomly distributed cross-linking sites on the cell surface. As shown in Figure 6.4b, the Young's modulus does not increase linearly with the C_{PFA} which suggests saturation in the number of available sites for surface protein cross-linking. Below the 0.1 % of C_{PFA} treatment, there is no significant effect on cell stiffness. However, when treated with high concentrations of PFA, over the 0.1 %, it produces dramatic changing of the cell stiffness.

Figure 6.5a shows live and dead cells from the staining kit. Green color represents live cells, and red color represents dead cells. As shown in this figure, from control to 0.1 % PFA treatment, most of the cells are alive. PFA treatment over 1 % shows intensely increase red positive cells, which means that a number cells are dead. Also, Figure 6.5b shows the quantitative analysis of live and dead ratio from staining data after PFA treatment.

The concentration C_{PFA} of 0.1 % to 1 % is the critical concentration for live and dead ratio exchange at this point. This agreement among cell surface fluctuation, Young's mod-

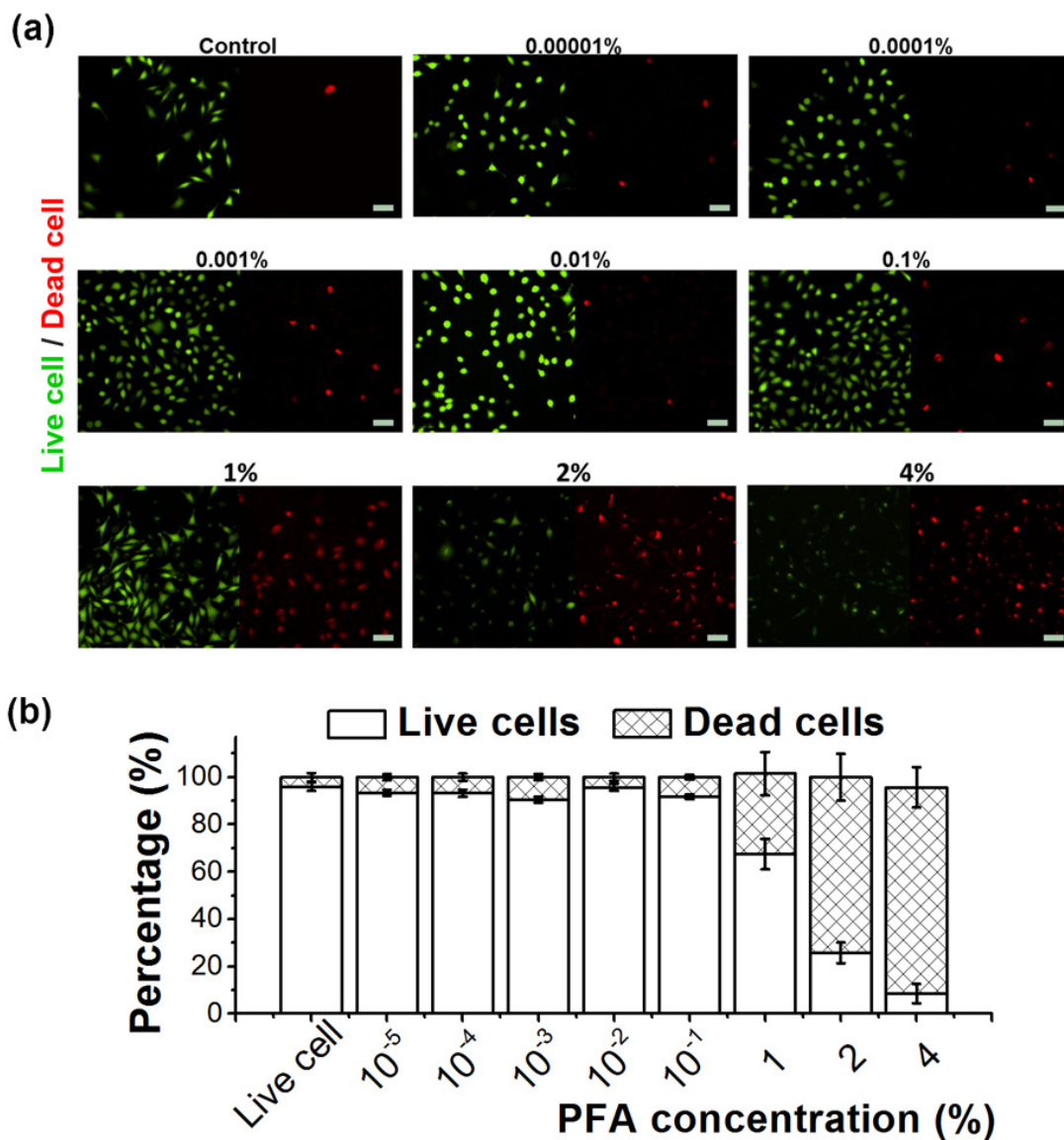


Figure 6.5 Evaluation of cytotoxicity property of PFA on the L929 cell. (a) Fluorescence microscopy image for assessment of live and dead cell ratio dependent on titration of C_{PFA} . Green color represents live cell, and red color represents dead cell. scale bar is 50 μm . (b) Graph of live/dead cell ratio depending on the titration of C_{PFA} . Data are presented as mean \pm standard deviation and significance were considered at $p < 0.05$ by Student's t-test.

ulus, and cell viability assay data supports the statement that the concentration of 0.1 % to 1 % is the trigger points for cell surface protein cross-linking. In other words, this PFA concentration of 0.1 % to 1 % produces many chances to approach the available number of cross-linking sites on the cell surface, with that, it affects cell survivability.

6.4 Conclusions

A fundamental comparison between live cells and fixed cells with various PFA concentration using AFM and SICM was demonstrated. The cell surface fluctuation measurement by I-D curve can estimate the viability of cells. The measurement of cell stiffness has been conducted by force spectroscopy. Because of PFA fixation, cell surface fluctuation value is 71 % less than the live cell, and the Young's modulus value is approximately 5-fold higher than that of live cells. The result presented in this chapter offers a broader insight for understanding cell behaviors in the chemical treatment; not only the traditional consideration of the effect of PFA on the cell, but also the more specifically studies of mechanical properties of cells.

Cell membranes are always flexible and variable. However, in a certain situation, such as chemical treatment, biological functions are changed, and morphological changes also occur. This is the reason why studying cell surface fluctuations is crucial for the understanding of cell function in relation to cell dynamics. SPM techniques can be well served as a promising tool for quantitative studies of both fixed and live cells.

References

- (1) Fox, C. H.; Johnson, F. B.; Whiting, J.; Roller, P. P. Formaldehyde fixation. *J. Histochem. Cytochem.* **1985**, *33*, 845–853.
- (2) Lanier, L.; Warner, N. Paraformaldehyde fixation of hematopoietic cells for quantitative flow cytometry (FACS) analysis. *J. Immunol. Methods* **1981**, *47*, 25–30.
- (3) Hopwood, D. Cell and tissue fixation, 1972–1982. *Histochem. J.* **1985**, *17*, 389–442.
- (4) Hoh, J. H.; Schoenenberger, C.-A. Surface morphology and mechanical properties of MDCK monolayers by atomic force microscopy. *J. Cell Sci.* **1994**, *107*, 1105–1114.

- (5) Braet, F.; Rotsch, C.; Wisse, E.; Radmacher, M. Comparison of fixed and living liver endothelial cells by atomic force microscopy. *Appl. Phys. A: Mater. Sci. Process.* **1998**, *66*, S575–S578.
- (6) Wu, H.; Kuhn, T.; Moy, V. Mechanical properties of L929 cells measured by atomic force microscopy: effects of anticytoskeletal drugs and membrane crosslinking. *Scanning* **1998**, *20*, 389–397.
- (7) Hutter, J.; Chen, J.; Wan, W.; Uniyal, S.; Leabu, M. Atomic force microscopy investigation of the dependence of cellular elastic moduli on glutaraldehyde fixation. *J. Microsc.* **2005**, *219*, 61–68.
- (8) Yamane, Y.; Shiga, H.; Haga, H.; Kawabata, K.; Abe, K.; Ito, E. Quantitative analyses of topography and elasticity of living and fixed astrocytes. *J. Electron Microsc.* (Tokyo) **2000**, *49*, 463–471.
- (9) Kim, J.; Choi, M.; Jung, G.-E.; Ferhan, A. R.; Cho, N.-J.; Cho, S.-J. Dimensional comparison between amplitude-modulation atomic force microscopy and scanning ion conductance microscopy of biological samples. *Jpn. J. of Appl. Phys.* **2016**, *55*, 08NB18.
- (10) Seifert, J.; Rheinlaender, J.; Novak, P.; Korchev, Y. E.; Schäffer, T. E. Comparison of Atomic Force Microscopy and Scanning Ion Conductance Microscopy for Live Cell Imaging. *Langmuir* **2015**, *31*, 6807–6813.
- (11) Rheinlaender, J.; Geisse, N. A.; Proksch, R.; Schaffer, T. E. Comparison of scanning ion conductance microscopy with atomic force microscopy for cell imaging. *Langmuir* **2011**, *27*, 697–704.
- (12) Anariba, F.; Anh, J. H.; Jung, G. E.; Cho, N. J.; Cho, S. J. Biophysical Applications of Scanning Ion Conductance Microscopy (SICM). *Mod. Phys. Lett. B* **2012**, *26*, 1130003.
- (13) Cappella, B.; Dietler, G. Force-distance curves by atomic force microscopy. *Surf. Sci. Rep.* **1999**, *34*, 15–3104.
- (14) Alonso, J. L.; Goldmann, W. H. Feeling the forces: atomic force microscopy in cell biology. *Life Sci.* **2003**, *72*, 2553–2560.
- (15) Santos, N. C.; Castanho, M. A. An overview of the biophysical applications of atomic force microscopy. *Biophys. Chem.* **2004**, *107*, 133–149.

- (16) Butt, H.-J.; Cappella, B.; Kappl, M. Force measurements with the atomic force microscope: Technique, interpretation and applications. *Surf. Sci. Rep.* **2005**, *59*, 1–152.
- (17) Gorelik, J.; Shevchuk, A. I.; Frolenkov, G. I.; Diakonov, I. A.; Kros, C. J.; Richardson, G. P.; Vodyanoy, I.; Edwards, C. R.; Klenerman, D.; Korchev, Y. E. Dynamic assembly of surface structures in living cells. *Proc. Natl. Acad. Sci.* **2003**, *100*, 5819–5822.
- (18) Mizutani, Y.; Choi, M.-H.; Cho, S.-J.; Okajima, T. Nanoscale fluctuations on epithelial cell surfaces investigated by scanning ion conductance microscopy. *Appl. Phys. Lett.* **2013**, *102*, 173703.
- (19) Lim, C.; Zhou, E.; Quek, S. Mechanical models for living cells—a review. *J. Biomech.* **2006**, *39*, 195–216.
- (20) Novak, P.; Li, C.; Shevchuk, A. I.; Stepanyan, R.; Caldwell, M.; Hughes, S.; Smart, T. G.; Gorelik, J.; Ostanin, V. P.; Moss, G. W. J.; Frolenkov, G. I.; Klenerman, D.; Korchev, Y. E. Nanoscale live-cell imaging using hopping probe ion conductance microscopy. *Nat. Methods* **2009**, *6*, 279–282.
- (21) Nitz, H.; Kamp, J.; Fuchs, H. A combined scanning ion-conductance and shear-force microscope. *Probe Microscopy* **1998**, *1*, 187–200.
- (22) Hutter, J. L.; Bechhoefer, J. Calibration of atomic-force microscope tips. *Rev. Sci. Instrum.* **1993**, *64*, 1868–1868.
- (23) Rico, F.; Roca-Cusachs, P.; Gavara, N.; Farré, R.; Rotger, M.; Navajas, D. Probing mechanical properties of living cells by atomic force microscopy with blunted pyramidal cantilever tips. *Phys. Rev. E* **2005**, *72*, 021914.
- (24) Lin, D. C.; Dimitriadis, E. K.; Horkay, F. Robust Strategies for Automated AFM Force Curve Analysis—I. Non-adhesive Indentation of Soft, Inhomogeneous Materials. *J. Biomech. Eng.* **2007**, *129*, 430.
- (25) Crawford, C.; Barer, R. The action of formaldehyde on living cells as studied by phase-contrast microscopy. *J. Cell Sci.* **1951**, *3*, 403–452.
- (26) Kiernan, J. A. Formaldehyde, formalin, paraformaldehyde and glutaraldehyde: what they are and what they do. *Microscopy today* **2000**, *1*.

- (27) Targosz-Korecka, M.; Daniel Brzezinka, G.; Danilkiewicz, J.; Rajfur, Z.; Szymonski, M. Glutaraldehyde fixation preserves the trend of elasticity alterations for endothelial cells exposed to TNF- α . *Cytoskeleton* **2015**, 72, 124–130.

Chapter 7*

Improvement on SICM Instrumentation

Scanning ion-conductance microscopy (SICM) uses an electrolyte filled nanopipette as a scanning probe and detects current changes based on the distance between the nanopipette apex and the target sample in an electrolyte solution. In conventional SICM, the pipette sensor is excited by applying the voltage as it raster scans near the surface. There have been attempts to improve upon raster scanning because it can induce collisions between the pipette sidewalls and a target sample, especially for soft, dynamic materials (e.g., biological cells). Recently, Novak et al. demonstrated that hopping probe ion conductance microscopy (HPICM) with an adaptive scan method can improve the image quality obtained by SICM for such materials. However, HPICM is inherently slower than conventional raster scanning. In order to optimize both image quality and scanning speed, an alternative configuration scheme for SICM signal amplification that is based on applying current to the nanopipette is studied. This scheme overcomes traditional challenges associated with low bandwidth requirements of conventional SICM.

*This chapter published substantially as Kim, J.; Kim, S.-O.; Cho, N.-J. Alternative configuration scheme for signal amplification with scanning ion conductance microscopy. *Rev. Sci. Instrum.* **2015**, 86, 023706.

7.1 Introduction

An electrolyte-filled nanopipette, which is pulled from a glass capillary, is used as the scanning ion-conductance microscope (SICM) probe.¹ In the earliest convention, the nanopipette was raster scanned across the surface while a feedback loop adjusts the vertical position in order to keep the ion conductance constant by adjusting the nanopipette tip height, enabling the topography of the surface to be mapped with high resolution.¹⁻⁴

As the SICM technique became popular, different modes were introduced. Those modes include direct current (DC),^{1,5} alternate current (AC),⁶⁻⁸ and hopping modes.⁹⁻¹³ DC mode was first utilized to demonstrate live cell imaging as it maintains a constant direct current on the sample surface during raster scanning. Since the direct current maintains the tip-sample distance while the scanning probe follows the lateral topography, it has an inherent limitation for scanning larger or coarse objects.⁷ In order to improve sensitivity and stability, AC mode was introduced by the superimposition of the DC signal with a current component.⁶ It operates similarly to tapping mode¹⁴ in AFM by modulating the pipette along the z-axis within few tens of nanometers, and detects the amplitude signal using a lock-in amplifier.⁶⁻⁸ Despite stable scanning of the sample topography in AC mode, the pipette can only detect the distance signal at its apex, and is hence not suitable for investigating the significant morphological variations inherent on cell surfaces.¹⁵

To circumvent the aforementioned challenges with SICM imaging, the hopping probe ion conductance microscope (HPICM) was introduced enabling the scanning probe to be retracted after each positional recording.⁹⁻¹³ In this mode, the probe approaches the sample until reaching the given setpoint vertically, records the distance from the initial z-position, returns to the initial z-position, then laterally moves to the next position. Possible interference of coarse or fluctuating morphology is minimized using this non-continuous scan approach. However, the advantages of this mode were initially offset by the requirement for an appreciably longer equivalent scan time due to the greater traveling distance of the pipette. To improve imaging speed in HPICM mode, Novak et al. introduced an adaptive algorithm based on a low resolution prescan of the entire sample followed by more detailed

imaging of regions that demand higher resolution analysis.¹⁵ With maturing SICM instrumentation field, there have hitherto been many successful demonstrations of various modes adapted to the requirements of particular applications. At the same time, all of these modes are fundamentally based on a voltage source, which means applying a constant voltage between the pipette electrode and the bath electrode and detecting changes in current flow through the nanopipette.

This work introduces an alternative configuration scheme for SICM measurements based on a current source, in which a constant current is applied from the pipette electrode to the bath electrode and detect changes in the voltage associated with the nanopipette. Based on the current source design, the fabrication of a prototype printed circuit board (PCB) configuration is reported that is compatible with a commercial SICM instrument. Analysis of the frequency response and noise spectrum of the current source shows better performance than the conventional voltage source. A microfabricated polydimethylsiloxane (PDMS) grating sample and the biological cell are imaged in the current source configuration scheme, and the results are compared with those obtained by a conventional voltage source. Possible applications of this new configuration scheme are discussed.

7.2 Theoretical Background

7.2.1 Limitation of Voltage Source Configuration

The conventional SICM circuit uses a voltage source to excite the system comprised of the pipette electrode, the electrolyte solution, and the bath electrode. This configuration can be divided and modeled as three resistances, the pipette resistance R_P , the access resistance R_{AC} , and the solution resistance R_S as shown in Figure 7.1. The pipette resistance R_P represents the resistance inside of the pipette and R_P is the resistance when the pipette is far from the sample surface. The cross-section of the pipette end is small and tapered so the pipette resistance typically reaches over 100 M Ω . The access resistance R_{AC} varies depending on the distance between the pipette apex and the sample surface. R_{AC} is zero when the pipette is far from the sample surface and increases when the pipette becomes closer to the sample surface, because the area of the ion current path between the pipette

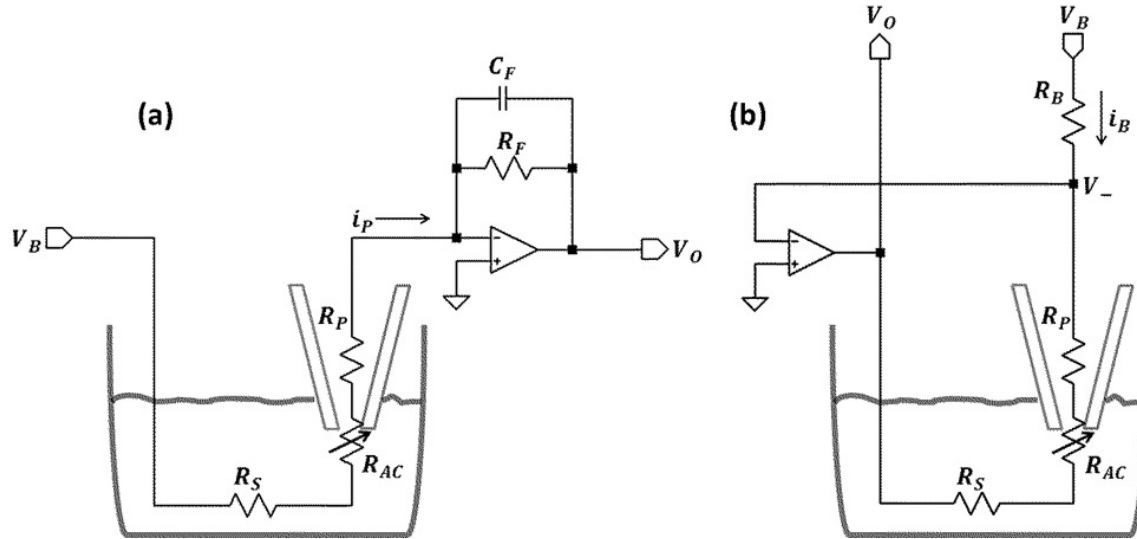


Figure 7.1 Principle of SICM signal amplification. The SICM pipette consists of the pipette resistance R_P and the access resistance R_{AC} , which varies corresponding to the distance between the pipette apex and the sample surface and the solution resistance R_S . (a) The conventional voltage source configuration. When voltage bias V_B is applied to the pipette, current i_P is generated. The amplifier converts i_P to voltage V_O with transimpedance gain R_F . (b) Alternative configuration scheme for signal amplification, current source configuration. An alternative configuration applies current i_B to the pipette, and detects voltage drop V_O .

and the surface is decreased. In most imaging conditions with the setpoint at 1 % to 2 % of R_P , the access resistance R_{AC} only contributes a small portion to the total pipette resistance. For mathematical convention, the access resistance can be simplified by

$$R_{AC} = R_P \delta(z) \quad (7.1)$$

where $\delta(z)$ is the dependent term of the distance between the pipette and the sample surface. The solution resistance R_S represents the bulk resistance from the access resistance to the bath electrode, but compared to the pipette resistance the solution resistance is negligible. Hence, the total resistance R_T between two electrodes can be expressed by

$$R_T = R_P + R_{AC} + R_S = R_P(1 + \delta(z)). \quad (7.2)$$

When applying a constant voltage between two electrodes using a voltage source, the current i_P is generated and its value changes based on the distance between the pipette and the

sample as follows

$$i_P = \frac{V_B}{R_T} = \frac{V_B}{R_P(1 + \delta(z))}. \quad (7.3)$$

To convert the generated current i_P into the voltage, a transimpedance amplifier is used.

The converted voltage of the current i_P is proportional to the feedback resistance R_F

$$V_O = R_F \cdot i_P. \quad (7.4)$$

The thermal noise of this transimpedance amplifier is $\sqrt{4k_B T R_F \text{BW}}$ where $k_B = 1.38 \times 10^{-23} \text{ J K}^{-1}$ is the Boltzmann's constant, T is the absolute temperature and BW is the bandwidth of interest. Considering the signal to noise ratio (SNR) of the transimpedance amplifier, the feedback resistance should be set at significantly higher values because the current gain is linearly proportional to R_F and the noise is proportional to $\sqrt{R_F}$. In this case, the SNR improves proportionally to $\sqrt{R_F}$. However, the resistor R_F has a stray capacitance C_F which is on the order of 0.1 pF in parallel. Therefore, the output voltage is dependent on the frequency and low pass-filtered with the bandwidth $f_0 = 1/2\pi R_F C_F$, which is mathematically expressed by

$$V_O(f) = \frac{i_P R_F}{1 + j \cdot f/f_0} \quad (7.5)$$

where $j = \sqrt{-1}$ is the imaginary number and f is the frequency. As such, it is not practical to set R_F too high because the high frequency signal is eliminated by the low-pass filtering.

This conventional voltage source configuration has a trade-off between SNR and bandwidth. If R_F is set at a higher value to get a higher SNR, the bandwidth is reduced. On the other hand, in order to get a higher bandwidth, the SNR is poorer. To balance SNR and proper bandwidth, the R_F is chosen to 1 G Ω in order to obtain a bandwidth of around 1 kHz for SICM measurements using the voltage source configuration in this work. To circumvent this trade-off between SNR and bandwidth, an alternate preamplifier circuit is required.

7.2.2 Current Source Configuration and its Characteristics

The alternate circuit uses a current source to apply a constant current i_B from the pipette electrode to the bath electrode and to detect the voltage changes between two electrodes as

shown in Figure 7.1b. When negative feedback of an operational amplifier (opamp) works, the two input nodes, inverting input ($-$) and non-inverting input ($+$) of the opamp become the same voltage, or the voltage of the inverting input node of opamp, V_- is virtually ground or 0 V, and the biasing current is determined by

$$i_B = \frac{V_B}{R_B} \quad (7.6)$$

The bias current i_B passes through two electrodes, the voltage drops the amount of total resistance R_T , and the output voltage is

$$V_O = -i_B R_T = -i_B R_P (1 + \delta(z)). \quad (7.7)$$

In contrast to the voltage source, the output voltage is independent of the circuit element because the applied voltage V_B and current i_B are constant during the operation. In other words, the bandwidth is not limited by circuit components when applying current to the pipette.

In addition, using a current source, the overall impedance of the circuit can be reduced. The output noise voltage of voltage source configuration, e_V and current source configuration, e_I are expressed by

$$e_V = \left(1 + \frac{R_F}{R_T}\right) \sqrt{4k_B T (R_T \parallel R_F) \text{ BW}} \quad (7.8)$$

$$e_I = \left(1 + \frac{R_T}{R_B}\right) \sqrt{4k_B T (R_T \parallel R_B) \text{ BW}} \quad (7.9)$$

where \parallel is the parallel resistance of the two resistors, $(R_1 \parallel R_2) = R_1 R_2 / (R_1 + R_2)$. The parallel resistance $(R_1 \parallel R_2)$ is less than R_1 and R_2 . As there is no opportunity to adjust the pipette resistance R_P , the minimum value of $(R_T \parallel R_F)$ is R_T when R_F is infinite. In the case of the current source, R_B should be smaller than R_T , and the output noise can be decreased independently from the pipette resistance.

Considering the applied power between two electrodes, the applied power in the current source configuration is proportional to the total resistance, $P = I_B^2 R_T$ whereas the applied power in the voltage source configuration is inversely proportional to the total resistance, $P = V_B^2 / R_T$. In the extreme case when the pipette is broken during imaging, and the pipette

resistance is reduced suddenly, the current source configuration is automatically reducing the power between two electrodes. This feature would be helpful to image living cell to avoid unnecessary electrical stimulus to cells in the worst case.

7.3 Materials and Methods

7.3.1 SICM and Nanopipettes

A commercial SICM (NX-Bio, Park Systems, Korea) was used as the SICM imaging platform. The nanopipette was fabricated from borosilicate capillaries which have 0.6 mm inner diameter and 1.0 mm outer diameter (Narishige, Japan) by using a CO₂-laser-based micropipette puller (P-2000, Sutter Instruments, US).

7.3.2 Measurement of Noise and Frequency Response

To test the alternative current source configuration, the noise and bandwidth of the two modes were performed with a resistor of 100 M Ω . The noise was measured by a data acquisition board (PCI-6251, National Instruments, US), and the data were recorded for 10 seconds with 200 kilo-samples per seconds (kSPS) after 10 kHz low-pass filter to prevent an aliasing effect and analyzed by a one-side power spectrum density. The frequency responses were taken using a lock-in amplifier (SR830, Stanford Research System, US).

7.3.3 L929 Fibroblast Cell

The cells were maintained in Dulbecco's Modified Eagle Medium (DMEM, Invitrogen, US) supplemented with 10 % fetal bovine serum (FBS, Gibco, US) and 1 % penicillin/streptomycin (Gibco, US) at 37 °C in a humidified atmosphere containing 5 % CO₂. The cells were harvested after trypsinization, washed and re-suspended at a concentration of 10⁵ cells/mL in normal growth medium for subculture. A 1 mL aliquot of the cells containing medium was seeded on the experimental petri dish at a concentration of 10³ cells/mL. After 3 days culture, the cells were washed by phosphate buffered saline (PBS) buffer 3 times and then treated with 4 % paraformaldehyde (PFA) solution for 5 minutes. Before imaging, the fixed cells were washed again two times with PBS buffer.

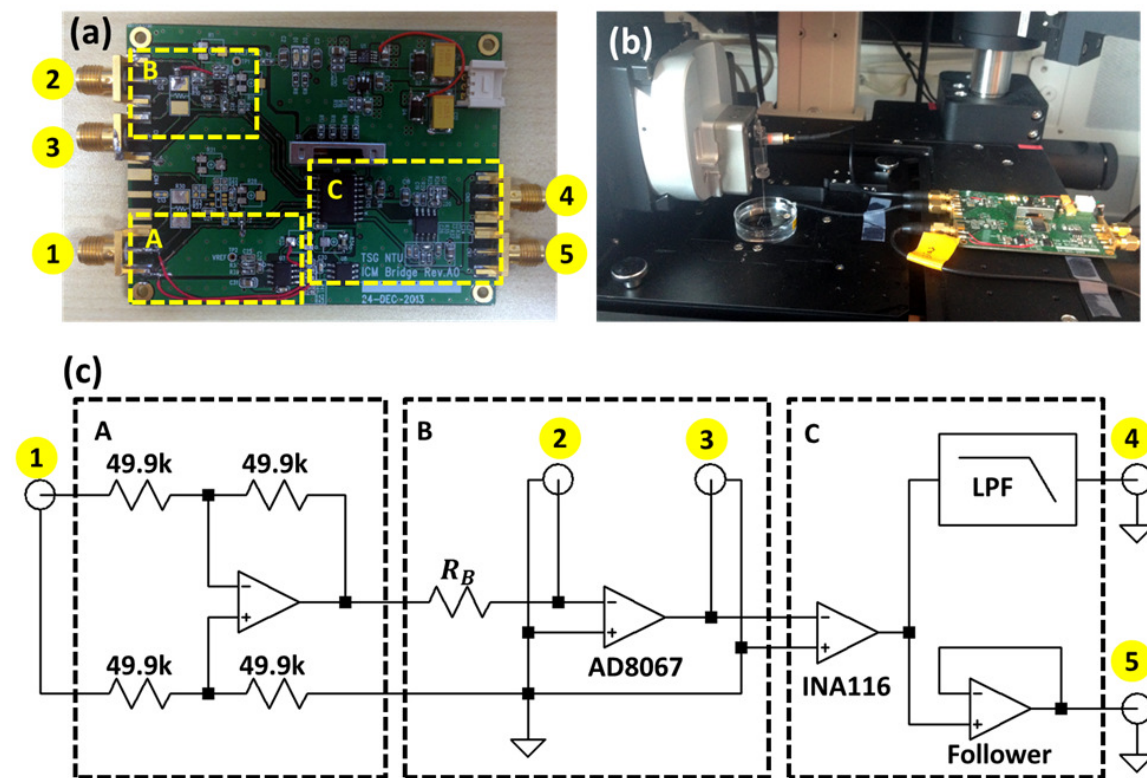


Figure 7.2 Implementation of the current source circuit. (a) The printed circuit board (PCB) for the current source configuration. (b) Experimental setup for current bias signal amplification mode. (c) A detailed schematic of the PCB. The external bias is connected to port 1, the pipette electrode and the bath electrode are connected to ports 2 and 3, respectively. Ports 4 and 5 are to monitor output voltage with and without low-pass filtering, respectively. Dotted panel A is for avoiding ground loop noise; dotted panel B is the main circuit of current bias signal amplification mode. Dotted panel C indicates additional signal conditioning for output filter and buffer.

7.3.4 Implementation of Current Source Configuration

The implementation of the current source configuration is shown in Figure 7.2. To interconnect the external voltage source, the differential amplifier was used for eliminating ground loop noise (panel A). The voltage controlled current source was designed with the field effect transistor (FET) input amplifier (AD8067, Analog Devices, US). This amplifier has a low input bias current, typically 1.0 pA, and has a wide gain bandwidth product (GBP), OPA128 and OPA129 (Texas Instruments, USA) can be used instead of AD8067. The bias resistor R_B is chosen to 10 M Ω to reduce the significance of the input offset volt-

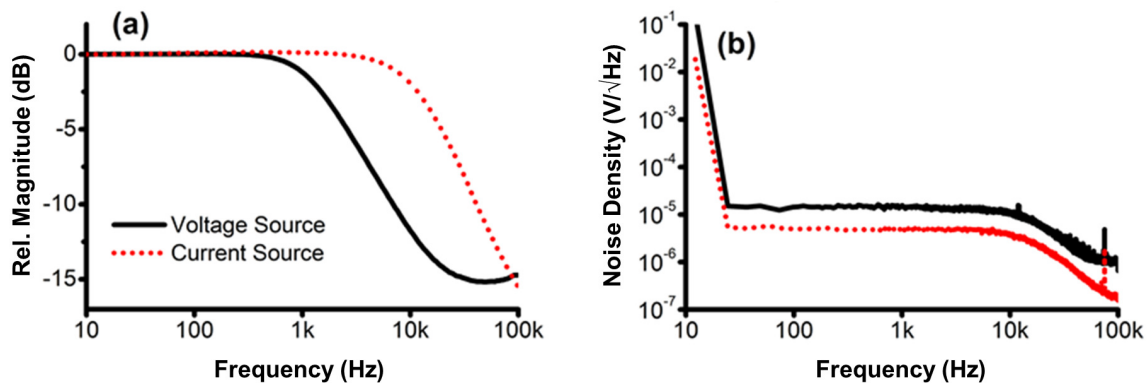


Figure 7.3 Comparison of bandwidth and noise of voltage and current source configurations. (a) Comparison of magnitude (dB) of two different signal amplification modes as a function of frequency (Hz). (b) Comparison of noise spectral density fixed at a resistance of 100 M Ω for two different signal amplification modes. Black solid is for voltage source and red dotted is for current source configuration.

age (AD8067 has 1 mV offset voltage in maximum), in comparison to the bias voltage V_B which is around 10 mV to 100 mV. Subminiature version A (SMA) connectors and cables were used to shield high impedance nodes from the pipette distance sensing system. In principle, it is better to connect the output of the opamp (port 3) to the bath electrode to block external noise because the electrolyte solution, which has a relatively lower impedance than the pipette resistance, might behave like a shield. The instrumentation amplifier (INA116, Texas Instruments, USA) was employed to detect the voltage difference between the non-inverting input and the inverting input of the FET input amplifier. Finally, the signal passed to the output through a 10 kHz 2nd order Bessel filter (port 4) for noise measurement and imaging, and the signal passed via the follower (port 5) for bandwidth measurement. Opamps for the low pass filter and others consisted of the general purpose amplifier (OPA2209, Texas Instruments, USA).

7.4 Results and Discussion

7.4.1 Comparison of Bandwidth and Noise

The frequency responses of both configurations are shown in Figure 7.3a. The relative magnitude-frequency plot in Figure 7.3 was prepared with normalized by the magnitude

of 10 Hz, and displayed in dB scale with $20 \log_{10}(V_O(f)/V_O(10 \text{ Hz}))$. The bandwidth of the voltage source configuration with 1 G Ω feedback resistor is 1.69 kHz as expected and the bandwidth of current source configuration is 13.2 kHz which is much higher than the voltage source configuration.

The noise voltage spectral density is plotted in Figure 7.3b. The spectral noise densities at 1 kHz are $15.7 \mu\text{V}/\sqrt{\text{Hz}}$ and $5.38 \mu\text{V}/\sqrt{\text{Hz}}$ for the voltage source and current source configurations, respectively. These values correspond well with the calculated thermal noise at 25 °C, $13.5 \mu\text{V}/\sqrt{\text{Hz}}$ from the equation (7.8) for the voltage source configuration, $4.26 \mu\text{V}/\sqrt{\text{Hz}}$ from the equation (7.9) for the current source configurations. The thermal noise from the current source configuration can easily be smaller than the thermal noise of R_P , the latter of which is $14.1 \mu\text{V}/\sqrt{\text{Hz}}$ in the 100 M Ω case.

7.4.2 Comparison of Image Quality

As discussed above, the noise and bandwidth signals of the current source configuration show improved performance compared to the voltage source configuration. To determine if a similar performance improvement can be realized in actual imaging conditions, imaging two samples in different SICM modes was performed: a grating sample in DC mode and an L929 fibroblast cell in hopping mode.

Before the imaging test, the current-distance curve of the voltage source and the voltage-distance curve of the current source configuration were investigated as shown in Figure 7.4a,d. The output of the voltage source configuration represents the conductance between the pipette and the bath electrodes, which can be interpreted as current, and the output of the current source configuration means the resistance between the two electrodes. The normalized output of the current source configuration increases when the pipette approaches the surface (Figure 7.4d) which contrasts with the decreasing output of the voltage source configuration (Figure 7.4a). The polarity of the feedback should be negated due to the polarity of the error signal, which is the difference between the setpoint and measured output voltage, $e = (\text{measured}) - (\text{setpoint})$, is reversed in the current source configuration. For example, when the error signal is a positive value, the pipette moves to the surface in the

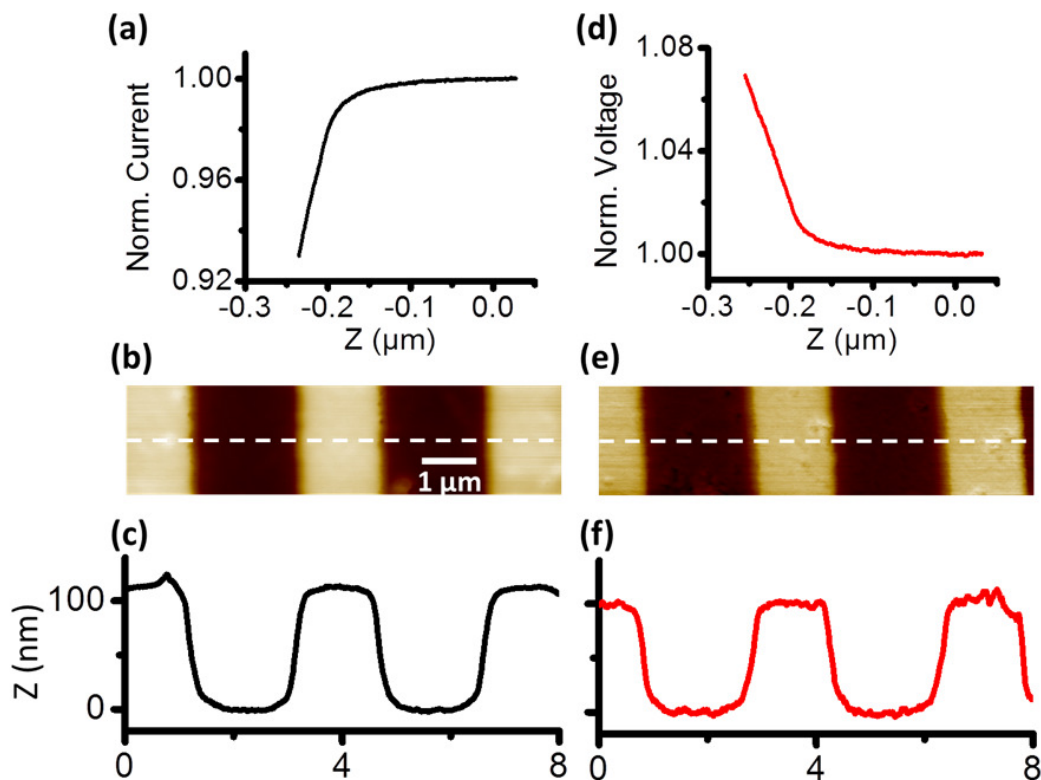


Figure 7.4 Comparison of SICM imaging in voltage and current source configurations. (a) The current-distance curve for voltage source configuration. (b) 8 μm by 2 μm standard PDMS grating image of the voltage source in DC mode, and (c) line profile of dashed-line (white) from the image. (d) Voltage-distance curve of current source configuration and (e) corresponding standard PDMS grating image and (f) line profile.

voltage source configuration, whereas the pipette moves away from the surface in the current source configuration with the same control software. Thus, the feedback software was modified to calculate the proper error signal for the current source configuration. DC mode SICM images of a grating sample are presented in Figure 7.4b,e, and the corresponding line profile is shown in Figure 7.4c,f. The sample was prepared on polydimethylsiloxane (PDMS) by stamping of a 118.5 nm height sample (TGZ02, MikroMasch, Bulgaria). The image and line profile obtained using a current source (Figure 7.4e,f) displays sharper details than the image obtained using a voltage source.

Furthermore, to demonstrate the utility of the alternative current source configuration

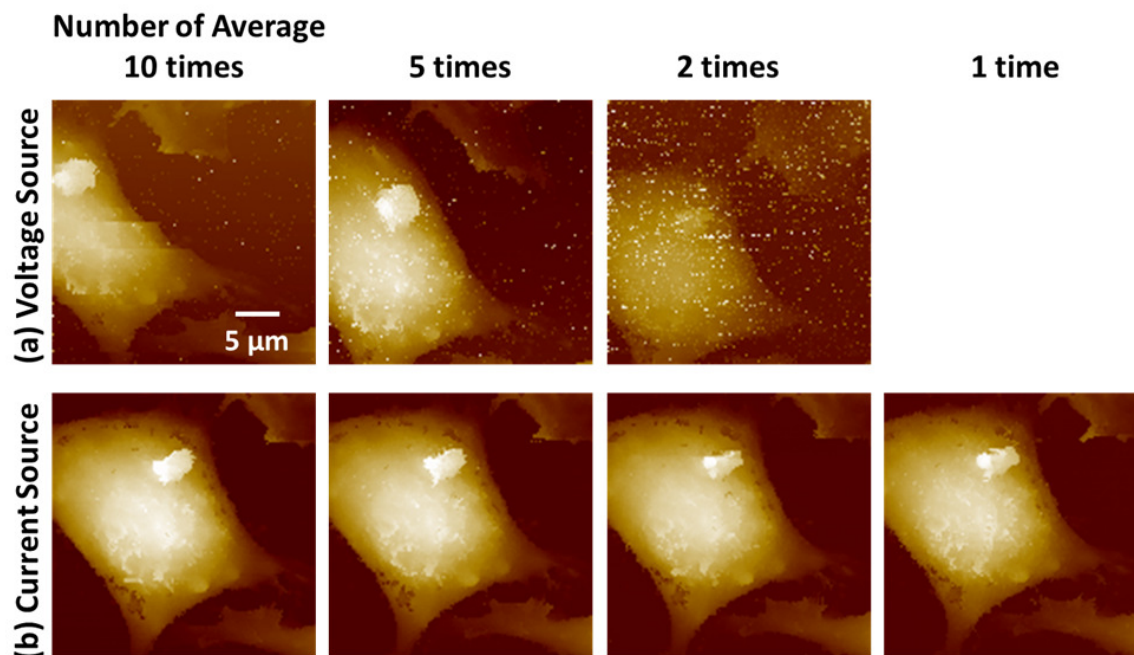


Figure 7.5 Comparison of cell images for the conventional voltage source and the modified current source configurations. (a) Using the voltage source configuration, L929 cells were imaged with a various number of digital average filter taps to compare image quality. The white dots indicate for noise. (b) Direct comparison of L929 cells images by the modified current source configuration. In the current source configuration, consistent image resolution can be obtained regardless of the number of average taps, even in the case of one-time average tap.

on soft biological samples, L929 fibroblast cell images were obtained (Figure 7.5). For direct comparison, the cell surface was scanned using hopping mode with a 1.5 % setpoint to compare between the voltage source and current source configurations. The control software stops the approach and records the height when the output voltage of the amplifier reaches the setpoint or $e \leq 0$. With a high noisy signal, the control software might stop before reaching the right setpoint value because the control software picks the noise, and the software records the height which is higher than the sample surface displaying the point as a white dot. To reduce the noise, a digital average filter is used and the number of digital average taps is related to the time duration for imaging.

In the voltage source configuration, in order to acquire a relatively high-resolution cell

image, it required more than five average filters as shown in Figure 7.5a. Of note, there is noise (represented as white dots) two-times averaging. The image could not be obtained without a digital filter (one-time averaging), because it was impossible even to approach the pipette on the sample surface without a digital filter. If the control software picks the undesirable noise during approaching, the coarse Z stage is stopped before engaging the pipette to the sample surface sufficiently. So, the Z scanner remains fully extended, and loses the power of feedback.

In marked contrast, using the current source configuration, it is possible to scan and acquire reasonable cell images without digital filter as shown in Figure 7.5b. This finding demonstrates that the current source configuration may provide better performance than the voltage source configuration for imaging biological samples, and should be further explored.

7.5 Conclusions

In here, an alternative method was suggested to operate the SICM which applies current to the pipette sensor instead of voltage. This current source configuration of the electric circuit can have a lower output noise, and the bandwidth is not limited by the circuit component. Moreover, it was successfully demonstrated that DC mode and hopping-mode images with faster acquisition time in same image quality. This improvement would be useful to investigate the nanoscale dynamics of living cells. Furthermore, a positive aspect of the current source configuration is detecting the change of resistance linearly, and it can be helpful to analyze the behavior of the pipette dynamics more intuitively.

Even though the positive result was obtained from the suggested current source configuration, further discussion of the circuit model is presented in Section 8.2. Considering the origin of the access resistance R_{AC} changes, SNR of both configurations should be the same in contrast of this chapter result. Based on the corrected logic of SNR in Section 8.2, the ideas for improving SNR and understanding the dynamics of ion-current are discussed in Chapter 8.

References

- (1) Hansma, P. K.; Drake, B.; Marti, O.; Gould, S. A.; Prater, C. B. The scanning ion-conductance microscope. *Science* **1989**, *243*, 641–3.
- (2) Anariba, F.; Anh, J. H.; Jung, G. E.; Cho, N. J.; Cho, S. J. Biophysical Applications of Scanning Ion Conductance Microscopy (SICM). *Mod. Phys. Lett. B* **2012**, *26*, 1130003.
- (3) Happel, P.; Thatenhorst, D.; Dietzel, I. D. Scanning ion conductance microscopy for studying biological samples. *Sensors* **2012**, *12*, 14983–15008.
- (4) Schäffer, T. E.; Anczykowski, B.; Fuchs, H. In *Applied Scanning Probe Methods II*, 2006, pp 91–119.
- (5) Korchev, Y. E.; Bashford, C. L.; Milovanovic, M.; Vodyanoy, I.; Lab, M. J. Scanning ion conductance microscopy of living cells. *Biophys. J.* **1997**, *73*, 653–658.
- (6) Proksch, R.; Lal, R.; Hansma, P. K.; Morse, D.; Stucky, G. Imaging the internal and external pore structure of membranes in fluid: TappingMode scanning ion conductance microscopy. *Biophys. J.* **1996**, *71*, 2155–7.
- (7) Pastré, D.; Iwamoto, H.; Liu, J.; Szabo, G.; Shao, Z. Characterization of AC mode scanning ion-conductance microscopy. *Ultramicroscopy* **2001**, *90*, 13–19.
- (8) Shevchuk, A. I.; Gorelik, J.; Harding, S. E.; Lab, M. J.; Klennerman, D.; Korchev, Y. E. Simultaneous Measurement of Ca^{2+} and Cellular Dynamics: Combined Scanning Ion Conductance and Optical Microscopy to Study Contracting Cardiac Myocytes. *Biophys. J.* **2001**, *81*, 1759–1764.
- (9) Mann, S.; Hoffmann, G.; Hengstenberg, A.; Schuhmann, W.; Dietzel, I. Pulse-mode scanning ion conductance microscopy – a method to investigate cultured hippocampal cells. *J. Neurosci. Methods* **2002**, *116*, 113–117.
- (10) Happel, P.; Hoffmann, G.; Mann, S. A.; Dietzel, I. D. Monitoring cell movements and volume changes with pulse-mode scanning ion conductance microscopy. *J. Microsc.* **2003**, *212*, 144–151.
- (11) Happel, P.; Dietzel, I. D. Backstep scanning ion conductance microscopy as a tool for long term investigation of single living cells. *J. Nanobiotechnol.* **2009**, *7*, 7.

- (12) Takahashi, Y.; Murakami, Y.; Nagamine, K.; Shiku, H.; Aoyagi, S.; Yasukawa, T.; Kanzaki, M.; Matsue, T. Topographic imaging of convoluted surface of live cells by scanning ion conductance microscopy in a standing approach mode. *Phys. Chem. Chem. Phys.* **2010**, *12*, 10012–10017.
- (13) Ushiki, T.; Nakajima, M.; Choi, M.; Cho, S.-J.; Iwata, F. Scanning ion conductance microscopy for imaging biological samples in liquid: A comparative study with atomic force microscopy and scanning electron microscopy. *Micron* **2012**, *43*, 1390–1398.
- (14) Zhong, Q.; Inniss, D.; Kjoller, K.; Elings, V. Fractured polymer/silica fiber surface studied by tapping mode atomic force microscopy. *Surf. Sci. Lett.* **1993**, *290*, L688–L692.
- (15) Novak, P.; Li, C.; Shevchuk, A. I.; Stepanyan, R.; Caldwell, M.; Hughes, S.; Smart, T. G.; Gorelik, J.; Ostanin, V. P.; Moss, G. W. J.; Frolenkov, G. I.; Klenerman, D.; Korchev, Y. E. Nanoscale live-cell imaging using hopping probe ion conductance microscopy. *Nat. Methods* **2009**, *6*, 279–282.

Chapter 8

Conclusions and Future Outlook

From the demonstration of SPM strength over other microscopes, this dissertation offers the progress on SICM instrumentation. This chapter reconsiders the current-distance relation, which is the basic model of SICM. Unlike the discussion in Chapter 7, the signal-to-noise ratios (SNR) of both voltage source and current source configurations are concluded in the same considering the origin of the access resistance changes. By analyzing the SNR, the low-resistance pipette will improve the performance of SICM. The ultramicroelectrode (UME) can be the role of low-resistance pipette, and would be fabricated by electroplating. However, the fabrication of UME has not been optimized yet, the difficulties of UME fabrication are shortly discussed. In addition, since the current-distance model based on the Ohm's law does not fully explain the ion-transport phenomena in SICM, a working result of solving the Poisson-Nernst-Planck (PNP) equation is presented. The current implementation can solve the PNP problem with the boundary conditions of moderate surface charge density and electric potential. The in-depth understanding of the biological phenomena will be possible from the progress presented in this dissertation.

8.1 Conclusions

Scanning probe microscopy (SPM) has successfully demonstrated exploring the nano-scale phenomena over decades. Scanning ion-conductance microscopy (SICM) has an advantage over other SPM techniques. Although atomic force microscopy (AFM) has no limitation of the survey in vacuum, air, and liquid environments, SICM is specially developed to be operated in an electrolyte solution with *contact-free* nature. SICM monitors ion-current flows in the channel, which is geometrically formed between the pipette and the sample surface. When the pipette contacts the sample, ion-current cannot flow anymore. Hence, SICM is only capable of operating with an enough distance from the sample.

In this dissertation, the strength of AFM over scanning electron microscopy (SEM) was explored. Even though AFM does not seem to be suitable for the biological application, the detailed structures of mouse spermatozoa were observed even in contact-mode AFM. The end knob structure is destroyed by electron-beam of SEM, and the structure has not been reported before. However, the end knob structure was easily observed in AFM measurement with a simple sample preparation. However, for more accurate dimensional measurement, AFM can cause soft sample deformation even involving all of the state-of-art techniques in AFM. Hopping mode or ARS with amplitude modulation is a lot more useful for reducing the interaction between the AFM tip and the soft materials. But due to the nature of monitoring forces, the soft sample is compelled to be reshaped. The untouchable feature of SICM enables a reconstruction of more intact appearance of living cells. Besides the functionality of microscopy, AFM and SICM can profile a mechanical property of a specific area. While AFM natively probes the Young's modulus, SICM can measure the activity of cells. The distance between the cell surface and the SICM pipette is changed as much as the cell is active, and the change is reflected in the modulation of ion-current. From the time average of ion-current variation, the amount of steadiness of the surface can be estimated. This technique may become the complementary measure of the modulus.

Notwithstanding advantages of above mentioned, SICM still needs to be improved its sensor sensitivity and signal-to-noise ratio. Thus, the alternative configuration of the ampli-

flying scheme was presented to reduce the overall resistance of the pipette. Due to geometrically small structure and low conductance of electrolyte, the pipette has high impedance inevitably. The pipette resistance is a stray and has no dependency on the distance between the pipette and the surface, but this high resistance increases the noise and decreases the system bandwidth. This alternative scheme provides more stable and faster operation of SICM.

In summary, the findings presented in this dissertation show the superior capability of SICM to AFM and SEM for imaging biological samples in a liquid environment, and provide the advances both in instrumentation and theory. However, to be more accurate, some topics should be more clarified, and few of them are discussed below.

8.2 Current-Distance Relation: Critical Review of Chapter 7

8.2.1 Source of Current-Distance Relation in SICM

Although the work presented in Chapter 7 has an improvement of the signal-to-noise ratio, one logical question arises: What is the source of the current-distance relation? There has not been enough discussion of the current-distance relation so far. One indirect evidence of lack of discussion is that many researchers still focused on the inner opening diameter of the pipette end.¹⁻³ However, from the equation (2.6) and (2.7),⁴ the outer diameter of the pipette end also has the important role of sensing the distance between the pipette and the surface. The curvature of the equation (2.6) is determined by the ratio of outer radius to inner radius as shown in the equation (2.7). Obviously, this model is derived from the consideration of the beneath areas of the disk-shaped pipette glass wall, not only considering of the inner opening (Section 2.3). Therefore, this work should be reviewed with the more proper model of the pipette distance from the surface.

8.2.2 Access Resistance as a Voltage Source

Figure 8.1 shows a circuit model of the pipette as discussed in Section 2.3 and Section 7.2. The access resistance can be treated as the arbitrary voltage source in a circuit, which depends on the distance between the pipette and the surface. Hence, it is necessary to

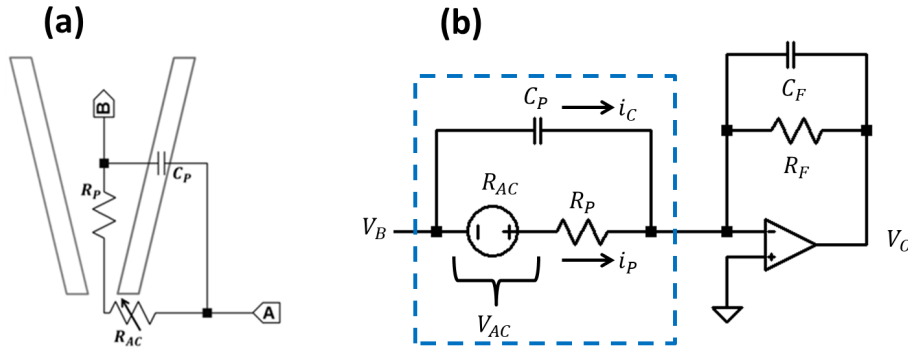


Figure 8.1 Circuit model of the pipette. (a) The circuit model of pipette consists of the pipette resistance R_P , capacitance C_P and the access resistance R_{AC} . (b) The pipette with the transimpedance amplifier. The dotted blue box represents the pipette circuit model

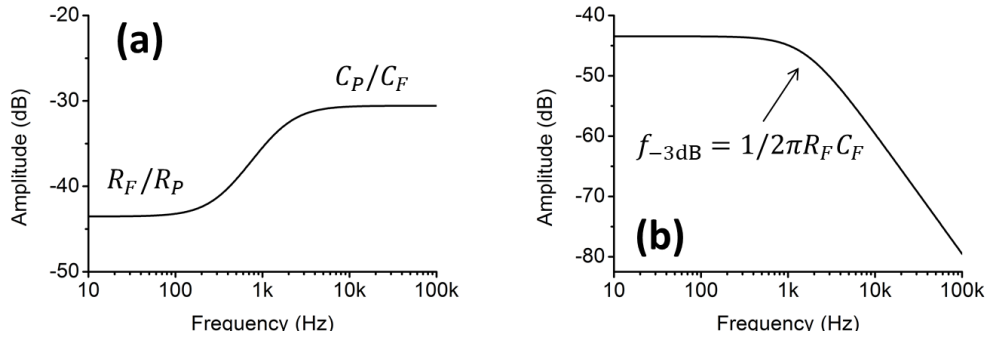


Figure 8.2 Frequency response of modulating (a) the voltage bias and (b) the access resistance.

discuss the bandwidth from the point of view of the voltage generated from R_{AC} instead of the externally applied voltage V_B .

In the constant voltage source (CV; V_{BA} is constant) configuration, there is no displacement current $i_C = C_P dV_{BA}/dt = 0$ at the pipette capacitance. Then, the ion-current i_{BA} and the R_{AC} dependent term s_V of the output voltage are

$$i_{BA} = i_P = \frac{V_{BA}}{R_P + R_{AC}} \quad (8.1)$$

$$s_V \simeq -\frac{R_F R_{AC}}{R_P^2} \frac{V_{BA}}{1 + j \cdot f/f_F} \quad (8.2)$$

where $j = \sqrt{-1}$ is the imaginary number, and $f_F = 1/2\pi C_F R_F$ is the bandwidth of the signal which is constrained by in-circuit elements. Figure 8.2 shows the result from SPICE

circuit simulation (LTspice, Linear Technology, US). Considering the pipette capacitance, the frequency response of the model used in this work (previously, the pipette capacitance was ignored) is plotted in Figure 8.2a. Fortunately, for the case of CV, the pipette capacitance has no role, and the frequency response of the access resistance is same as Figure 8.2b and as the previous discussion of Section 7.2.

In the constant current source (CC; i_{BA} is constant) configuration, where the pipette capacitance has a role and the displacement current exists, the voltage drops on the two electrodes V_{BA} and the output voltage s_I depending on R_{AC} are

$$V_{BA} = \frac{i_{BA}(R_{AC} + R_P)}{1 + j \cdot f/f_P} \quad (8.3)$$

$$s_I = \frac{i_{BA}R_{AC}}{1 + j \cdot f/f_P} \quad (8.4)$$

where $f_P = 1/2\pi C_P(R_{AC} + R_P)$ is the bandwidth of signal, which is determined by the pipette capacitance.

To compare two configurations, one can set the same in-circuit resistance, $R_F = R_B$, and the applied current when the pipette is not engaged to the surface, $V_{BA}/R_P = i_{BA}$. Comparing equations (8.2) and (8.4), the signal gain of CV is R_F/R_P whereas CC has unity gain. The total noise with arbitrary noise current i_n in CC and CV are expressed by

$$e_V = i_n R_F \frac{1 + j \cdot f/f_z}{1 + j \cdot f/f_P} \quad (8.5)$$

$$e_I = i_n R_P \frac{1 + j \cdot f/f_z}{1 + j \cdot f/f_P} \quad (8.6)$$

where $f_z = 1/2\pi(R_F \parallel (R_P + R_{AC}))(C_F + C_P)$ becomes the SNR bandwidth. The signal to noise ratio (SNR) in CV and CC are

$$\frac{s_V}{e_V} = \frac{i_{BA}}{i_n} \frac{R_{AC}}{R_P} \frac{1}{1 + j \cdot f/f_z} \quad (8.7)$$

$$\frac{s_I}{e_I} = \frac{i_{BA}}{i_n} \frac{R_{AC}}{R_P} \frac{1}{1 + j \cdot f/f_z}. \quad (8.8)$$

Thus, the SNRs of both configurations are the same.

This conclusion sounds more plausible than the one from Section 7.2. One paradox was missed: according to results from Section 7.2, one can obtain an infinite SNR if the current

setting resistance in the current source configuration is set to be zero, $R_B \rightarrow 0$. Then, the arising question is why the current source configuration showed better image quality than the voltage source configuration. One possible explanation is that in the current source configuration, the bandwidth is limited by the pipette bandwidth f_p as in the equation (8.4), which is in the order of a few hundred hertz, whereas the bandwidth is around 1 kHz in the voltage source configuration. The limited bandwidth means more low-pass filtering, and changed configuration might apply an analog filter instead of a digital filter. Consequently, it is quite worthy to try setting the feedback resistance to 5 G Ω or 10 G Ω in order to acquire improved signal-to-noise ratio with the bandwidth ranged from 160 Hz to 320 Hz, which is the bandwidth of the current source configuration.

8.2.3 Discussion on Improving the Signal-to-Noise Ratio

From the equations (8.7) and (8.8), two goals to improve the signal-to-noise ratio (SNR) can be induced:

1. f_z should be high enough, and
2. R_{AC}/R_P also should be high.

In consequence, the pipette resistance R_P and the pipette capacitance C_P should be low, and the sensitivity of the access resistance needs to be high. From the equations (2.5) and (2.6), the subsequent results are

1. The ratio of outer to inner radii r_i/r_o should be high,
2. The half cone angle θ should be high,
3. The conductivity of electrolyte κ should be high.

Therefore, it is worth to fabricate the pipette from multiple capillaries with different ratios of outer to inner radii, and to pull capillaries with different pulling parameters to adjust the

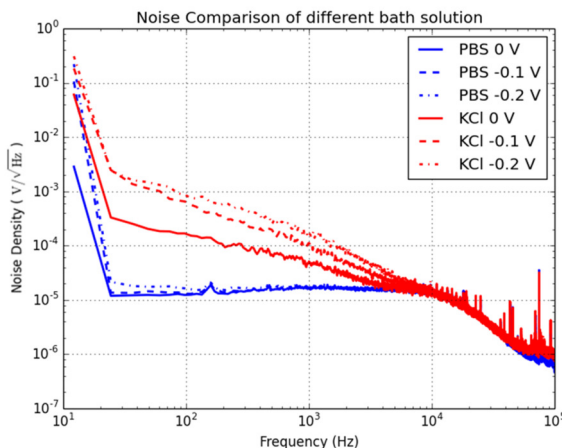


Figure 8.3 Noise spectrums from PBS (blue) and 3M KCl (red) bath solutions.

pipette tip shape. The prospect of high-conductive pipettes is discussed in the following section.

8.3 Ultramicroelectrode

8.3.1 Electrolyte Filled Pipette

Schäffer, Anczykowski, and Fuchs suggested the highly conductive electrolyte filled pipette to reduce the pipette resistance in their review paper.⁵ They expected “The diffusion of this solution into the bath solution would be small due to the small tip diameter.” But in the preliminary experiment, the diffusion from an imbalance of concentrations between the inside of and outside of the pipette was not ignorable. Figure 8.3 shows the noise spectrum density from two bath solutions with a PBS filled pipette. The blue line was obtained from the bath solution of PBS which was same as the solution inside of the pipette, and the red line was from the bath solution of 3 M KCl, which was different from the solution of the pipette. The $1/f$ slope of the PBS(pipette)–3 M KCl(bath) in the range of 20 Hz to 10 kHz is the evidence of the DC drift of the measured current when even 0 V bias was applied. Therefore, the imbalance of solutions between the inside and the outside of the pipette builds a liquid junction potential and tends to make the system unstable.

The high-conductive pipettes will boost studies on not only SICM but also electrophys-

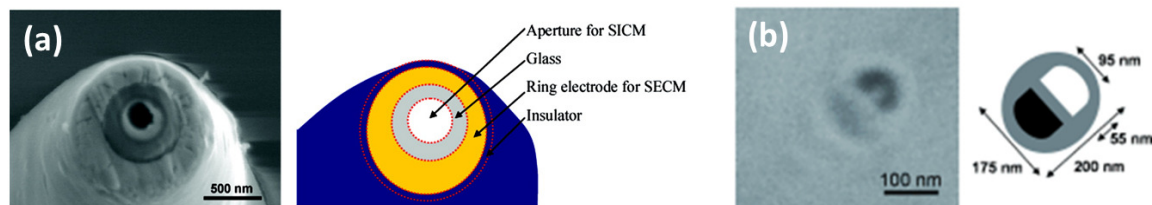


Figure 8.4 SEM images and schematics of SECM/SICM probes. (a) A SECM/SICM probe by coating Ti/Au or Ti/Pt on the pulled pipette, (b) by filling carbon on one channel of a double barrel pipette. Adapted from Takahashi et al. 2010⁶ and Takahashi et al. 2011⁷

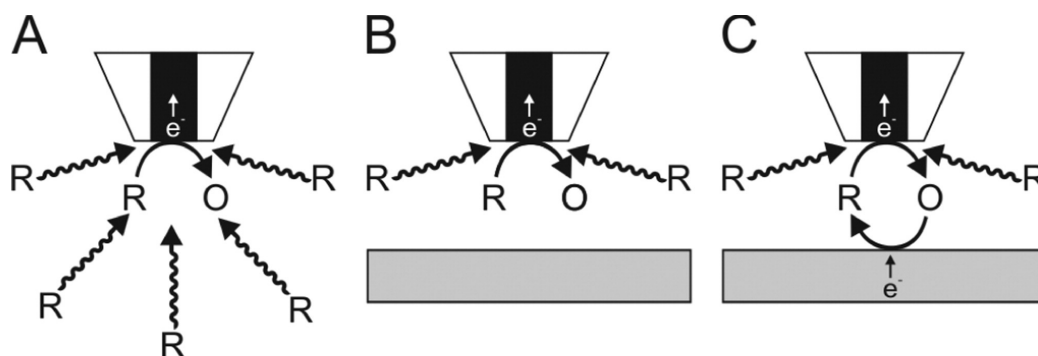


Figure 8.5 Some represented modes in SECM. (A) Steady-state behavior (diffusion-limited) in bulk solution. (B) Feedback mode over an inert substrate (negative feedback). (C) Feedback mode over a conducting substrate (positive feedback). Adapted from Polcari, Dauphin-Ducharme, and Mauzeroll 2016.¹⁰

iology. This topic is highly important for extending the knowledge of nature. All SICM uses electrolyte filled pipettes so far, and using different solution from the bath electrolyte seems to be undesirable.

8.3.2 Ultramicroelectrode (UME)

The metal filled pipette is known as the ultramicroelectrode (UME). Fabricating UMEs is one of important topic in electrochemistry, especially scanning electrochemical microscopy (SECM).^{8,9} Takahashi et al. fabricated a SECM/SICM probe by coating Ti/Au or Ti/Pt on the pulled glass capillary.⁶ After one year, Takahashi et al. introduced another type of SECM/SICM probe by filling carbon in one channel of a pulled double barrel pipette.⁷ Figure 8.4 shows the SEM images of those probes.

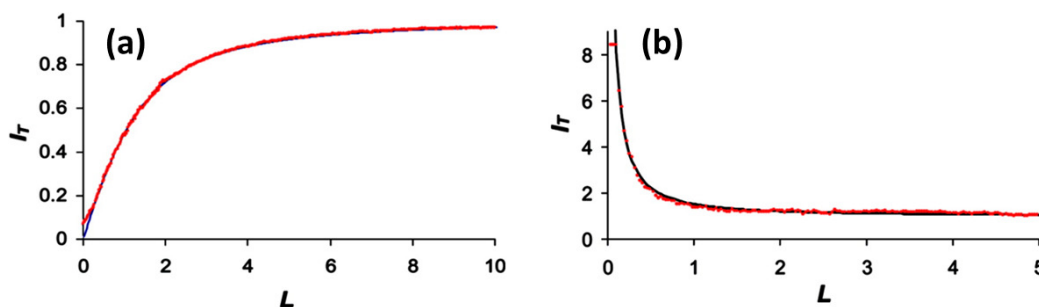


Figure 8.6 Current-distance curves for (a) negative feedback mode and (b) positive feedback mode in SECM. Adapted from Velmurugan, Sun, and Mirkin 2008.¹¹

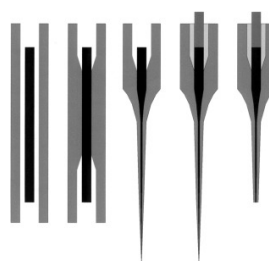


Figure 8.7 UME fabrication process by pulling the capillary and the electrode together. Adapted from Katemann and Schuhmann 2002.¹²

In SECM, there are several modes to be involved in analyzing a chemical reaction; negative feedback mode, positive feedback mode, tip-generation/substrate-collection mode, substrate-generation/tip-collection mode, redox competition mode, and so on.¹⁰ Figure 8.5 shows diffusion limited mode, negative feedback mode, positive feedback mode for instance.

Figure 8.6 shows current-distance curves from negative feedback mode and positive feedback mode. The red dots indicates the experimental data, and the solid black lines refer to the fitted curve from the model. The current-distance curve of the negative feedback mode is similar to the curve of SICM. The UME, which is used in SECM, can be a distance sensor, although the electrode is protruded till the end of the pipette apex, whereas the electrode in SICM is recessed far from the pipette apex.

One of widely used methods to fabricate UMEs is developed by Mirkin's group^{11,13,14}

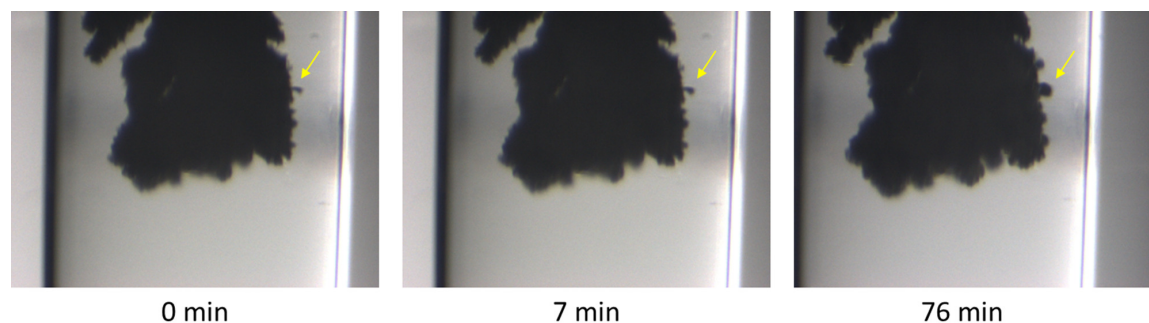


Figure 8.8 Electroplating of commercial silver-cyanide solution in a capillary.

and Schuhmann's group.^{9,12} This method pulls the pipette and the metal wire, which was inserted in the pipette, together. Figure 8.7 shows the process of fabrication of UMEs. They used two-step pulling; the first step was to grab the electrode, then hard pulling was applied to make the capillary and the electrode to shape.

However, from the different melting points between glass and metal, it was hard to find the optimum pulling protocol. The metal was broken discontinuously locating inside of pipettes in the preliminary experiments. Therefore, the idea to fabricate UMEs can be adopted from the nanowire fabrication by anodic aluminum template assisted electrodeposition.¹⁵

8.3.3 UME Fabrication by Electroplating

It is a popular method to use an anodic aluminum oxide (AAO) as a template for fabricating nanowires.^{15–18} The dimension of the nanopipette tip end has the same order of magnitude dimension of nanowires. However, from the conically shaped asymmetric geometry of nanopipettes, there were some challenges to grow silver in a pipette.

Figure 8.8 shows a result from a commercial silver-cyanide solution (Silver 1025, Technic, USA) in a 0.6 mm inner diameter capillary. Even though the experiment was conducted in a capillary with relatively wide opening instead of the nanopipette, the plating throughput was quite poor. Minimal growth was found as indicated by the white arrow for 76 minutes. This slow growth rate may stem from the negative valency of the silver cyanide ion. The

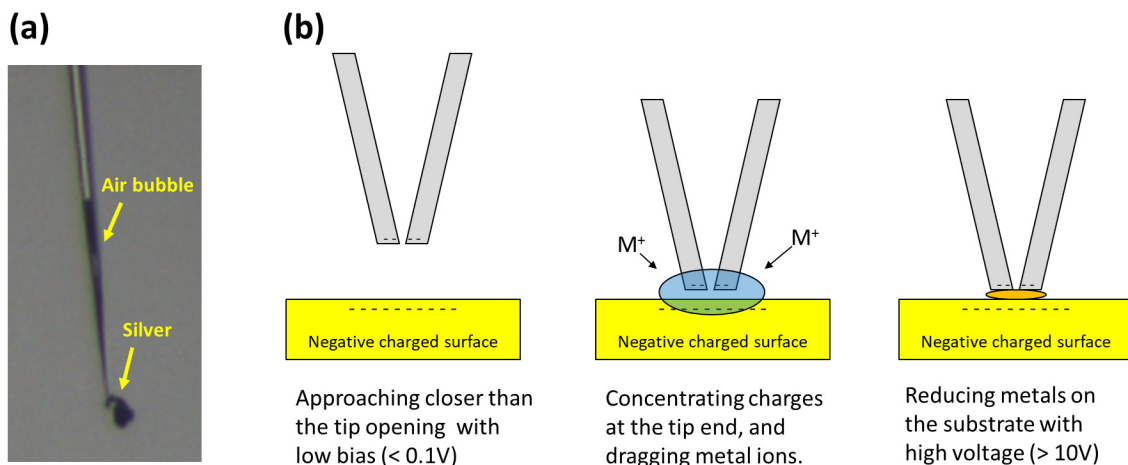
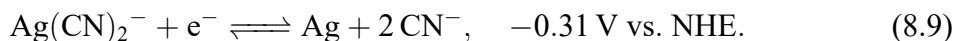


Figure 8.9 Reduction at the tip end with 10 mM AgNO_3 solution. (a) Silver can be reduced at the tip end without any metal electrode. (b) The idea of metal patterning using an electrolyte filled pipette.

cathodic reaction is given by¹⁹



Hence, the replenishment of silver cyanide ion strongly depends only on diffusion but not migration.

Figure 8.9a shows an electroplating result with 10 mM AgNO_3 solution. In this case, the cathode potential was applied -5 V relative to the bath electrode. Surprisingly, the reduction of silver ion was occurred at the end of the pipette tip, instead of the silver electrode located inside of the pipette. This result is expected that the singular geometry of the tip end is lowering down the electrical potential unusually from the negatively charged glass surface. Although this phenomenon is a barrier of the fabrication of UMEs, it could be used for nanopatterning on the substrate as sketched in Figure 8.9b. The nanopipette approaches the surface as SICM usually do, and positive metal ions migrate to the highly negatively charged point. Then, high voltage can be applied to reduce metal ions to metal solid on the target surface.

The third challenge is that depletion of ions in the pipette can be easily occurred. Figure 8.10 shows the dendric growth of silver due to depletion of ions in the pipette during con-

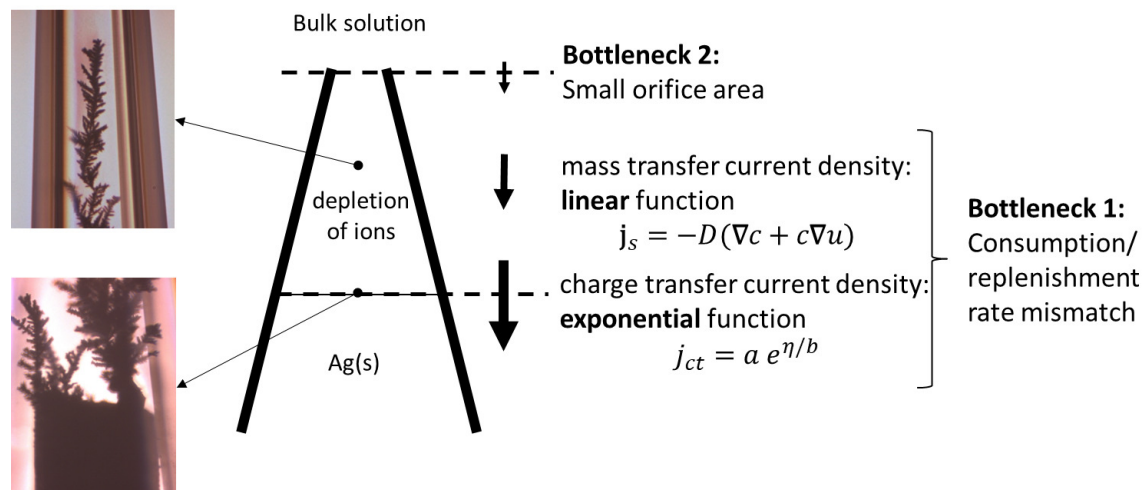
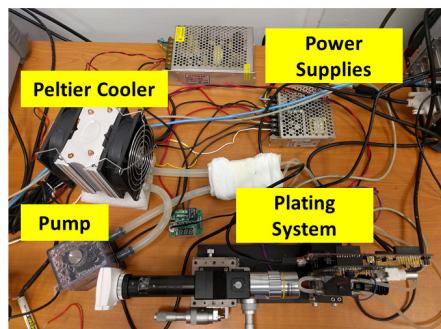


Figure 8.10 Dendritic growth of silver due to depletion of ions for DC plating in the pipette.

(a)



(b)

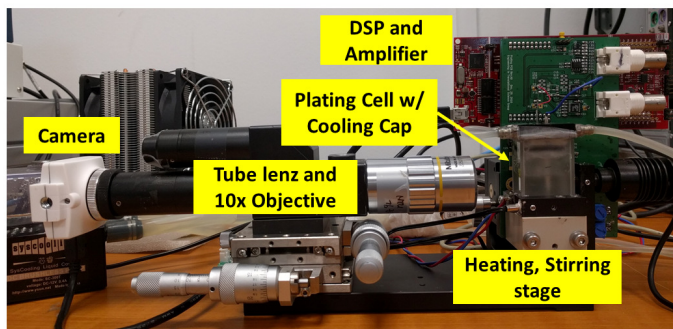


Figure 8.11 Custom made plating station. (a) The whole system for electroplating including water cooling parts, and (b) the plating station.

tinuous DC plating. The electrolyte contained $2 \text{ g L}^{-1} \text{ AgNO}_3$, 20 g L^{-1} of boric acid, and is buffered to pH 2 with H_2SO_4 ²⁰ to change the glass surface potential. The boric acid is considered to suppress hydrogen evolution.²¹ Ions are consumed exponentially on the electrode surface according to Butler-Volmer equation or Tafel equation.²² However, the ion migration obeys linear Nernst-Planck equation. Moreover, the entrance of ions is relatively too small comparing to the area of the target electrode surface.

The pulse plating is widely used for modern plating industry to deposit metals compactly.²³ Therefore, a custom plating system was developed. The plating system is digital

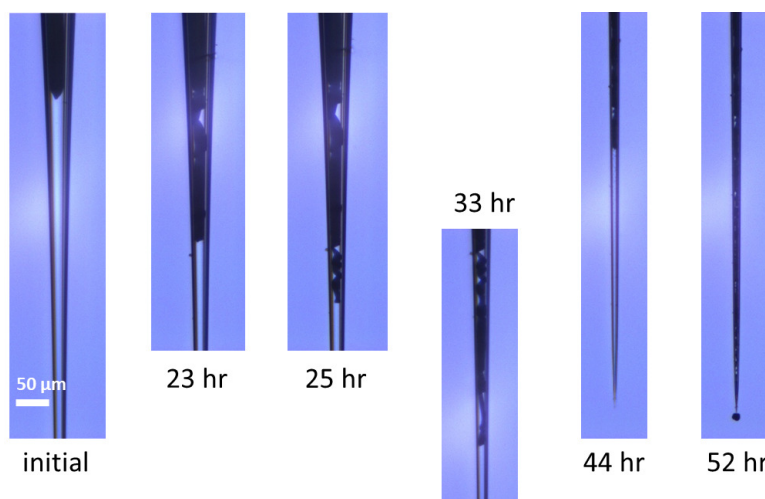


Figure 8.12 Snapshots of electroplating of silver inside of the pipette.

signal processor (DSP) controlled to generate pulses, as shown in Figure 8.11. This plating station is comprised of an optical system for monitoring electrodeposition with XY and Z micrometer stages, the control circuit board which is controlled by a floating point digital signal processor (TMS320F28377S, Texas Instruments, US), a custom-made heating and stirring stage, and a water cooling system with a Peltier element and a water pump for preventing evaporation of solution from the heating.

Figure 8.12 shows snapshots of silver plating in the pipette. Finally, after 52 hours, silver was growing to the end of the pipette. This overgrown fraction can be eliminated by dipping in nitric acid or applying a reverse bias for anodic reaction. The electroplating solution contains $5 \text{ g L}^{-1} \text{ AgNO}_3$ and 20 g L^{-1} boric acid, and is buffered to pH 2 by H_2SO_4 . The temperature of the chemical cell is maintained at 80°C . The period of current pulse was 100 ms, and the on-time is decided by the proportional-integral feedback algorithm. If the inside solution was not stabilized, the plating cell builds electrochemical potential. So, the feedback error calculated the difference between a given setpoint, e.g. 50 mV and the output voltage of the amplifier at a certain time in off-period, e.g. 50 ms, when the current set to zero. A thin gold wire with the diameter of $25 \mu\text{m}$ was an initial electrode for electroplating. The overall elapsed time was about 2 days. Although Figure 8.12 is one of the positive results, it is necessary to improve reproducibility with the current protocol.

8.4 Beyond the Ohmic Model

The overall discussion of this dissertation was based on the linear Ohm's law, but the nonlinear effect like the rectification in the nanopipette was reported.^{24–26} Therefore, it is necessary to extend the model to ion-transport phenomenon based on the Poisson-Nernst-Planck (PNP) equation to understand the pipette dynamics. This section briefly examines the feasibility of the finite element method solver implemented by FEniCS project.²⁷ This solver will give insights for optimizing the electroplating system for fabrication of UMEs, and for better understanding the kinetics of ion-current signals with the consideration of surface charges.

Gummel firstly solved PNP equation with the iteration method in 1964.²⁸ With the assumption of ideal gases or Boltzmann distribution, the concentration c_i for i -th ion is

$$c_i = \exp\left(\frac{\mu_i - z_i F \phi}{RT}\right) \quad (8.10)$$

where ϕ is electrostatic potential, μ_i and z_i are the chemical potential and the valency of i -th ion, respectively. F , R and T are the Faraday number, the gas constant, and the absolute temperature, respectively.

The first step of the iteration is to obtain electrostatic potential ϕ with given chemical potentials by solving the Poisson-Boltzmann equation,

$$-\epsilon \nabla^2 \phi = F \sum_i z_i \exp\left(\frac{\mu_i - z_i F \phi}{RT}\right). \quad (8.11)$$

Then, the second step is to calculate chemical potentials μ_i or concentrations c_i with pre-calculated electrostatic potential ϕ by solving the Nernst-Planck equation,

$$-\mathbf{j}_i = D_i \left(\nabla c_i + \frac{z_i F}{RT} \nabla \phi \right) \quad (8.12)$$

with the continuity equation,

$$\frac{\partial c_i}{\partial t} + \nabla \cdot \mathbf{j}_i = 0. \quad (8.13)$$

The FEM solver repeats the first and the second steps, iteratively, until there is no significant difference between the previous solution and the lastly calculated solution.

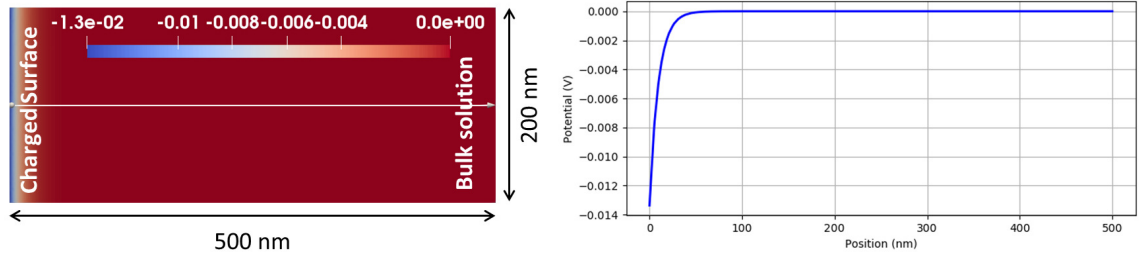


Figure 8.13 Numerical result of Gouy-Chapman model.

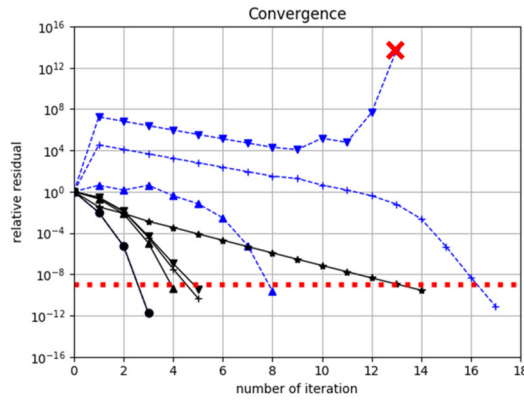


Figure 8.14 Convergence of Poisson-Boltzmann equation. circle: 0.001, triangle up: 0.011 cross: 0.032, triangle down: 0.045, star: 1 C/m^2 , blue dash line: the initial guess is set to zero, black solid line: the initial guess is from the previous solution. The red dotted line indicates the termination condition. The red cross mark indicates terminated without convergence.

8.5 Solving Poisson-Boltzmann Equation

First, the Poisson-Boltzmann (PB) equation was validated with the problem of a rectangular box ($500 \text{ nm} \times 200 \text{ nm}$). The basic method to solve PB equation is described in Section 3.3. This problem is known as Gouy-Chapman model.²⁹ The geometry is the same as that White and Bund was used.³⁰ The left boundary is the charged surface with the surface charge in the range of -1 mC/m^2 to -1 C/m^2 . The right boundary is set to the pseudo-infinite boundary with the electrostatic potential of zero and 1 mM concentration. Figure 8.13 shows a represented plot with the surface charge of -1 mC/m^2 . The electrostatic potential of the left boundary is obtained as -13.63 mV , which is the same as the numerical value of White and Bund.³⁰

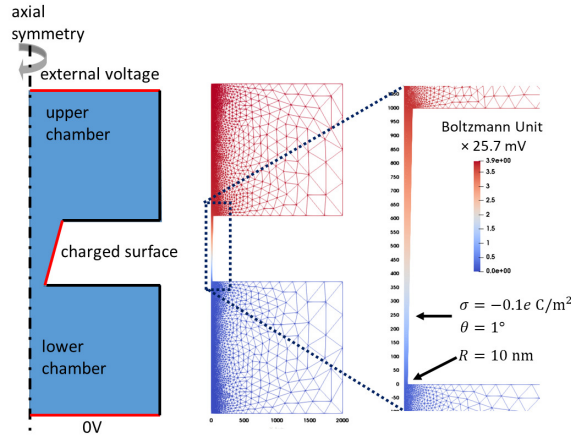


Figure 8.15 The pipette geometry and the mesh of PNP problem.

Figure 8.14 shows the convergence plots of the FEM solver. The blue dashed lines are calculated with that the initial value of the electrostatic potential is set to zero. From -45 mC/m^2 , the solver was divergent, and could not find a solution. In contrast, if the initial guess is taken from the previous result, which is calculated with less surface charge density, then the solver can solve up to the surface charge density of -1 mC/m^2 with fewer iteration steps. The convergence of Newton method highly depends on the initial guesses.³¹ Lately, inexact Newton method with ensuring global convergence was developed,^{32–37} thus it is worth to implement those methods to have robust FEM solver.

8.5.1 Poisson-Nernst-Planck Equation

To validate PNP solver, one simple geometry is tested. Figure 8.15 shows 2D axial symmetric geometry and the mesh of the nanopipette, similar to one of Sa et al.³⁸ This study assumes two univalent ions exist. The bulk concentration of $c_0 = 1 \text{ mM}$, and the surface charge of the slanted line of $\sigma = -0.1e \text{ C/m}^2$ (16 mC/m^2) were used. The bottom and top boundary are set to pseudo-infinite condition. The electrostatic potential of the bottom boundary is 0 V , and the electrostatic potential of the top boundary is set to -0.1 V , 0 V and 0.1 V . Figure 8.15 is the result with the 0.1 V top boundary condition, and the solution is colored according to the color map.

Figure 8.16 shows the simulation results. The electrostatic potential changes gradually,

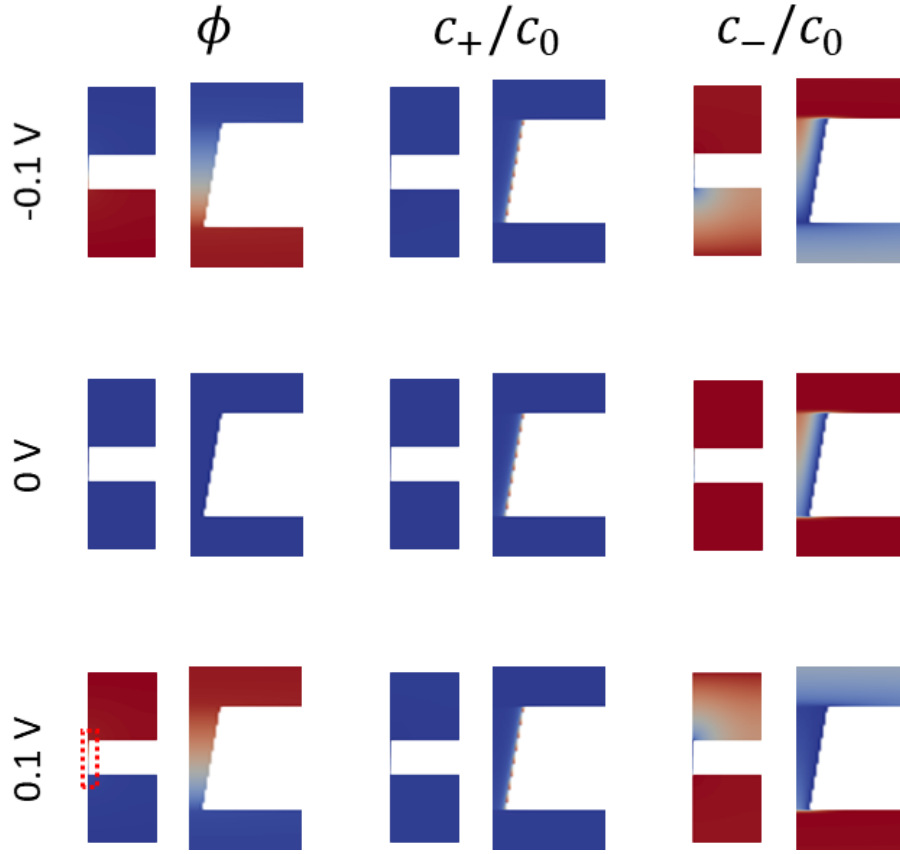


Figure 8.16 FEM Simulation result of the pipette problem. The values are color mapped from highest value marked red to lowest value marked blue. The overall results are displayed on the left side for each case, and zoomed results to highlight the inside of pipette are on the right side with 1:10 aspect ratio.

and the concentration of the counterion c_+/c_0 from the surface charge seems not to be changed in the overall domain. The concentration gradients of the coion c_-/c_0 are reversed when the direction of electrostatic potential is changed.

The line profile along the symmetric axis are plotted in Figure 8.17. When 0.1 V is applied in the pipette, the concentration of coion c_-/c_0 is more depleted inside of pipette than when -0.1 V is applied. This means that the magnitude of ion-current is more hindered when ion-current flows out of the pipette, which is well corresponding to experimental results and other analyses.^{24–26,39,40} Interestingly, electrostatic potential at the 0 V boundary condition, there is no significant values in the electrostatic potential profile in contrast of

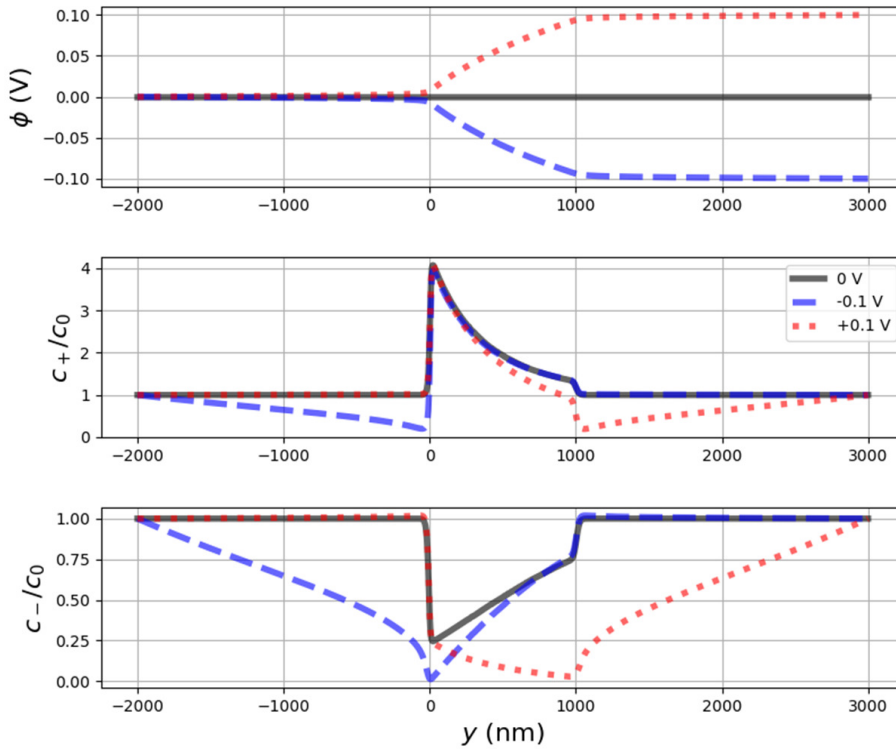


Figure 8.17 Line profiles of the pipette simulation.

the result from Cervera et al.^{39,40} But the result seems to be more physically appreciated because of considering equilibrium. If there is a non-even electrostatic potential, free charged particles should adjust their location to cancel the electrostatic potential out.

8.6 Future Work

This chapter shortly discussed two intermediate results. First, the ultramicroelectrode (UME) fabrication to improve the signal-to-noise ratio (SNR) based on Nitz's model, which assumed Ohm's law.⁴ Second, the finite element method (FEM) solution of the nonlinear Poisson-Nernst-Planck (PNP) equation to extend the Nitz's model for elucidating the surface charge effect in the electrolyte solution. The idea of UME fabrication is adopted from the fabrication of nanowires in the anodized aluminum oxide (AAO) template because of the similar dimension of the pipette opening with the one of the nanowire. However, there are several challenges from the singular geometry of the nanopipette unlike from the situa-

tion of the fabrication of nanowires. Even though some positive results were obtained, the reproducibility of UMEs should be improved.

The ions in the electrolyte solution can be described by the PNP equation with the assumption of infinitely small charged particles in a continuous medium. To solve PNP equation, the Poisson-Boltzmann equation should be solved. However, from the nonlinearity of the Poisson-Boltzmann equation, the solution is merely calculated. The result demonstrated in this chapter was from loosened boundary conditions of the surface charge density and the applied external voltage. Hence, it is necessary to implement a robust method to cover more realistic surface charge density and electrostatic potential boundary conditions. Moreover, the interpretation of data to understand the rectification effect should be further discussed.

In this dissertation, advantages of SICM over SEM and AFM were discussed. SICM can take high-resolution images with *contact-free* so that soft biological samples are intact during measurement, and the dimensional analysis of soft materials is possible. However, a whole cell image with hopping mode SICM takes a long time because of poor signal-to-noise ratio (SNR) from the high-resistance of the nanopipette. The improving SNR can be attained by using current source configuration instead of the conventional voltage source configuration. Also, if the low resistance pipette is applied to SICM, the performance of SICM will increase. Therefore, the fabrication method of the low resistance pipette or the ultramicroelectrode is under optimization. The current-distance relation does not simply obey Ohm's law, so the solver of the Poisson-Nernst-Planck equation is being implemented more robustly to understand ion-transport phenomena in the electrolyte solution. The progress presented in this dissertation will unveil biological phenomena in the future.

References

- (1) Rheinlaender, J.; Schäffer, T. E. Image formation, resolution, and height measurement in scanning ion conductance microscopy. *J. Appl. Phys.* **2009**, *105*, 094905.
- (2) Rheinlaender, J.; Schaffer, T. E. Lateral Resolution and Image Formation in Scanning Ion Conductance Microscopy. *Anal. Chem.* **2015**, *87*, 7117–24.

- (3) Caldwell, M.; Del Linz, S. J. L.; Smart, T. G.; Moss, G. W. J. Method for estimating the tip geometry of scanning ion conductance microscope pipets. *Anal. Chem.* **2012**, *84*, 8980–8984.
- (4) Nitz, H.; Kamp, J.; Fuchs, H. A combined scanning ion-conductance and shear-force microscope. *Probe Microscopy* **1998**, *1*, 187–200.
- (5) Schäffer, T. E.; Anczykowski, B.; Fuchs, H. In *Applied Scanning Probe Methods II*, 2006, pp 91–119.
- (6) Takahashi, Y.; Shevchuk, A. I.; Novak, P.; Murakami, Y.; Shiku, H.; Korchev, Y. E.; Matsue, T. Simultaneous Noncontact Topography and Electrochemical Imaging by SECM/SICM Featuring Ion Current Feedback Regulation. *J. Am. Chem. Soc.* **2010**, *132*, 10118–10126.
- (7) Takahashi, Y.; Shevchuk, A. I.; Novak, P.; Zhang, Y.; Ebejer, N.; Macpherson, J. V.; Unwin, P. R.; Pollard, A. J.; Roy, D.; Clifford, C. A. Multifunctional nanoprobe for nanoscale chemical imaging and localized chemical delivery at surfaces and interfaces. *Angew. Chem.* **2011**, *50*, 9638–9642.
- (8) Kranz, C. Recent advancements in nanoelectrodes and nanopipettes used in combined scanning electrochemical microscopy techniques. *Analyst* **2014**, *139*, 336–352.
- (9) Clausmeyer, J.; Schuhmann, W. Nanoelectrodes: Applications in electrocatalysis, single-cell analysis and high-resolution electrochemical imaging. *TrAC, Trends Anal. Chem.* **2016**, *79*, 46–59.
- (10) Polcari, D.; Dauphin-Ducharme, P.; Mauzeroll, J. Scanning Electrochemical Microscopy: A Comprehensive Review of Experimental Parameters from 1989 to 2015. *Chem. Rev.* **2016**, *116*, 13234–13278.
- (11) Velmurugan, J.; Sun, P.; Mirkin, M. V. Scanning electrochemical microscopy with gold nanotips: the effect of electrode material on electron transfer rates. *J. Phys. Chem. C* **2008**, *113*, 459–464.
- (12) Katemann, B. B.; Schuhmann, W. Fabrication and Characterization of Needle-Type. *Electroanalysis* **2002**, *14*, 22–28.
- (13) Shao, Y.; Mirkin, M. V.; Fish, G.; Kokotov, S.; Palanker, D.; Lewis, A. Nanometer-sized electrochemical sensors. *Anal. Chem.* **1997**, *69*, 1627–1634.

- (14) Noël, J.-M.; Velmurugan, J.; Gökmeşe, E.; Mirkin, M. V. Fabrication, characterization, and chemical etching of Ag nanoelectrodes. *J. Solid State Electrochem.* **2013**, *17*, 385–389.
- (15) Stępniewski, W. J.; Salerno, M. Fabrication of nanowires and nanotubes by anodic alumina template-assisted electrodeposition. 2014.
- (16) Pang, Y.; Meng, G.; Shan, W.; Zhang, L.; Gao, X.; Zhao, A.; Mao, Y. Arrays of ordered Ag nanowires with different diameters in different areas embedded in one piece of anodic alumina membrane. *Appl. Phys. A: Mater. Sci. Process.* **2003**, *77*, 717–720.
- (17) Lee, W.; Scholz, R.; Nielsch, K.; Gösele, U. A Template-Based Electrochemical Method for the Synthesis of Multisegmented Metallic Nanotubes. *Angew. Chem.* **2005**, *117*, 6204–6208.
- (18) Zhang, J.; Kielbasa, J. E.; Carroll, D. L. Nanostructure of the nanopores in anodic aluminum oxide films used as template to fabricate Ag nanowires. *J. Mater. Res.* **2009**, *24*, 1735–1740.
- (19) Sánchez, H.; Chainet, E.; Nguyen, B.; Ozil, P.; Meas, Y. Electrochemical deposition of silver from a low cyanide concentration bath. *J. Electrochem. Soc.* **1996**, *143*, 2799–2804.
- (20) Zhang, J.; Kielbasa, J. E.; Carroll, D. L. Controllable fabrication of porous alumina templates for nanostructures synthesis. *Mater. Chem. Phys.* **2010**, *122*, 295–300.
- (21) Tsuru, Y.; Nomura, M.; Foulkes, F. Effects of boric acid on hydrogen evolution and internal stress in films deposited from a nickel sulfamate bath. *J. Appl. Electrochem.* **2002**, *32*, 629–634.
- (22) Bard, A. J.; Faulkner, L. R., *Electrochemical methods: fundamentals and applications*. Wiley New York: 1980; Vol. 2.
- (23) Chandrasekar, M.; Pushpavanam, M. Pulse and pulse reverse plating — Conceptual, advantages and applications. *Electrochim. Acta* **2008**, *53*, 3313–3322.
- (24) Wei, C.; Bard, A. J.; Feldberg, S. W. Current rectification at quartz nanopipet electrodes. *Anal. Chem.* **1997**, *69*, 4627–4633.
- (25) Gamble, T.; Decker, K.; Plett, T. S.; Pevarnik, M.; Pietschmann, J.-F.; Vlassiouk, I.; Aksimentiev, A.; Siwy, Z. S. Rectification of ion current in nanopores depends on

- the type of monovalent cations: experiments and modeling. *J. Phys. Chem. C* **2014**, *118*, 9809–9819.
- (26) Siwy, Z.; Heins, E.; Harrell, C. C.; Kohli, P.; Martin, C. R. Conical-nanotube ion-current rectifiers: the role of surface charge. *J. Am. Chem. Soc.* **2004**, *126*, 10850–10851.
- (27) Logg, A.; Mardal, K.-A.; Wells, G., Automated solution of differential equations by the finite element method: The FEniCS book. Springer Science & Business Media: 2012; Vol. 84.
- (28) Gummel, H. K. A self-consistent iterative scheme for one-dimensional steady state transistor calculations. *IEEE Trans. Electron Devices* **1964**, *11*, 455–465.
- (29) Kirby, B. J., Micro-and nanoscale fluid mechanics: transport in microfluidic devices. Cambridge University Press: 2010.
- (30) White, H. S.; Bund, A. Ion current rectification at nanopores in glass membranes. *Langmuir* **2008**, *24*, 2212–2218.
- (31) Wright, S. J.; Nocedal, J. Numerical optimization. *Springer Science* **1999**, *35*, 7.
- (32) Eisenstat, S. C.; Walker, H. F. Globally convergent inexact Newton methods. *SIAM J. Optim.* **1994**, *4*, 393–422.
- (33) Eisenstat, S. C.; Walker, H. F. Choosing the forcing terms in an inexact Newton method. *SIAM J. Sci. Comput.* **1996**, *17*, 16–32.
- (34) Shadid, J. N.; Tuminaro, R. S.; Walker, H. F. An inexact Newton method for fully coupled solution of the Navier–Stokes equations with heat and mass transport. *J. Comput. Phys.* **1997**, *137*, 155–185.
- (35) Cai, X.-C.; Keyes, D. E. Nonlinearly preconditioned inexact Newton algorithms. *SIAM J. Sci. Comput.* **2002**, *24*, 183–200.
- (36) Hwang, F.-N.; Cai, X.-C. A parallel nonlinear additive Schwarz preconditioned inexact Newton algorithm for incompressible Navier–Stokes equations. *J. Comput. Phys.* **2005**, *204*, 666–691.
- (37) Liu, L.; Keyes, D. E. Field-split preconditioned inexact Newton algorithms. *SIAM J. Sci. Comput.* **2015**, *37*, A1388–A1409.
- (38) Sa, N.; Lan, W.-J.; Shi, W.; Baker, L. A. Rectification of Ion Current in Nanopipettes by External Substrates. *ACS Nano* **2013**, *7*, 11272–11282.

- (39) Cervera, J.; Schiedt, B.; Ramírez, P. A Poisson/Nernst-Planck model for ionic transport through synthetic conical nanopores. *Europhys. Lett.* **2005**, *71*, 35.
- (40) Cervera, J.; Schiedt, B.; Neumann, R.; Mafé, S.; Ramírez, P. Ionic conduction, rectification, and selectivity in single conical nanopores. *J. Chem. Phys.* **2006**, *124*, 104706.

List of Publications

Citations to Previously Published Work

Chapter 5 appeared as

Kim, J.; Choi, M.; Jung, G.-E.; Ferhan, A. R.; Cho, N.-J.; Cho, S.-J. Dimensional comparison between amplitudemodulation atomic force microscopy and scanning ion conductance microscopy of biological samples. *Jpn. J. of Appl. Phys.* **2016**, 55, 08NB18.

Chapter 6 appeared as

Kim, S.-O.†; **Kim, J.**†; Okajima, T.; Cho, N.-J. Mechanical properties of paraformaldehyde-treated individual cells investigated by atomic force microscopy and scanning ion conductance microscopy. *Nano Convergence* **2017**, 4, 5. († denotes equal contribution)

Chapter 7 appeared as

Kim, J.; Kim, S.-O.; Cho, N.-J. Alternative configuration scheme for signal amplification with scanning ion conductance microscopy. *Rev. Sci. Instrum.* **2015**, 86, 023706.

Additional Doctoral Work Published Outside of Thesis

Lee, D.†; **Kim, J.**†; Cho, N.-J.; Kang, T.; Kauh, S.; Lee, J. Pulled microcapillary tube resonators with electrical readout for mass sensing applications. *Sci. Rep.*, **2016**, 6, 33799.

(† denotes equal contribution)